Solid-State Flow Control for Ion Electrospray Propulsion

By

Jonathan V. MacArthur

B.S., Iowa State University 2017

S.M., Massachusetts Institute of Technology 2020

Submitted to the Department of Aeronautics and Astronautics
in partial fulfillment of the requirements for the degree of

DOCTOR OF PHILOSOPHY IN AERONAUTICS AND ASTRONAUTICS

at the

MASSACHUSETTS INSTITUTE OF TECHNOLOGY

June 2023

©Jonathan V. MacArthur 2023. All rights reserved.
The author hereby grants to MIT a nonexclusive, worldwide, irrevocable, royalty-free license to exercise any and all rights under copyright, including to reproduce, preserve, distribute and publicly display copies of the thesis, or release the thesis under an open-access license.

Authored by: Jonathan V. MacArthur
Department of Aeronautics and Astronautics
March 17, 2023

Certified by: Paulo C. Lozano
M. Alemán-Velasco Professor of Aeronautics and Astronautics, Thesis supervisor

Rohit Karnik
Professor of Mechanical Engineering, Committee Member

Kripa Varanasi
Professor of Mechanical Engineering, Committee Member

Accepted by: Jonathan P. How
R. C. Maclaurin Professor of Aeronautics and Astronautics
Chair, Graduate Program Committee

Solid-State Flow Control for Ion Electrospray Propulsion

by

Jonathan V. MacArthur

Submitted to the Department of Aeronautics and Astronautics
on May 2023, in partial fulfillment of the
requirements for the degree of
Doctor of Philosophy in Aeronautics and Astronautics

Abstract

Electrospray propulsion offers high-efficiency, low-mass propulsive capabilities, based on ion extraction from ionic liquid propellants, to small spacecraft that exceed the capabilities of conventional chemical propulsion. Two shortcomings of such propulsion systems is their lack of lightweight propellant management due to the restrictive sizing and weight criteria for small spacecraft and the lack of a truly homogeneous porous emitter material. Lacking fluid control in these thrusters can lead to excess propellant delivery to the surface of the thruster emitter, flooding and potentially shorting the entire thruster. Use of mechanical valves and flow regulators outweigh the benefits of having such a small electric thruster in the first place. Previous work on an electrowetting valve provided a single-use activation barrier to prevent propellant from flooding the thruster's emitter prior to launch and shorting the thruster entirely. The next reasonable evolution in this propellant management area is to attain fully active control of the ionic liquid propellant in a manner analogous to conventional mechanical valves in pressurized systems. Open microfluidics are microfluidics where one surface of the liquid is unconstrained at all times. Electrowetting provides the ability to manipulate liquid wetting characteristics actively with the application of an electric potential. Combining the transport of liquids via capillary flow in open microchannels with the ability to manipulate liquid contact angle via electrowetting, a solid-state electrostatic liquid flow controller may be designed and built.

This thesis aims to tackle three primary contributions seen as improving on the aforementioned shortcomings. First, the analysis of performance envelopes for an electrowetting flow control device. Second, design, fabrication, and testing of the devices to compare with model predictions. Third, creating a new emitter material to couple with the flow controller in order to mitigate uncontrolled flow to the emitter tips. This research will shed light on the many variables at play in achieving active flow control in electrowetting open microfluidics. These analyses will grant insight into designing and fabricating micro-devices to be tested in the lab in order to verify the models. A new porous emitter material will aim to address issues with emitter uniformity that are seen in current materials, also lending to mitigation of tip flooding. A solid-state propellant management device may be coupled with future electrospray

thrusters based on this thesis research.

Thesis Supervisor: Paulo C. Lozano
Title: M. Alemán-Velasco Professor of Aeronautics and Astronautics, MIT

Acknowledgments

First and foremost, I would like to thank my advisor, Prof. Paulo Lozano for his countless hours of academic and personal guidance during my years at MIT. His seemingly endless love for the field of space propulsion and aerospace as a whole has kept my motivation at the levels constantly needed to maintain quality research.

To my fiancé and personal editor, Haley, there has never been a person I have relied more heavily on during the lows and highs of graduate academic research. Your attitude towards life and the importance of friends and family have kept me faithful in the pursuit of prioritizing family and loved ones with a demanding career. Your ability to take the numerous inequities life throws at you in stride has provided me with a wholly new perspective of the value of true perseverance. You have my love and admiration forever.

To my committee and readers, your feedback has been extremely valuable in the course of my research and has made me not just a better scientist, but a better critical thinker with an improved eye for truth.

To the many staff of MIT nano and the former MTL facilities, you all keep the field alive every single day. Whether its that pesky tool that broke because a wafer got stuck in it, an acid spill, or someone just forgot their safety glasses, you all keep the wheels from squeaking too loudly and it has been deeply appreciated! Your insights on my fabrication processes have proven invaluable as your combined knowledge of simplified fab steps that produce reliable results led me to the final test devices that fundamentally proved my hypothesis.

Additional thanks to Shaymus Hudson for his help in running many Vickers Hardness Tests all throughout the busy academic terms. We would never know what "it feels pretty sintered" actually means in quantifiable terms without you.

To Prof. Ken Brakke, your many messages on the dynamics of open microfluidic flows and your incredible surface evolver software proved crucial to my research successes. Helping students visualize a particular phenomenon is invaluable and your program accomplishes that with ease! Additional thanks go to FLOW3D for provid-

ing an academic trial license to utilize their fluid dynamics simulation software used in this work.

This work was supported by the AFOSR under grant number FA9550-19-1-0104.

Contents

1 Introduction **23**

2 Literature Review **27**

2.0.1 Electrospray Propulsion 27

2.0.2 Microfluidics 30

2.0.3 Electrowetting 31

2.0.4 Open Microfluidics and Spontaneous Capillary Flow 36

2.0.5 The Electrowetting Flow Controller 45

2.0.6 Materials 47

2.0.7 Summary of Research Knowledge Gap and Contributions . . . 48

3 Electrospray Thruster Propellant Management **51**

3.1 Capillary Flows in Electrospray Thrusters 51

4 Design of an Electrowetting Flow Controller **57**

4.1 Performance Requirements for an Electrowetting Flow Controller . . 57

4.2 Open Microchannels 58

4.3 Numerical and Analytical Performance Modeling 65

4.4 Experimental Device Design Parameters 77

5 Fabrication Techniques for Experimental Electrowetting Flow Controller **81**

5.1 Conventional Fabrication Techniques 81

5.1.1 Machining 81

5.1.2 Stamping 82
5.1.3 3D Printing 85
5.2 Microfabrication 86
5.2.1 Binary Photolithography 86
5.2.2 Grayscale Photolithography 89
5.2.3 Resist Reflow 91
5.2.4 Deep Reactive Ion Etching 92
5.2.5 Isotropic Etching 98
5.2.6 Silicon Oxidation 98
5.2.7 Evaporative Parylene Coating 102
5.2.8 Hydrophobic Coatings 103
5.3 Fabrication of the Experimental Electrowetting Flow Controllers . . . 105

6 A Monodisperse Thruster Emitter Material 111
6.1 Material Formulation 111
6.1.1 Coloidal Silica Solution 113
6.1.2 UV Curable Resin Solution 113
6.2 Material Molding 114
6.3 Material Sintering 116
6.4 Material Thruster Integration 118

7 Experimental Methods 119
7.1 Flow Controller 119
7.1.1 Experimental Testing Set-up 119
7.1.2 Voltage Control and Data Logging 121
7.2 Monodisperse Emitter Thrusters 121
7.2.1 Vickers Hardness Testing 121
7.2.2 SEM Tip Profiling 122
7.2.3 Emission Current-Voltage Characterization 122
7.2.4 Time-of-Flight Mass Spectrometry 123

8 Data Analysis Methods 127
8.1 Flow Controller Data Analysis 127
8.2 Monodisperse Emitter Data Analysis 128

9 Experimental Results 131
9.1 Electrowetting Flow Controller 131
9.2 Monodisperse Emitter Thrusters 152
9.2.1 Material Characteristics 153
9.2.2 Laser Ablation of Emitters 155
9.2.3 Thruster Firing 158

10 Discussion 163

11 Future Work 167
11.1 Electrowetting Flow Controller 167
11.2 Monodisperse Porous Materials 168

12 Conclusion 171

A Time of Flight Post Processing 175

B Pressure Contours for Tested Liquids in Open Microchannels 179

THIS PAGE INTENTIONALLY LEFT BLANK

List of Figures

1-1 Emitter flooding limits thruster lifetime, stopping flow to the emitter via an active flow controlling device would prevent this. 26

1-2 Non-uniform porous emitter materials lead to less-than-optimal thruster performance, a material made of uniform nanoparticles will improve tip geometries and bulk material uniformity. 26

2-1 Diagram of an ion electrospray emitter tip extracting ions from an ionic liquid. 28

2-2 A PDMS-glass microfluidic device controlled via external flow control equipment. Source Elveflow 30

2-3 Electrowetting valve 34

2-4 Electrowetting droplet test 35

2-5 Setup for preliminary valve tests 35

2-6 Sketch of a generalized uniform open microchannel with an advancing meniscus. [22] 38

2-7 Concept for open channel electrowetting flow regulator. Left: voltage applied, contact angle allows channel to wet, feeding thruster emitter. Right: voltage removed, contact angle forces liquid to segment, dewetting thruster emitter. 46

2-8 Box diagram highlighting the shortcomings of other fluid management mechanisms in the scope of electrospray thruster propellant requirements. 47

3-1 A diagram of the fluid path for electrospray thrusters from the propellant reservoir up to the porous thruster emitter. 52

3-2 Surface Evolver simulation of a hexagonally packed group of cylinders experiencing "emitter flooding." Left: Contact angle of 10 degrees allows capillary flow up cylinders. Right: Contact angle of 65 degrees prevents capillary flow up cylinder. 53

3-3 Left: top-down view of actual emitter tips flooding with propellant. Right: Surface Evolver simulation of propellant flooding effect between emitter tips modelled as cylinder. 53

3-4 A "flooded" thruster emitter. Note the meniscus formations between tips and the extractor as highlighted by the red arrow. 54

4-1 Expected normalized pressure contour for a 100 micron wide rectangular channel with varying depths using EMI-BF4. Note the highlight of the 1.6 aspect ratio point highlighting the onset of SCF for a liquid-wall contact angle of 76 degrees. 63

4-2 Surface Evolver simulated meniscus morphologies in open microchannels. Left:liquid pinning to the ledges of a rectangular microchannel. Right: Liquid meniscus freely terminating at its contact angle with the rounded channel wall. 64

4-3 Expected liquid penetration distance vs time for EMI-BF4 in a variety of rectangular microchannels. 66

4-4 Expected liquid penetration distance vs time for EMI-BF4 in a variety of rectangular microchannels coated with an oxygen-plasma-treated spin-coated fluoropel layer. Note that with only an 8 degree decrease in contact angle, necessary aspect ratio decreases from slightly above 4 down to 2. All channel depths are fixed at 400 micron, aspect ratio is varied by channel width. 67

4-5 Expected liquid penetration distance vs time for EMI-IM in a variety of rectangular microchannels 400 micron deep. 68

4-6 Expected liquid penetration distance vs time for EMI-IM in a variety of rectangular microchannels 200 micron deep. 69

4-7 Expected liquid penetration distance vs time for DI water in a variety of rectangular microchannels 400 micron deep. 70

4-8 Expected liquid penetration distance vs time for DI water in a variety of rectangular microchannels 200 micron deep. 71

4-9 Expected liquid penetration distance vs time for 80% water 20% IPA by volume in a variety of rectangular microchannels 400 micron deep. 72

4-10 Expected liquid penetration distance vs time for 80% water 20% IPA by volume in a variety of rectangular microchannels 200 micron deep. 73

4-11 A rounded open microchannel 100 micron wide by 300 micron deep with an infinite upstream reservoir of water at zero pressure. This numerical simulation is run as a comparison to the MLW liquid filament propagation length vs. time. 74

4-12 A comparison of the liquid phase boundary front propagation down an open rectangular microchannel of 100 micron width and 300 micron depth with water. Both MLW analytical and FLOW3D numerical simulation data is plotted. 74

4-13 Segmentation of a liquid water filament in a hydrophobic open microchannel 100 micron wide by 300 micron deep. Note that the curvature of the meniscus is ever so slightly convex (Cassie angle of approximate 106 degrees) indicating the desired positive pressure in the channel region. 75

4-14 Segmentation of a liquid water filament in a hydrophobic open microchannel 100 micron wide by 300 micron deep. Relative pressure boundary condition at right end of channel is -1000 Pa. 75

4-15 Left:Surface Evolver showing two cylinders too far apart to initialize capillary flow. Right:Surface Evolver showing two cylinders close enough together to initialize capillary flow. 76

4-16 A 2D design of an open microchannel device with 2 circular reservoirs at either end. 77

4-17 A rounded open microchannel with a hydrophobic region located in the central region (yellow) and hydrophilic regions on either end (gray.) 78
4-18 Surface Evolver simulation of liquid flowing up to point of the hydrophobic region. 78

5-1 Several milled microchannels in an aluminum bar prior to sawing into individual devices. 82
5-2 A CNC milled steel positive microchannel device used to stamp softer metals. 83
5-3 A stamped copper substrate with the steel positive geometry transferred into the softer copper under 4000psi. 84
5-4 Profilometer results for the stamped copper microchannel. Note the extensive rounding of the channel edges. Also note the difference in axis scale in the cross-section measurement profile. 84
5-5 A 3D printed ABS plastic variant of the milled tool steel microchannel device. 85
5-6 Spin coating wafer with photoresist 87
5-7 SEM image of developed grayscale lithography "stairsteps." Image: SY Lee - Auburn University 89
5-8 Left: Grayscale multi-layer design file for simple stripes; total width is 100 microns. Right: Exposed and developed pattern viewed through microscope, note distinct lines correspond to different dose strips; total width is 100 microns. 90
5-9 Profilometer data for a grayscale test exposure of several differing-dosage strips in 10XT resist. 91
5-10 Microscope view of reflowed grayscale photoresist mask, note the lack of distinct dosage strip lines after reflow. 92
5-11 Profilometer data for a grayscale test exposure following a 60 sec 150C hot plate reflow. 93
5-12 DRIE etching of silicon via the Bosch process 94

5-13 SEM cross-section view of a partially etched microchannel using DRIE and binary lithography. Note the black line showing the remaining thin film of photoresist at the top of the silicon wafer. 95
5-14 Grayscale exposure photoresist mask atop a silicon wafer. Devices are 100 micron wide microchannels 5mm long with two 5mm diameter reservoirs at either end. 96
5-15 Top down microscope image of the grayscale device mask. Note the "cornrow" features that remain atop the 5 micron thick region of the grayscale photoresist mask even after reflow of the resist. 96
5-16 Etched grayscale photoresist mask. Note that some devices reached the silicon layer before others due to photoresist being slightly thicker in the lower half of the wafer. 97
5-17 Profilometer data of the etched grayscale lithography devices. Note the transfer of the small "cornrow" features in the resist scaled up by the etch selectivity ratio. 97
5-18 Wafers entering a thermal oxidation tube 99
5-19 SEM cross-section view of a DRIE etched and subsequently cleaved rounded-microchannel corner. A 2 micron thermal oxide layer is grown into the silicon then etched away with a buffered oxide etch to leave a rounded ledge. 101
5-20 Open microchannel devices after coating with parylene via CVD. . . 102
5-21 Depositing a thin film of hydrophobic C4F8 fluoropolymer using the passivation step of a DRIE etch process. 104
5-22 Aluminum microchannels inside of a sputter chamber attached to a rotating planetary stage. 105
5-23 Silicon microfluidic device after spin coating with a fluoropolymer solution. 106
5-24 Fabrication cross-section evolution of the electrowetting test chip. . . 106
5-25 Fabrication cross-section evolution of the test electrowetting flow controller devices. 107

5-26 Left: masked device with photoresist coating atop the dielectric layer. Right: Post-development resist mask shows empty region where UV flood exposure occurred. 108

6-1 Current emission heat map from an electrospray emitter array. Note certain tips emit more ion current than others. [45] 112

6-2 PDMS mold with 12 emitter chip wells. 115

6-3 Curing chip greens under UV light source 115

6-4 Cured chip greens prior to sintering. 116

6-5 Sintering temperature profile. 117

6-6 Sintering temperature ramp rates and hold times. 118

6-7 Chips greens in the sintering furnace atop a platinum sheet to avoid reactions with furnace walls. 118

7-1 Experimental diagram for filming electrowetting flow control devices. 120

7-2 Emitted and intercepted current vs applied voltage for an ion electrospray thruster. 124

7-3 Time of flight data for electrospray ion emission. Note the stair steps corresponding to monomer and dimer species with sloped regions showing fragmented species. 125

8-1 Contact angle measurement for a droplet of water on a hydrophobic surface. 128

9-1 Preliminary electrowetting curve for DI water on the trichlorosilane hydrophobic treatment on a silicon-silicon dioxide chip. Note the large hysteresis in the angle restoration. 132

9-2 Electrowetting curve for DI water and EMI-BF4 on a PECVD fluoropolymer hydrophobic coating. Note the narrow range of angle change for EMI-BF4. 133

9-3 Electrowetting curve for droplets of DI water and EMI-BF4 on a silicon-silicon dioxide chip coated with Fluoropel. Note the addition of the Young-Lippman curve to the EMI-BF4 data to show where saturation begins. 133
9-4 Electrowetting curve for droplets of EMI-BF4 and EMI-IM ionic liquids on a Fluoropel coated test chip. 134
9-5 Cyclic electrowetting actuation of EMI-IM and EMI-BF4 droplets on Fluoropel. 120 VDC is applied and removed multiple times to measure any degradation in contact angle restoration. 135
9-6 Electrowetting curve for EMI-BF4 and water atop an O2 plasma treated fluoropel hydrophobic coating. 136
9-7 Electrowetting curve for a mixture of 80% water with 20% IPA by volume atop a fluoropel hydrophobic coating. Note the negligible angle hysteresis for this mixture. 137
9-8 Electrowetting curve for a mixture of 50% water with 50% Glycerol by volume atop a fluoropel hydrophobic coating. Note the very similar range as pure water. 138
9-9 Electrowetting curve for EMI-BF4 on an O2 plasma and SF6 plasma treated parylene C hydrophobic layer. 139
9-10 Cyclic electrowetting of O2 and SF6 plasma treated parylene coating with EMI-BF4. 139
9-11 Cyclic electrowetting of O2 plasma treated Fluoropel coating with EMI-BF4. 140
9-12 EMI-BF4 undergoing SCF into a plasma-treated fluoropel coated channel. Channel width is 100 micron and depth is approximately 300 micron. Note the clear meniscus pinning along the sharp ledge of this particular device. 141
9-13 MLW approximation vs experimental test results of SCF wetting in open rectangular microchannels with a mixture of 80% H2O and 20% IPA by volume. 141

9-14 MLW approximation vs experimental test results of SCF wetting in open rectangular microchannels with a mixture of 50% H2O and 50% Glycerol by volume. 142
9-15 MLW approximation vs experimental test results of SCF wetting in open rectangular microchannels with EMI-IM. 143
9-16 MLW approximation vs experimental test results of SCF wetting in open rectangular microchannels with EMI-BF4. 144
9-17 MLW approximation vs experimental test results of SCF wetting in open rectangular microchannels with H2O. 145
9-18 Two reservoir device with hydrophobic coating strip in middle, note that the liquid in the reservoirs stops at the hydrophobic region in the channel. 147
9-19 Two reservoir device with hydrophobic coating strip in middle and emitter material at end of channel. 147
9-20 EMI-BF4 in a two reservoir device with hydrophobic coating strip in middle and emitter material at end of channel undergoing SCF via electrowetting. 148
9-21 Liquid filament depletion and segmentation without application of voltage to device. 149
9-22 EMI-BF4 filament depletion and segmentation shown at an angle. The divit is the light gray region in the center of the channel where the hydrophobic coating is. The EMI-BF4 filled reservoir is at the right and saturated emitter material reservoir is at the left. 150
9-23 Water filament depletion and segmentation without application of voltage to device. 151
9-24 DI water wets up to the central hydrophobic strip on a cylindrical capillary electrowetting device. Once the 100VDC is applied between the two cylinders and the liquid reservoir, the contact angle drops below the wetting threshold for the hydrophobic region, due to electrowetting, and flow along the rail toward the filter paper. 151

9-25 So long as voltage is applied between the cylinders and the liquid reservoir, liquid continues to flow into the filter paper until it is saturated. 152
9-26 Once voltage is removed, the hydrophobic contact angle restores in the fluoropel region, causing the liquid to form a capillary instability and segment between the filter paper and reservoir ends of the rails. . . . 152
9-27 SEM image of 75 percent mass loading fraction after 1160°C sintering 153
9-28 Vickers hardness test values under 300 gram force. Note no hardness value was determined for the 1120°C as it was just barely sintered and crumbled under any measurable load. 154
9-29 Vickers hardness test values under 300 gram force on samples held at peak 1200°C sintering temperatures for varying times. Note the clear increase in hardness as the hold time is increased. 154
9-30 Laser ablated emitter tip array JG4-2. 156
9-31 Tip profile of JG4-2 emitter, note well-rounded tips, but rather blunt. 156
9-32 Laser ablated emitter tip array JG4-3. 156
9-33 Laser ablated emitter tip array JG6-2, note smaller 750nm diameter nanoparticles are used here. 157
9-34 Laser ablated emitter array JG4-4. 157
9-35 JG4-4 emitter tip, note very sharp profile with <5 micron radius of curvature. 157
9-36 JG4-3 voltage-current relation. 159
9-37 JG4-3 time-of-flight mass spectrometry. 159
9-38 JG4-3 time-of-flight derived performance metrics. 159
9-39 JG4-4 Voltage-Current relation. Note I1 corresponds to emitted current and I3 corresponds to current intercepted by the extractor grid. . 160
9-40 JG4-4 time-of-flight mass spectrometry. 160
9-41 JG4-4 time-of-flight derived performance metrics. 160
9-42 JG4-2 emission current-voltage data. 161
9-43 JG4-2 TOF data. 161
9-44 Derived performance metrics for JG4-2 161

9-45 Liquid shorts (dark spots) in JG4-2 after firing for 30 hours. 162
9-46 Lifetime current emission-voltage data for JG4-2. Note shorts developed just prior to 30 hours and are truncated to see hour marks. . . . 162

B-1 EMI-IM pressure contours for varying depth microchannels based on a range of contact angles and channel depths. Note that not all contact angles are achievable, the range is physically set by the hydrophobic coating used for electrowetting. 180
B-2 Water pressure contours for varying depth microchannels based on a range of contact angles and channel depths. Note that not all contact angles are achievable, the range is physically set by the hydrophobic coating used for electrowetting. 181
B-3 80% Water/ 20% IPA by volume pressure contours for varying depth microchannels based on a range of contact angles and channel depths. Note that not all contact angles are achievable, the range is physically set by the hydrophobic coating used for electrowetting. 182

List of Tables

4.1 Liquid Properties 65

THIS PAGE INTENTIONALLY LEFT BLANK

Chapter 1

Introduction

Ion electrospray sources are a low-mass and low-power propulsion option for spacecraft. Ionic liquids are fed into tiny porous conical tips where the positive and negative ions are extracted from the liquid by an electrode held at a high positive or negative voltage just above the tips. Prior to their launch as part of a spacecraft, these systems often stay in storage on the ground for long periods of time. The launch itself, in which rocket payloads are exposed to depressurization and various vibrational loads, is another harsh environmental test of the system's robustness. Given the scale of these thrusters being best suited for use on small spacecraft where volume is limited, traditional pressurized propellant management systems are not an option. Therefore, these electrospray propulsion systems rely solely on passive fluid flows from un-pressurized reservoirs. During these long ground storage periods and eventual rocket launch, robust propellant management would help mitigate propellant going where it should not. Ideally, propellant would remain in the reservoir until on orbit, where the propellant would then be directed to the porous emitter when ready to fire. Furthermore, if the propellant management system could stop flow to the thruster's emitter and restore flow as directed, the phenomenon known as "emitter flooding", whereby the propellant saturates the emitter and forms negative pressure menisci between the emitter tips, slowly crawling up the extractor electrode and shorting the thruster circuit, could be prevented. A combination of small-scale active propellant management and homogeneous porous emitter materials would serve to

prevent any propellant-related failure modes in future electrospray thrusters. This is the fundamental drive for this thesis research.

While single-use electrowetting capillary valves have been demonstrated [1] to provide an initial activation barrier to ionic liquids leaving the reservoir, such valves cannot isolate the liquid once wetted and it is unable to regulate the flow to the thruster. These features are important for two primary reasons. Once the liquid is delivered to the porous material, surface tension forces alone have the ability to pull the liquid such that the meniscus between emitter tips could potentially result in flooding. This effect has been observed in the laboratory setting during a thruster's initial firing up and could be more severe in the zero gravity environment of space, given the lack of gravity working against the meniscus movement. Flooding generally depends on the wetting state (contact angle) of the ionic liquid propellant with the substrate material, bubble formation, or gravity in the wrong direction. It is frequent enough, however, especially during long idle times between thruster firings, that a system to prevent it is necessary.

During thruster operation, propellant flow is governed by the traction force of the applied voltage and the device's hydraulic resistance and surface tension stress. A capability would be added if the flow rate could be actively controlled and even stopped altogether, similar to that of conventional pressurized propellant systems. If the hydraulic resistance between the propellant reservoir and emitter tips could be modified enough to initialize, regulate, or stop the liquid flow, this would achieve the desired level of control. A complementary approach to mitigate excess propellant flooding the emitter, is to modify the emitter material itself, providing more control over uniformity, porosity, and laser ablation of the tip structures. A more uniform material and better control over tip geometry will also lend to mitigating unwanted tip flooding and improve thruster performance and lifetime via improved tip profiles and flow traits as compared to commercially available porous materials currently utilized.

In this thesis work, a combination of open microfluidic flow dynamics and electrowetting coupled with a new, more uniform, monodisperse emitter material is shown to be a potential solution to this ongoing propellant management problem. By utiliz-

ing contact angle control from electrowetting and spontaneous capillary flow in open microfluidics, that remain un-pressurized relative to the environment, a new form of electrowetting liquid flow control can be attained for use in electrospray thrusters. By removing a surface from a closed capillary channel, the free surface energy and liquid pressure can be modified by changing the contact angle of the liquid and the channel walls via electrowetting analogous to a flow regulator's operation. Through modeling and experimental verification tests, this thesis research will characterize the operation and fluid dynamics involved in such a device in the lab environment and demonstrate physical feasibility of such a device for use in electrospray propellant management. The resulting device should be scalable in order to directly couple via propellant to the emitter material as part of a fluid system in the thruster. This highlights the importance of the emitter material as the other half of this fluid system. Addressing shortcomings in uniformity and tip geometry achieved from laser ablation was necessary to minimize variations in tip-to-tip ion emission. Casting silica nanosphere suspensions and sintering them can provide a macroscopic, monodisperse, porous emitter material that has excellent uniformity and sensitive laser ablation response as seen in prior work. [2].

To summarize, there exists two operational lifetime limitations in electrospray thrusters. The first is unwanted pooling of propellant around emitter tips, leading to "flooding" of the emitter and shorting the thruster circuit. The second is non-uniformities in emitter tips that lead to varied emission characteristics which can lead to shorter operational lifetimes. The proposed solutions are the implementation of a flow controller to stop flow and start flow to the thruster emitter as needed to prevent flooding and the development and implementation of a monodisperse emitter material to improve emitter tip geometries as well as bulk porous material uniformity compared to prior porous glass emitter materials. These two solutions are shown graphically in Figures 1-1 and 1-2.

The following section touches on the background and relevant literature pertaining to this thesis research.

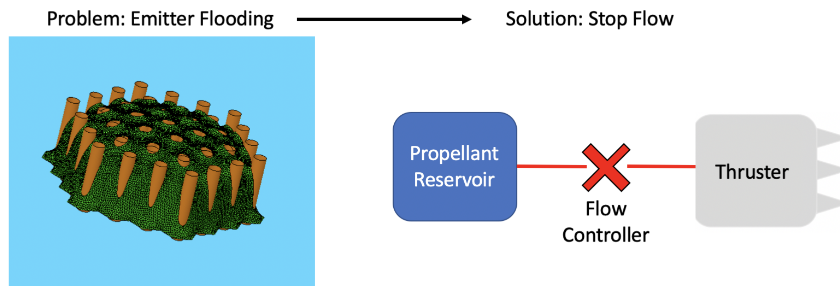

Figure 1-1: Emitter flooding limits thruster lifetime, stopping flow to the emitter via an active flow controlling device would prevent this.

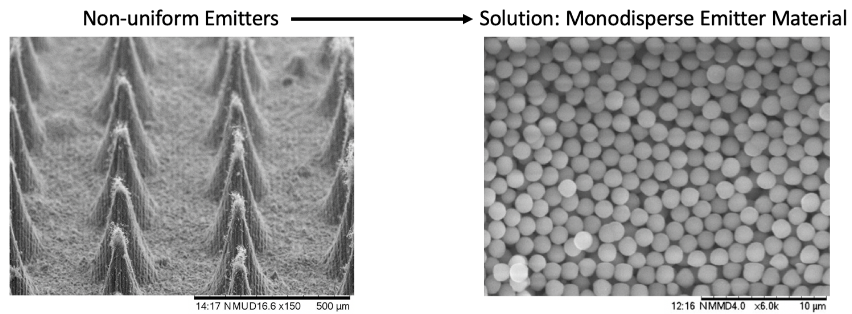

Figure 1-2: Non-uniform porous emitter materials lead to less-than-optimal thruster performance, a material made of uniform nanoparticles will improve tip geometries and bulk material uniformity.

Chapter 2

Literature Review

This thesis work spans the areas of electrospray propulsion, microfluidics, electrowetting, and material science. Works encompassing these areas are discussed below broadly with more focus on open microfluidic flow dynamics, electrowetting, and monodisperse porous materials. Research gaps from these overlaying topics will serve as the motivation for the contributions of this research discussed in later sections.

2.0.1 Electrospray Propulsion

Ion electrospray thrusters are an offspring of the ion engine family of electric spacecraft propulsion systems. Charged ions are accelerated by an electrical potential difference in order to produce thrust. In an electrospray thruster, the charged particles are extracted from an electrically conductive liquid such as an ionic liquid. Ionic liquid propellant, often 1-ethyl-3-methylimidazolium tetrafluoroborate (EMI-BF4) or 1-ethyl-3-methylimidazolium bis(triflouromethylsulfonyl)amide (EMI-IM), is fed to a porous chip called the emitter with multiple pointed conical tips on the order of a few hundred microns each on its surface. Each "emitter" chip hold hundreds of these tips to provide useful thrust via ion extraction and acceleration. A potential difference is applied between the propellant-saturated emitter and an extractor grid, essentially a high-voltage electrode with holes corresponding to each emitter tip location. The electric field around the emitter tips deforms the ionic liquid and creates a meniscus

where the pressure, surface tension, hydraulic pressure drop, and electrical pressure are balanced. The sharp tips on the emitter chip enhance the electric field strength to the point that ions in the ionic liquid can be extracted from the emitter and accelerated by the extractor electrode away from the thruster to produce a resulting thrust. A great deal of detail on the operation and underlying physics of electrospray thrusters can be found in these papers: [3], [4], [5]. This section simply serves to establish where this thesis research work fits in the aerospace realm.

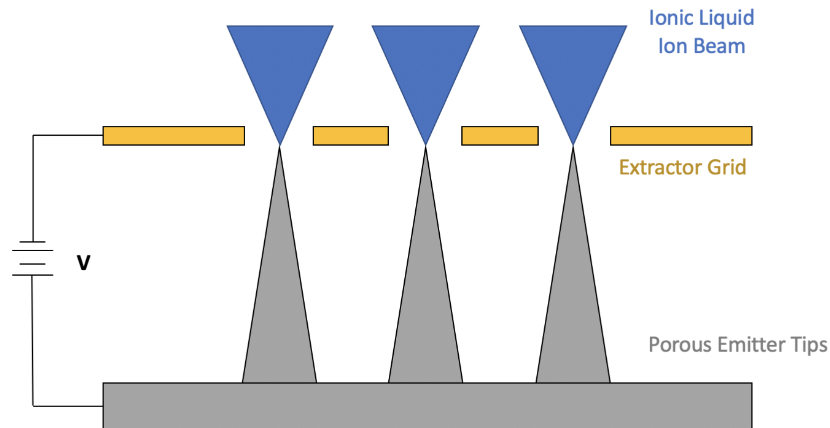

Figure 2-1: Diagram of an ion electrospray emitter tip extracting ions from an ionic liquid.

Figure 2-1 shows an ion electrospray emission diagram. Like most propulsion systems, electrospray thrusters are comprised of a propellant reservoir, a valve (although single use), and the thruster. The thruster is made of a silicon frame, the porous emitter chip with tips, and the extractor electrode. For the purposes of this work, we can consider the region from the neutral-pressure propellant reservoir up to the emitter chip as a microfluidic device where liquid control is provided by passive capillary forces using porous wicking materials and a porous emitter chip. In between the neutral pressure propellant reservoir and the porous emitter is currently a single-use electrowetting capillary valve that offers a one-time flow prevention barrier prior to firing the thruster. This system can also be open to the environment to prevent bubble formation in propellant lines due to the negligible vapor pressure of ionic liquids. [6], [7]

This work partly focuses on the next logical evolution of the electrowetting capillary valve: a fully reversible flow controlling microfluidic chip that can be used multiple times for active control of the propellant flow from reservoir to emitter. This capability would not only add a new dial to turn for thruster performance, changing flow rates to the emission site, but also add a layer of robustness to prevent the conductive ionic liquid from leaving the reservoir prematurely and shorting the thruster circuit. A final improvement this capability would add is the ability to mitigate tip flooding. "Emitter flooding", as discussed in the introduction, is when the conical tips of the emitter chip act as capillary rails between which a meniscus may climb towards to the extractor grid, shorting the thruster circuit. The emitter tips are essentially slightly tapered cylinders in a porous media, and as such, there is presumably some contact angle of liquid and separation between the tips that spurs the formation of a negative pressure meniscus between the tips that wants to propagate along the tips towards the extractor grid. This phenomenon has been witnessed in several laboratory thrusters and can often lead to a premature thruster failure if not addressed.

The ability to control propellant flow on command to the thruster emitter would effectively cut the supply of liquid and stop flooding from occurring. Although, not the only solution, another solution could involve negative pressure on the backside of the emitter equal to the capillary pull of the porous emitter when energy is zero. That being said, segmenting the liquid bridge between the reservoir and emitter would be the simplest form of active propellant flow control. Additionally, the porous emitter material itself plays a crucial role to both ion emission as well as flow management. Thus, the secondary focus of this work is evolving the materials research in [2] to achieve a monodisperse porous material to replace the polydisperse porous materials currently used for electrospray emitters. The following sections will discuss the individual concepts and backgrounds pertaining to the aforementioned details.

2.0.2 Microfluidics

Microfluidics is a broad term generally used to classify a device that is able to manipulate fluid flows or fluid motions in the sub-millimeter scale. While not a new technology, microfluidics are seeing widespread integration across new areas in biotechnology, chemical engineering, and remote sensing. This is not to turn a blind eye to the fact that nature has been utilizing "microfluidics" for millions of years in the form of leaf veins, spider spinners, and numerous other uniquely evolved scenarios. At the turn of the 20th century, Washburn's capillary equation simply described the depth of liquid penetration into a capillary orifice. In order to change the height or motion of the meniscus in such a setup, external pressure must be applied. In most contemporary applications, the actuation of liquid flow in closed microfluidics, such as capillary tubes or Polydimethylsiloxane (PDMS) microchannels, is implemented either by external pressure sources, external mechanical pumps, or integrated mechanical micropumps [8]. These flow controlling techniques are needed for continuous flow and droplet generation applications that are two common threads in microfluidics. While very effective at the lab-scale, these closed, pressure-driven microfluidic devices do not scale well for use in the space domain where every gram and milliliter count.

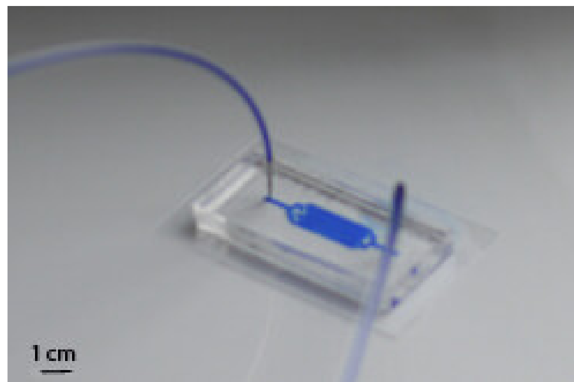

Figure 2-2: A PDMS-glass microfluidic device controlled via external flow control equipment. Source Elveflow

The bulk of microfluidic devices that emerged in the 2000s were closed channel PDMS-on-glass devices, mostly due to their ease of manufacture compared to earlier

micromachined devices. The PDMS is impressioned using any number of thin film MEMS photolithography techniques to achieve channel geometries typically in the tens of microns in size. Once treated with a plasma, silanol groups are increased at the surface where they can form covalent bonds with glass, thus creating closed microchannel devices with inlets and outlets removed in desired locations along the fluid path(s). [9] While this manufacturing technique is very versatile, these closed geometries rely on external equipment to sustain fluid flows in the devices. This equipment is often some form of table-top pressure or flow-rate regulating device that is connected to the microfluidic device's inlets and outlets. Given that this research seeks to create a microfluidic device that can be scaled to act as a propellant management device for ion electrospray thrusters, these external systems put relatively large constraints on scalability. A solid-state, possibly electrical method of control would aid in this scalability and system-integration goal.

2.0.3 Electrowetting

Electrowetting is the phenomena by which the contact angle (angle formed between a liquid and a solid substrate) of a liquid is altered via application of an electric field. More specifically, the traditional electrowetting case describes an electrolytic liquid on top of a hyrdrophobic dielectric layer which is, in turn, on top of a conductive substrate. An electrical potential is established between the electrolytic liquid and the conductive substrate. The changing of the contact angle via electrowetting can be understood from a thermodynamic perspective. The free energy of this system is dependent on an electrical energy term. This electric term is the energy stored in the capacitor that is created between the conductor and the electrolyte droplet on top of the hydrophobic dielectric layer. By modifying the energy of the capacitor system, changes to the surface interface occur.

This relation between the modified contact angle and the energy change in the capacitor due to the a change in voltage is shown in the Young-Lippmann equation:

$$\cos\theta = \cos\theta_0 + \frac{\epsilon_0\epsilon}{2\gamma d}V^2 \tag{2.1}$$

In this equation, θ is the modified contact angle of the electrolyte on the hydrophobic dielectric, θ_0 is the unmodified (no electric field) contact angle between the electrolyte and the hydrophobic dielectric, ϵ_0 is the permittivity of free space, ϵ is the dielectric permittivity, γ is the surface tension of the electrolyte liquid, d is the dielectric thickness, and V is the voltage applied between the conductor and the electrolyte. For more detailed information on electrowetting and the underlying physics involved, these papers provide useful insights: [10], [11].

Within the scope of this thesis, electrowetting as a concept is understood well, but the reversibility, hysteresis, and voltage-limit/contact angle saturation phenomena require a bit more detail for use in microchannels and microgrooves. Superhydrophobic coatings (coatings that produce a contact angle of >90 degrees with water) have shown minimal hysteresis in reversible electrowetting applications including those utilizing ionic liquids. This has been shown via numerical modeling as well as experimentally. [12], [13], [14] There are many papers out that propose solutions to reversible electrowetting with minimal hysteresis, however the bulk of them focus on simplified electrowetting on dielectric (EWOD) devices. These are devices that typically only alter droplets or small liquid volumes, rather than offering controllable, continuous flow as is the goal of this work. While discrete droplet control is also feasible, it would require dedicated hardware to drive the multiple electrodes necessary to step droplets around on a surface. It also introduces more points of failure into an already complex system and severs the electrical circuit between the distal electrode in the propellant reservoir and the thruster's extractor electrode, requiring a new electrode scheme. Nonetheless, the points on mitigating surface roughness and chemical contamination to minimize hysteresis losses in reversible electrowetting likely apply to all device geometries.

Contact angle saturation is another aspect of electrowetting that the Young-Lippmann equation, in all of its usefulness, fails to predict. At low electric field

strengths and lower contact angle changes, the Young-Lippmann relation holds true. However, at higher field strengths, the contact angle saturates. Previous publications attempting to explain this effect have considered many causes including: charge trapping in the dielectric layer, [15] solid-liquid interfacial surface energy, [16], [17] large electric field strengths at the contact line, [18] and generalized free energy. [10] While these papers come close to experimental agreement in some domains, none of them effectively explain the contact angle over both the low and high voltage ranges where divergence from the Young-Lippmann model occur.

One particularly promising model to explain this saturation pertains to dipole polarization due to the applied potential difference. [19] This model shows much better agreement with experimental results than the Young-Lippmann model at high voltages, and predicted the observed asymmetry between high and low voltage regions. The authors attribute the better agreement with the experimental results to the influence of polarization on the surface energy. While these past publications shed light on contact angle saturation effects on typical single droplet electrowetting, none of the publications consider continuous flow applications or microchannel device geometries. These changes should not, in principle, alter the underlying physics, but for thoroughness, this difference should be noted. For the goals of this research, diving into underlying causes of contact angle saturation are neglected in favor of repeated testing within the limits of saturation.

Electrowetting Valve

As mentioned prior, a microcapillary ionic liquid electrowetting valve was developed by Freeman [1]. This single-use valve would serve as removable barrier to ionic liquids leaving the propellant reservoir prior to thruster firing. The valve is an array of through-holes etched in a 650 μm silicon wafer to form thousands of capillaries prior to thermally growing a silicon oxide layer on the wafer. Each diced valve chip is then coated with a fluoropolymer similar to Teflon via a PECVD (plasma enhanced chemical vapor deposition) to act as the hydrophobic dielectric layer. The hydrophobic layer prevents the capillaries from wetting until a voltage is applied, lowering the

contact angle of the ionic liquid enough to saturate the capillaries, causing liquid to flow to the other side of the chip into the emitter of the thruster. The high contact angle of a water droplet deposited on top of a finalized valve can be seen in Figure 2-3. This valve serves as the basis for this thesis research.

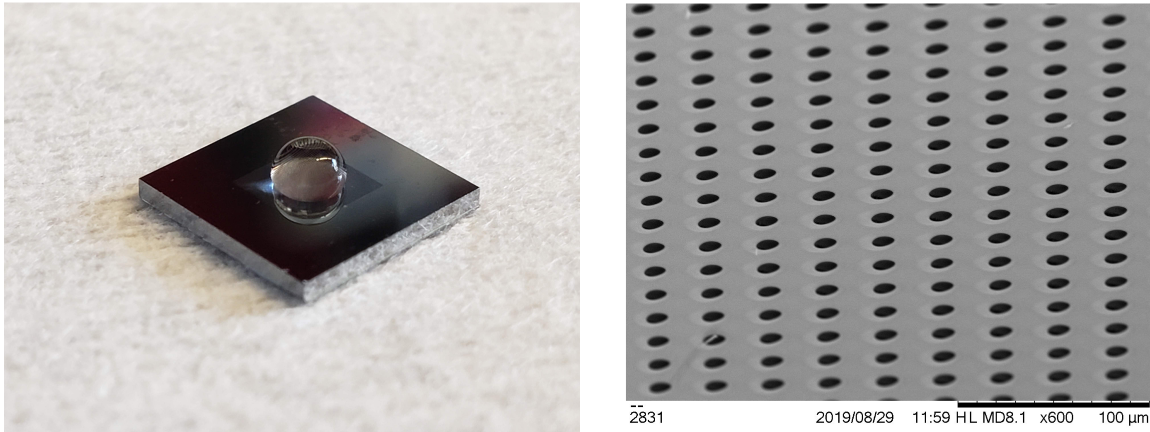

Figure 2-3: Left: Electrowetting valve displaying its hydrophobic nature with a water droplet. Right: An SEM image of an array of through-holes

To characterize the electrowetting contact angle change expected with the single use valve's oxide and hydrophobic dielectric layers, a flat chip with the same oxide and fluoropolymer was tested with water. A small droplet of water was placed on the center of the sample. The silicon side was used to ground a high-voltage power supply. The positive electrode from the supply was connected to a thin conductive wire placed in the water droplet without touching the silicon. The bias was increased between the droplet and the silicon in 5 volt increments up to 100 volts. This droplet experiment is shown in Figure 2-4. The droplet contact angle begins at greater than 90 degrees, but decreases to 90 and surpasses the wetting threshold as voltage increases. The wetting voltage (whereby the angle crosses this 90 degree threshold) was measured to be approximately 40 volts. [20]

The basic circuit formed in this test of the single-use electrowetting valve is shown in Figure 2-5. [1] This circuit is a very basic electrowetting setup and was utilized as a baseline for this thesis research on reversible electrowetting devices. It also simplifies the flight system and utilizes the current power supply that drives the thrusters themselves with only the addition of an additional switching point for software to

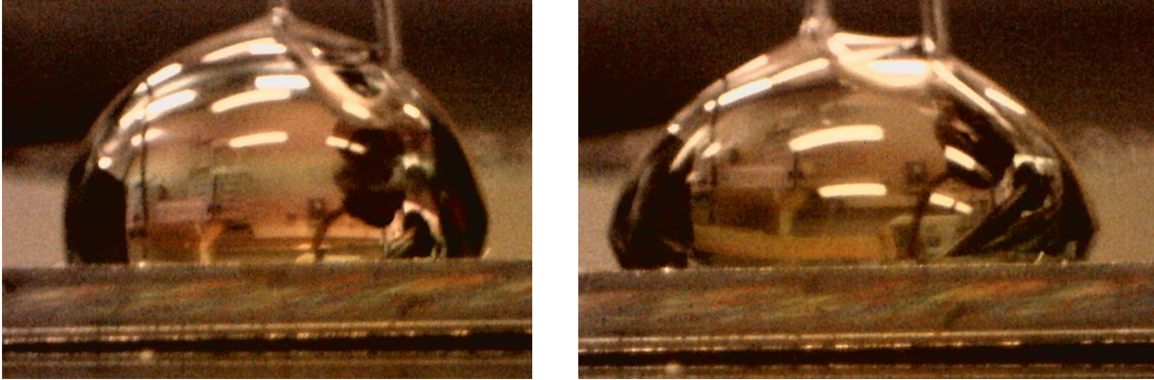

Figure 2-4: Electrowetting droplet test; left is droplet with 0 Volts applied and right is with 40 V applied.

[2]

drive the valve.

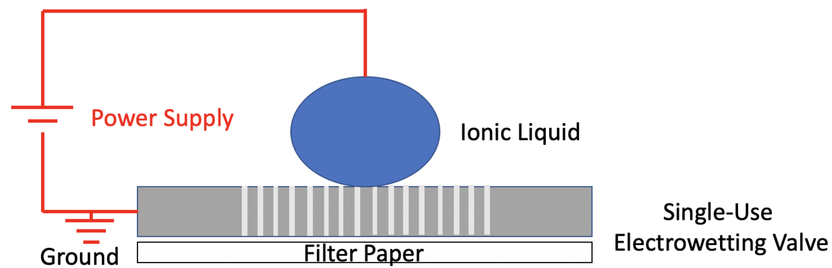

Figure 2-5: Setup for preliminary valve tests.

While this electrowetting valve served its purpose well, the closed capillary tubes, once wetted, are unable to de-wet. This is due to fact that there is no longer a fluid front or free liquid surface once propellant has filled the capillary completely between the reservoir and the thruster via the valve. However, the lessons learned about oxide thickness and hydrophobic coating resilience is still relevant to this thesis research work.

Electrowetting Pumps

While micro-pumps are also no recent discovery, they are typically referred to in two categories: mechanical and non-mechanical. Mechanical pumps exert force on a fluid by moving one or more boundaries, similar to conventional mechanical pumps just

much smaller. Non-mechanical pumps add momentum to the fluid by converting another energy form into kinetic energy. [21] There are successful developments of both categories. However, a similar electrically controlled non-mechanical micropump (the electroosmotic pump) has fundamental limitations on liquid chemistry and runs the risk of electrochemistry effects with ionic liquids around the electrodes.

2.0.4 Open Microfluidics and Spontaneous Capillary Flow

Open microfluidic devices are defined as having at least one boundary of the system removed, exposing the fluid to air or another interface (liquid or vacuum). Advantages of open microfluidics for this thesis research include a free surface where contact angle can directly alter meniscus shape and therefore the pressure in the microchannel liquid. [23] Just like closed microfluidics, surface tension driven flows are easily achieved in open microchannels. [22] Such a flow eliminates the need for external mechanical pumping methods such as peristaltic or syringe pumps. Open microfluidic devices are also easy and inexpensive to fabricate by milling or standard microelectromechanical (MEMS) fabrication techniques with a variety of materials. Examples of open microfluidic devices include open-channel microfluidics, rail-based microfluidics, paper-based microfluidics, and thread-based microfluidics. [24] These devices are not without disadvantages however, some worth noting include susceptibility to evaporation (although not for ionic liquids), contamination, and flow rate limitations. [25] Given the application of this research being in space with ionic liquids, limited flow-rate is really the only obstacle for this class of microfluidics to being utilized in ion electrospray thrusters effectively, although that can be addressed by scaling the channel dimensions appropriately. This scaling is even more forgiving when considering the lack of gravity and atmosphere in space. One open question is: how does microchannel geometry and voltage correlate to repeatable pressure change and can "macro"fluidic channels work in the absence of gravity?

In open channel microfluidic devices, fluids can be driven solely by surface tension under Spontaneous Capillary Flow (SCF) conditions. [22], [26] SCF occurs when the pressure at the advancing meniscus is negative. [22] Assuming channel walls are

smooth, uniform cross-section, and at least partially open to the surrounding atmosphere, and temperature is constant in the channel, a simple equation derived from Gibbs free energy dictates wetting condition based on the summed contributions of surface tension at all interfaces. The only needed conditions are for capillary forces to dominate all others and for low Reynolds number flows (laminar) as often seen in microfluidics. The geometry of the channel and contact angle of fluids has been shown to produce SCF if the following general condition is met:

$$\frac{p_f}{p_w} < cos(\theta) \tag{2.2}$$

Where p_f is the free perimeter of the channel (the interface not in contact with the solid channel wall), and p_w is the wetted perimeter (the channel wall surfaces in contact with the fluid), and θ is the contact angle of the fluid on the material of the channels. [22], [27] This is a direct consequence of calculating an infinitesimal change in the Gibbs free energy:

$$dG = \sum(\gamma_i dA_i) - pdV - SdT \tag{2.3}$$

where G is the Gibbs free energy, A; the liquid boundary areas, γ the liquid surface tensions, V the liquid volume, p the liquid pressure, S the entropy and T the temperature. Assuming the volume is constant and that the system will evolve towards a state of lower energy:

$$dG = \sum(\gamma_i dA_i) < 0 \tag{2.4}$$

The morphology of the free liquid surface is such that it evolves to reduce the Gibbs free energy G. As a simple example, consider a uniform channel with a single contact angle and open to the environment as shown in Figure 2-6.

Flow of liquid into the channel should occur as long as the pressure at the front of the flow is less than that of the reservoir when:

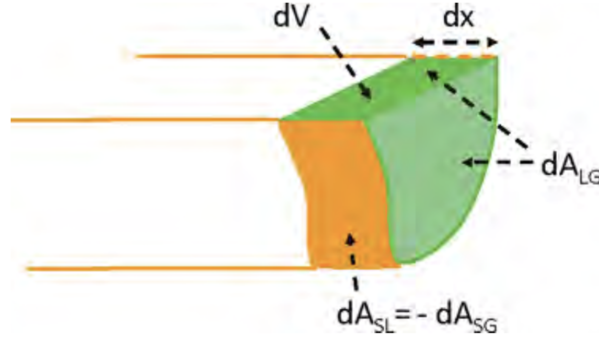

Figure 2-6: Sketch of a generalized uniform open microchannel with an advancing meniscus. [22]

$$\frac{dG}{dV} = \sum(\gamma_i \frac{dA_i}{dV}) < 0 \tag{2.5}$$

The i index accounts for the summed contributions from all surfaces A_i with corresponding γ_i which results in the following:

$$\sum(\gamma_i \frac{dA_i}{dV}) = \gamma_{SG}\frac{dA_{SG}}{dV} + \gamma_{SL}\frac{dA_{SL}}{dV} + \gamma_{LG}\frac{dA_{LG}}{dV} < 0 \tag{2.6}$$

This can be further reduced by substituting Young's equation $\gamma_{LG} cos\theta = \gamma_{SG} - \gamma_{SL}$ and taking into account that $dA_{SG} = -dA_{SL}$, we are left with:

$$\frac{dA_{LG}}{dV} < cos\theta \frac{dA_{SL}}{dV} \tag{2.7}$$

For continuous cross-section channels, the area terms are simply the 2D perimeter multiplied by the channel length. Since the length terms are on both sides of the equation, this further reduces to:

$$\frac{p_f}{p_w} < cos(\theta) \tag{2.8}$$

Another crucial equation for open microchannel flow dynamics is the change in Laplace pressure of the liquid meniscus that forms in the channel with respect to an upstream neutral pressure reservoir. Borrowing from the Delamarche derivation for

pressure of a liquid inside of a confined rectangular capillary channel:

$$\Delta P = \gamma(\frac{cos\theta_r + cos\theta_l}{w} + \frac{cos\theta_b + cos\theta_t}{h}) \tag{2.9}$$

where $\theta_r, \theta_l, \theta_b$, and θ_t correspond to the contact angle of the liquid with the rectangular channel right, left, bottom, and top walls respectively. For the case of an open rectangular channel with uniform walls (and an assumed negligible curvature along the free surface that was the "top" of the confined channel), this equation reduces to a simplified:

$$\Delta P = \gamma(\frac{2cos\theta}{w} + \frac{cos\theta}{h}) \tag{2.10}$$

assuming that the top surface corresponds to the free surface where the liquid is effectively having a contact angle of 180 degrees.

Microfluidics simulation via numerical modeling is also quite useful as a tool for predicting fluid flow characteristics through channel geometries. One particularly relevant example is a paper on adaptive meshing techniques for simulating capillary flow in basic open microchannel geometries. [28] This paper describes an adaptive meshing scheme that has shown good promise as a baseline for this thesis research given the similar spontaneous capillary flow criteria. As helpful as numerical simulation can be for visualization, they are only as good as the initial and boundary conditions given to them in addition to the meshing and solving scheme. Therefore, an analytical model is needed too.

From an analytical standpoint, research in capillary flows in hydrophobic microchannels has also been published. [29], [26], [30] By analytically solving the Poisson equation with general Navier-slip boundary conditions, the authors obtained the most general forms of velocity distributions, flow rate, friction factor and Poiseuille number for open and closed hydrophobic microchannels. This is to say, there are many tools available for estimating the expected dynamics of an electrowetting flow controller device, but this approach, generally referred to as the Modified Lucas-Washburn approach is well-suited for the case of open rectangular channels with aspect ratios

greater than or equal to one and utilizing liquids with contact angles above 45 degrees when Concus-Finn filaments do not form.

Following a the approach used in [26] and the previously derived relation between interface perimeters and free energy and contact angle, a derivation of the expected liquid-gas meniscus front velocity down the channel can be attained. We first start with the capillary driving force, calculated from the changing free energy of the liquid-channel system as it progresses down the channel. This change in the system's free isothermal Gibb's free energy G due to the liquid progressing down a length x of the initially empty channel is given by:

$$G = A_l\gamma_{LG} + (\gamma_{SL} - \gamma_{SG})A_{SL} + E_m = \gamma_{LG}(A_{LG} - A_{SL}cos\theta) + G_m \tag{2.11}$$

where γ_{LG}, γ_{SG}, and γ_{SL} are the surface tension terms for the liquid-gas, solid-gas, and solid-liquid interfaces. θ is Young's contact angle given by Young's equation: $\gamma_{SL} - \gamma_S G = \gamma_L G cos\theta$. A_{LG} is the liquid-gas interface surface area, A_{SL} is the liquid-solid interface surface area, and A_{LG} is the lost solid-gas interface surface area as the liquid wets the channel. E_m is the free energy of the region of the meniscus from the bottom to the top of the channel (does not account for top surface curvature and is assumed as constant with respect to x, since the meniscus shape is unchanging during flow past the channel inlet if walls are uniform.) From this relation, we can then derive the capillary driving force F_γ as being the negative rate of change in free energy with respect to x assuming an isothermal system:

$$F_\gamma = -\frac{dG}{dx} \tag{2.12}$$

For a rectangular channel with width W and depth D and aspect ratio $p = W/D$, the interface areas are $A_{SL} = (2+p)Dx$ and $A_{LG} = Dpx$. This leads to a capillary driving force of:

$$F_\gamma = -\frac{dG}{dx} = [2cos\theta - (1 - cos\theta)p]D\gamma_l \tag{2.13}$$

This driving force is only half of the dynamics equation, the other half is the viscous drag force F_μ along the solid walls of the rectangular open channel. End effects at the channel inlet and at the filament meniscus region are neglected for this as well as assuming that at a low Reynolds number, laminar flow for a Newtonian fluid, the quasi-steady-state Poiseuille type flow $\vec{u} = (v(y, z), 0, 0)$ induced by a pressure gradient $\frac{\Delta P}{x} = [F_\gamma/(area)]/x$ describes the progression of the liquid through the channel. Therefore, this flow would obey the Stokes equations:

$$\nabla^2 v = -\frac{1}{\mu}\frac{\Delta P}{x} \tag{2.14}$$

$$\nabla \cdot \vec{u} = 0 \tag{2.15}$$

The continuity equation is then satisfied by $\vec{u} = (v(y, z), 0, 0)$ and Stoke's equations can be solved for a given x value. The boundary condition of the flow field $\vec{u}$ is no-slip at the solid walls and full-slip at the liquid-ambient interface located at $z = D$. Thus, the viscous friction force term can then be written in a form like that of a closed cylindrical capillary:

$$F_\mu = 8\pi\mu\alpha(p)x\frac{dx}{dt} \tag{2.16}$$

with dx/dt being the cross-sectional averaged velocity of the moving liquid in the channel and $\alpha(p)$ being a geometrical factor:

$$\alpha(p) = \frac{1}{8\pi}\frac{p^2}{g(p)} \tag{2.17}$$

and

$$g(p) = \int_{-p/2}^{p/2} dy' \int_0^1 dz' \frac{v(y', z')}{v_0} \tag{2.18}$$

$$y' = y/D \tag{2.19}$$

$$z' = z/D \tag{2.20}$$

with

$$v_0 = \frac{1}{\mu}\frac{\Delta P}{x}D^2 \tag{2.21}$$

The cross-sectional average term requires the flow field be explicitly calculated, which requires that Stoke's equations are solved subject to correct boundary conditions. [26] discusses the cases of "no-slip and full-slip boundary conditions at the top liquid-air interface, respectively, because for any partial slip boundary condition the result will be bounded by these two," which stands to reason. For the case of a no-slip boundary condition at both the solid-liquid and liquid-ambient interfaces, the solution is then identical to that of flow in closed rectangular channels and there is some finite contact angle of the liquid on all surfaces below 180 degrees. For the case of a full-slip boundary condition at the liquid-air interface, the solution of Stoke's equations is directly taken from the result for Poiseuille flow with a no-slip boundary condition in a rectangular closed channel, stating that the mid-plane in the channel is subject to zero tangential shear stress (full-slip). This means that the depth of the channel, D, can be replaced by $2D$ in formulas corresponding to the closed microchannel:

$$v(y', z') = \frac{\Delta P}{\mu L}\frac{4D^2}{\pi^3}\sum_{n\geq 0, odds}^{\infty}\frac{1}{n^3}[1 - \frac{cosh(n\pi y')}{cosh(n\pi p/2)}]sin(n\pi z'), \text{ [No-slip BC]} \tag{2.22a}$$

$$v(y', z') = \frac{\Delta P}{\mu L}\frac{16D^2}{\pi^3}\sum_{n\geq 0, odds}^{\infty}\frac{1}{n^3}[1 - \frac{cosh(n\pi y'/2)}{cosh(n\pi p/4)}]sin((n\pi z')/2), \text{ [Full-slip BC]} \tag{2.22b}$$

Combining the preceding equations to compute the drag force term F_μ and equating it to the capillary force term F_γ and integrating the resulting differential equation

to then depend on a linearly-dependent distance-time relation for the progression of the liquid into the open channel gives:

$$x^2 = k * t \tag{2.23}$$

where k is refered to as a "mobility parameter", equal to:

$$k = \frac{2\gamma D}{\mu}\frac{[2cos\theta - (1 - cos\theta)p]}{p^2}g(p) \tag{2.24}$$

and $g(p)$ is a boundary condition dependent term:

$$g(p) = \frac{16}{\pi^5}\sum_{n\geq 0,odds}^{\infty}\frac{1}{n^5}[\frac{n\pi}{2}p - tanh(\frac{n\pi}{2}p)], \text{[No-slip]} \tag{2.25a}$$

$$g(p) = \frac{128}{\pi^5}\sum_{n\geq 0,odds}^{\infty}\frac{1}{n^5}[\frac{n\pi}{4}p - tanh(\frac{n\pi}{4}p)], \text{[Full-slip]} \tag{2.25b}$$

giving a complete analytical solution to meniscus front location versus time in a open rectangular microchannel for a Newtonian fluid experiencing laminar flow. This model does have some known shortcomings, although not heavily impacting liquids with contact angles above 45 degrees when Concuss-Finn filaments are not present. This model assumes the liquid fully fills the channels as it progresses down the channel. The concave profile of the meniscus means that only a portion of the channel is filled with the liquid in the advancing liquid region. In this concave meniscus region, the velocity gradient is higher compared to the upstream areas of the channel where the channel is completely filled with liquid. As a result, the shear stress drag is much higher at the partially filled portion of the channel, reducing the flowrate compared to what the analytical model predicts. [28] The MLW model also does not consider changes in dynamic contact angle and assumes a constant value for the contact angle. According to another paper on modeling these dynamics, this assumption does not seem to have a significant effect on the capillary flow and the meniscus location. [31] Despite these assumptions, this MLW model has shown correlation with experimental devices and will serve as the basis for studying open microchannel flow dynamics in

this thesis.

All this is to summarize, open microfluidics and more specifically, open microchannel flow dynamics have held many researchers' interest over the years and the knowledge gained from them is directly applicable to the research of this thesis on an electrowetting flow controller.

Electrowetting in Open Microchannels

There are some key questions to be addressed about electrowetting in an open microchannel flow regulator. Namely, how do material choices and channel cross-section geometries coincide with applied voltage to generate a desired flow condition, can reversible electrowetting be achieved with such a geometry, and if so, is there any hysteresis to be expected. An additional point to note, not seen often in other literature, is the effects of utilizing ionic liquids, which tend to have higher dynamic viscosity and lower surface tension than water, in open microchannels. Luckily, there exists some experimental research into reversible electrowetting flows in a handful of open microchannel devices. Namely square, rectangular, and triangular channel cross-sections utilizing OTS (octadecyltrichlorosilane) monolayers for hydrophobic dielectric layers. [30], [32], [33] In these three papers, this research group looks into the varying liquid morphologies that can exist in such open microgrooves under varying wetting conditions. They found that for certain aspect ratios of rectangular (including square) and triangular groove geometries, electrowetting could force a water-sodium chloride-glycerin solution to flow through an otherwise hydrophobic channel. When the voltage is removed, the liquid recedes back to its reservoir. This group did not consider electrowetting utilizing DC voltage sources, nor did the end of the channel have a porous material as a boundary condition, so that is two distinct differences to this thesis research, as well as not being in a vacuum environment. The authors also derive a driving force, liquid velocity, and meniscus location set of equations from excess surface energies that follow the MLW model mentioned earlier. Further detail is available on the derivations in these papers.

2.0.5 The Electrowetting Flow Controller

To date, there is considerable research in the domains of spontaneous capillary flow in open microfluidics as well as extensive work on electrowetting and its applications within microfluidics. There is work on electrowetting to force capillary wetting in open microchannels using glycerin/sodium chloride/water mixtures and showing the receding motion of a the free advancing meniscus once voltage is removed (although in the case of this research, no free advancing meniscus is available). [30], [32], [33]. However, the electrowetting flow controller differs quite a bit. Namely, in the use of more viscous ionic liquids within open microchannels that are sufficiently rounded along edges to prevent meniscus pinning during operation. It is hypothesized that the only viable way to enact a pressure change in a liquid filament within an open microchannel that exhibits a change in contact angle from below 90 degrees to above 90 degrees, is to ensure that the meniscus morphology is free to move about and change without being limited by pinning surfaces. Additionally, there is a systems integration problem component too. The problem where the device is part of a thruster system where a porous electrospray emitter, once firing, changes the pressure gradient across the channel from a neutral one to a slightly negative one. The transients, boundary condition effects, and contact angle hysteresis remain unknowns in a DC operation domain.

The preliminary conceptual operation of such a device is shown in Figure 2-7. The open channels (in this case rectangular) are supplied a liquid either from capillaries underneath the channels or a reservoir at one end of the channels. Once voltage is applied to the electrowetting device, the contact angle should decrease, allowing for spontaneous capillary flow to drive the liquid down the length of the channel with a slightly negative pressure gradient with respect to the neutral reservoir. Once the voltage is removed, the contact angle should increase given the hydrophobic coating on the channel walls. When this occurs, it is hypothesized that the liquid will then experience a positive pressure, favoring motion towards a lower relative pressure reservoir in the opposite direction. In the case where a liquid filament is formed in

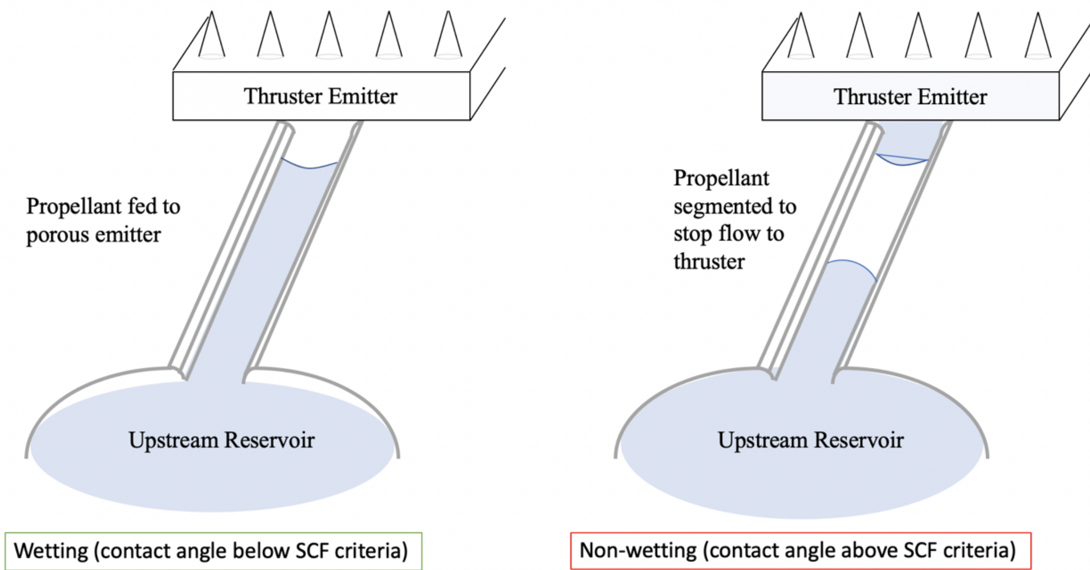

Figure 2-7: Concept for open channel electrowetting flow regulator. Left: voltage applied, contact angle allows channel to wet, feeding thruster emitter. Right: voltage removed, contact angle forces liquid to segment, de-wetting thruster emitter.

the open channel between the upstream reservoir and downstream emitter, it is hypothesized that this expected change in pressure within the channel may be sufficient to deplete the liquid within the channel and force the filament to segment between the reservoir and emitter, preventing any more propellant from reaching the thruster until desired. So long as the contact angle can fall above the generalized Cassie angle wetting threshold of 90 degrees, a positive pressure should serve to eventually deplete the hydrophobic region of the wetted channel. This would allow for a solid-state on-off flow control mechanism to act as propellant management for electrospray thrusters.

It is worth re-stating, however, that many microfluidic and non-microfluidic flow management mechanisms exist that could achieve flow control. That being said, Figure 2-8 shows a box diagram that highlights why electrowetting in open microfluidics is the ideal candidate for the use-case in electrospray thruster propellant management.

Fluid System	Scalable?	Controllable?	Compatible with Electrospray?
Pressure system	No	Yes, with hardware	Yes
Closed capillary	Yes	Not without pressure control	Yes
Electroosmotic/electrophoreses	Yes	Yes	Potential for IL electrochemistry to occur at electrodes
Droplet	Yes	Yes	Yes, but no continuous circuit can be formed across liquid
Electrowetting/Open Microfluidic	Yes	Yes, free surface is unconstrained	Yes, no potential for electrochemistry

Figure 2-8: Box diagram highlighting the shortcomings of other fluid management mechanisms in the scope of electrospray thruster propellant requirements.

2.0.6 Materials

In the past, porous glass with various frit size (microparticles comprising the bulk material) was used as an emitter material. These materials allowed a good flow rate of liquid through the pores, but unfortunately were not without their downsides. The major issue was the polydispersity of the powder and the resulting inhomogeneity of the resulting sintered material. During laser ablation of the tip arrays, there tended to be a great deal of debris and "stray tips", small peaks that were not part of the main pattern. This presented a twofold problem. First, any stray tip or piece of debris could potentially produce an emission site, which would be emitting ions directly into the extractor, damaging it or, worse, forming a liquid bridge that shorts the thruster circuit. Secondly, the increased topographical roughness of the emitter caused by the stray tips means that there were more sites that menisci can form. Like menisci (i.e. both concave upwards, in this case) can interact and climb; if that happens on the emitter chip surface, the chip could flood with ionic liquid and vastly increase the risk of shorting the emitter to the extractor. Fused silica chips with pores around 100 nm showed excellent uniformity and tip geometry compared to this material, but the pore size actually restricted flow rate and current emission. Ideally, pore sizes between 500 nanometers and 1 micron are desirable for tip geometry and flow impedance [1]. The

trend was clear, more uniformity of the material provided better tip geometries and uniform flow through the chip as a whole. Therefore, a monodisperse porous material would be ideal to address the issues seen in current porous materials used in ion electrospray thrusters.

While spin coating methods have shown to be effective in creating nearly perfect crystal formations of monodisperse nanospheres [34], to make chips thick enough for use in laser ablating the conical structures needed for ion electrospray thrusters, thousands of layers would need to be spun, making it far too inefficient a method. Similar results from self-assembly techniques which rely on capillary forces to organize colloids have the same shortcoming for the electrospray application [35].

Prior research in the Space Propulsion Lab outlined in both [2] and [1] showed that casting solutions of silica nanospheres prior to sintering provided very uniform, monodisperse porous chips that were less complex than other methods such as hydraulic pressing or freeze-casting. In the scope of this work, casting suspensions of UV-curable resin and silica nanospheres prior to curing and sintering proved to have the best batch to batch reproduceability. The procedure for forming these chips is described in detail in [2] and heavily borrows from the success in [36]. The simplified summary is: mix silica nanospheres with a surfactant, add them to a commercially available UV-curable resin, cast the solution into PDMS molds, UV cure, de-mold, and sinter to achieve the desired porosity.

2.0.7 Summary of Research Knowledge Gap and Contributions

To summarize, there exists a research gap in two areas relating to this thesis. First, between a functional and fully characterized electrowetting open microfluidic flow controller and the state of the art. Second, a lack of monodisperse porous materials for use in electrospray emitter tip arrays.

Microfluidic devices that accomplish similar fluid control do exist. However, in aerospace applications, they require additional pressurized systems that take up too

much volume and mass for small satellite applications. For most ground-based microfluid control, these requirements are not so strict. Droplet microfluidic controllers are also well studied, but can only provide a discrete flow rate via moving droplets and a set rate. Open microfluidics are also widely used, but the need for strict fluid flow control and reversibility are not common in the applications where they are presently utilized, namely diagnostics and chemical mixing and separation. Additionally, square channel geometries have demonstrated liquid pinning at sharp interfaces that impede the desired reversibility outlined in this research. There is also not much demand for propellant management that has such low mass flow rates as seen in electrospray thrusters (on the order of micrograms per second). It is the author's opinion that as satellites trend smaller and electrospray thrusters become more widely applied, propellant management on a chip will be required. Areas such as reverse electrowetting and open microchannel capillary flow modeling are well studied, but provide little insight into the more complex geometries at play in this open microfluidic research. A better understanding numerically and analytically of contact angle hysteresis in reversible electrowetting, contact angle saturation, and liquid-surface interactions in the operational transients of a flow regulator are required. Once this gap is narrowed, experimental devices will need to be designed, fabricated, and tested to compare and hopefully verify the modeling results.

Lastly, although monolithic monodisperse porous materials exist, the common means to manufacture them are typically quite labor intensive or prohibitively expensive for the academic lab environment. As shown in previous research on casting UV curable resin solutions packed with Al2O3, a repeatable process that can be done with a kiln and common lab equipment creates usable ceramic components [36]. By exploring this process for silica nanospheres, a monodisperse emitter material may be achieved for a fraction of the cost of polydisperse emitter materials currently used in electrospray thrusters. This thesis research seeks to further evolve work within the Space Propulsion Lab on creating a silica monodisperse emitter material that would mitigate the previously discussed issues that are present in polydisperse emitter materials. To summarize, the three thesis contributions in this work are:

1. Analyze (both numnerical and analytical) of the expected dynamics of wetting various aspect ratio open microchannels via electrowetting. Determine the expected pressure changes via electrowetting actuation within a hydrophobic open microchannel given contact angle ranges.

2. Design and fabricate an electrowetting flow controller based on an open microchannel architecture. Test these devices and compare their wetting behavior under electrowetting as well as the liquid segmentation phenomenon.

3. Develop and produce a porous monodisperse sintered nanoparticle emitter material for use in electrospray thrusters. Characterize their hardness, laser ablation response, and thruster performance.

Chapter 3

Electrospray Thruster Propellant Management

Given the prior review of literature pertaining to electrospray thrusters, microfluidics, electrowetting, and material science, this chapter discusses the current method of propellant management in electrospray thrusters in greater depth, highlighting the design parameters an active flow control device would need to operate within.

3.1 Capillary Flows in Electrospray Thrusters

The entirety of the electrospray thruster is essentially a microfluidic system. That is, it meets the criteria that all liquid flows are under capillary forces alone between the propellant reservoir and the porous emitter chip of the thruster. The electrospray thrusters are composed of several distinct components crucial to this fluid flow path: a porous PTFE neutral pressure propellant reservoir, a distal porous electrode (which mitigates the occurrence of propellant degradation due to electrochemistry) [5], a porous wicking filter paper, an electrowetting capillary valve, and a a porous thruster emitter.

The fluid system (shown in Figure 3-1) in an electrospray thruster sees multiple boundary condition changes from launch to on-orbit operation. First, the system is completely unsaturated, meaning the propellant remains in the reservoir and is kept

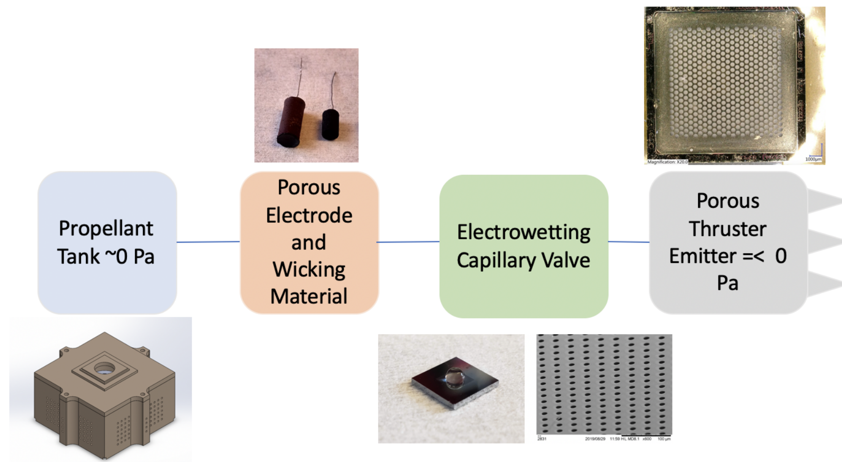

Figure 3-1: A diagram of the fluid path for electrospray thrusters from the propellant reservoir up to the porous thruster emitter.

there by the use of the single-use electrowetting capillary valve during its time on the launchpad until it is in orbit. Once on orbit, the electrowetting capillary valve is activated, wetting the multiple capillaries and carrying the propellant from the still neutral pressure reservoir up to the porous thruster emitter. Once the emitter is fully saturated with ionic liquid, the thruster is ready to fire. When not firing, the system is either at a neutral pressure at both ends or experiences a slightly negative pressure around the emitter tips if flooding begins to occur. When firing, the thruster end experiences a slightly negative pressure at the ions are extracted from the propellant focused at the emitter tips. Thus, the current system is well-suited for an electrospray thruster that has no risk of emitter flooding. However, since the current system may have inadvertent menisci form between emitter tips, there is a need for an additional component or system to segment the liquid supply to the emitter and prevent the menisci between the emitter tips from forming or propagating up to the extractor grid and shorting the thruster. This new flow controller must be able to segment the liquid in this system with an upstream boundary condition of a neutral pressure propellant reservoir and downstream condition of a neutral pressure (or slightly negative pressure) saturated thruster emitter.

As mentioned earlier, the flooded emitter problem is reliant on two variables on the emitter side, first is the tip radius and second is the liquid contact angle with the tips.

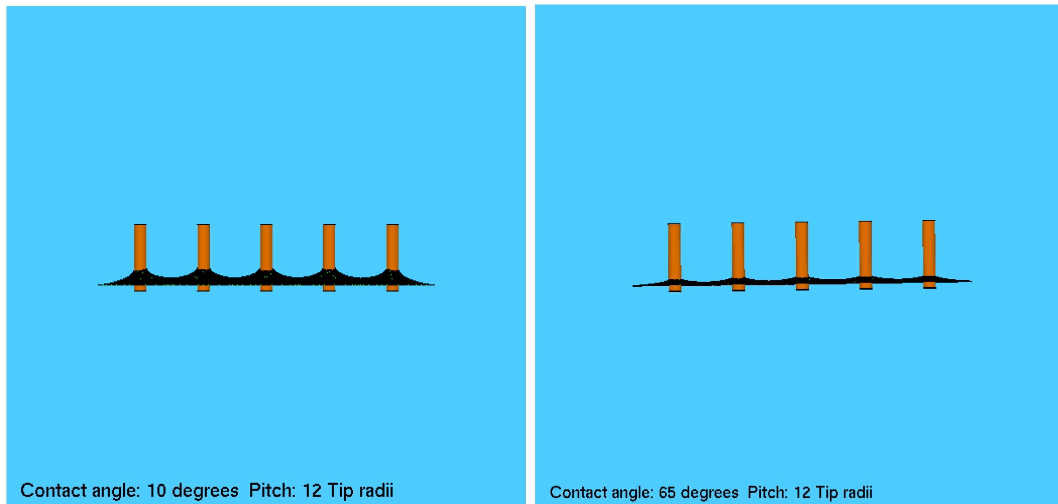

Figure 3-2: Surface Evolver simulation of a hexagonally packed group of cylinders experiencing "emitter flooding." Left: Contact angle of 10 degrees allows capillary flow up cylinders. Right: Contact angle of 65 degrees prevents capillary flow up cylinder.

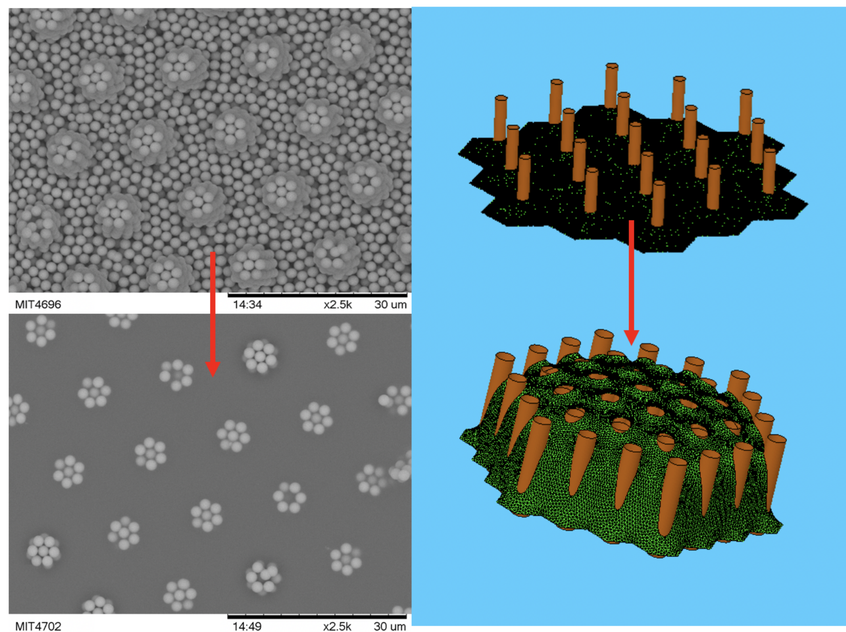

Figure 3-3: Left: top-down view of actual emitter tips flooding with propellant. Right: Surface Evolver simulation of propellant flooding effect between emitter tips modelled as cylinder.

As shown in Figure 3-2, by decreasing the contact angle, the liquid wants to bridge the gaps of the emitter tips and form a negative pressure meniscus that propagates up the tips. With sufficiently high contact angle and/or sufficiently high tip spacing,

these menisci cannot form. However, ionic liquids tend to have low contact angles on the porous emitter materials, and to enable a competitive thrust density to other forms of electric propulsion thrusters, 480 tips per square centimeter is necessary. So the only passive solutions are to increase contact angle on the emitter tips and/or make the tips extremely narrow as to increase the distance between the tip surfaces that can be wetted. Shown in Figure 3-3 is a tip spacing equal to 5 times the tip radius and a contact angle of 65 degrees. Given enough time and an continuous flow of propellant, this emitter arrangement still floods. This is an outcome that seen in thruster operating in lab conditions as well even when oriented in a manner that provides a gravitational assist opposite the direction of meniscus travel up the tips. An emitter that experienced flooding in one region is shown in Figure 3-4.

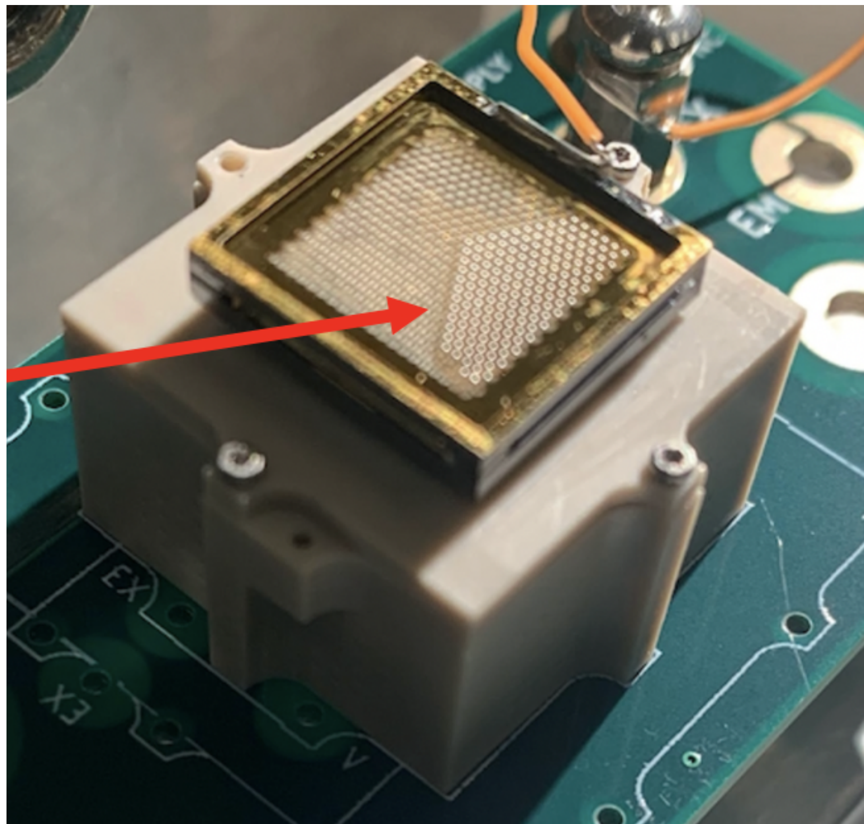

Figure 3-4: A "flooded" thruster emitter. Note the meniscus formations between tips and the extractor as highlighted by the red arrow.

All of this is to simply state, the current arrangement of emitter tips and a single-use electrowetting valve still allows for emitter flooding even when the thruster is not

firing and at a neutral pressure. If the "infinite" reservoir upstream of the emitter tips could be severed at will, the propagation of this flooding phenomenon up the tips and to the extractor grid could be prevented. Thus the design of an electrowetting flow controller to be integrated upstream of the emitter is needed.

THIS PAGE INTENTIONALLY LEFT BLANK

Chapter 4

Design of an Electrowetting Flow Controller

As was laid out in the previous chapter on current propellant management and flow path in electrospray thrusters, this chapter focuses on the design of an electrowetting flow controller that can achieve repeatable on-off flow control between the propellant reservoir and the thruster's porous emitter.

4.1 Performance Requirements for an Electrowetting Flow Controller

Throughout the course of firing many ion electrospray thrusters with both sintered silica emitters and a commercially available porous glass emitter, the typical mass flow rate seen for a thruster during operation is on the order of about 0.5 μg/s in the ionic mode, measured under lab conditions in recent tests. For a thruster to fire without a "choked flow" condition, an upstream flow controller must be able to provide a minimum of 0.5 μg/s when in the "open" state. This is the first performance requirement of an active flow controlling device.

Pressure at the emitter array in ion electrospray thrusters is either neutral (assuming no flooding onset) when not firing or negative with respect to the neutral

reservoir during ion emission. The magnitude of this pressure is governed solely by the extraction voltage in passive devices with no active flow control. Therefore, so long as the mass flow rate requirement is satisfied, and the ability to slow this flow (decrease the magnitude of the emitter site pressure) or stop it completely is attained, an upstream flow controller pressure requirement is satisfied.

A secondary performance requirement is the ability to both allow flow and stop flow to the thruster cyclically, unlike the prior iteration of the closed capillary electrowetting valve which only offers a single-use flow control. This means possible failure modes such and liquid pinning and dielectric breakdown must be avoided all while maintaining a free surface to be modified via electrowetting. If the liquid were allowed to pin along the channel edges, once in contact with a saturated liquid end condition at the other end of the channel, the free surface would longer be able to move freely in response to electrowetting contact angle changes.

Finally, a flow controller device must be able to operate within the supplied voltage range of the propulsion unit's power processing board. This voltage limit is set at 1000V. All of these performance requirements point to a device that must be able to alter the pressure of a liquid between the neutral pressure reservoir and the either neutral or slightly negative pressure emitter array. In order to achieve this, an open microchannel design is proposed to take full advantage of the free surface interface between the liquid and the environment in tandem with electrowetting to alter the interfacial wetting between the liquid and the device.

4.2 Open Microchannels

As was discussed in the preceding literature review of open microchannel research, the fluid dynamics of open microchannel flows is a well-studied area. Expected flow velocities, pressures, and effects of contact angle, surface tension, and viscosity changes all have analytical solutions to guide the design of the microchannel to meet given requirements. From a microfluidics standpoint, there are many cross-sections that are produceable and could meet the aforementioned flow rate requirements, however,

rectangular channels are some of the simplest in terms of manufacturing scalability. Given the nature of operating in a zero-gravity space environment, this device is also not bounded to the same limiting scales of capillary-dominated flow as here on Earth. Some assumptions are made in the analysis and design of the microchannel in this work, namely: the fluid in the channels has a continuous state of matter and can be described using Navier-Stokes equations obtained from the conservation of mass, momentum, and energy [37]. The device and liquid are assumed to be isothermal and consist of one incompressible ionic liquid, which is represented as a single liquid phase (given there is no gaseous atmosphere in vacuum.) There is presumed to be enough rounding of sharp interfaces (namely the edges along a rectangular channel) to avoid the meniscus pinning during electrowetting, a presumption that is key to the functionality of the electrowetting flow controller. If the liquid were to pin along the edges of the channel walls and then reach the saturated emitter at the end of the channel, a liquid bridge would be formed and the benefit of having a free surface would be negated by the pinned meniscus, since the contact angle at the channel corner becomes undetermined. In order for the meniscus morphology to change in the open microchannel, it must be free to move and evolve as the contact angle is changed via electrowetting.

Given the microfluidic scale of flows in these devices, the Reynolds number is low, meaning inertia can be neglected and laminar flow should be expected where viscous forces are dominant. Following a similar derivation process discussed in [28], the ratio of inertial to viscous forces is defined by the dimensionless Reynolds number:

$$R_e = \frac{\rho u L}{\mu} \tag{4.1}$$

The comparative forces of gravity and surface tension are defined by the dimensionless Bond number:

$$B_o = \frac{\Delta \rho g L^2}{\gamma} \tag{4.2}$$

where $\Delta\rho$ is the difference in the density of the two phases (if two phases are present), g is the gravitational acceleration, u is the average liquid velocity inside the microchannel, L is the characteristic length (or in the case of a fully-wetted circular cross section, L is the diameter of the tube), γ is the surface tension and μ is the dynamic viscosity. The characteristic length utilized in the dimensionless Bond and Reynolds numbers are then:

$$L = \frac{4A_c}{p_w} \tag{4.3}$$

where A_c is the cross-sectional area of the microchannel and p_w is the wetted perimeter of the channel cross-section.

Given that Bond number values are substantially less than 1 for microfluidic devices under 1 mm in characteristic length, including this work, gravitational effects are negligible and the low Reynolds number for ionic liquids at these micron scales confirm that Stokes flow can be assumed.

In similar fashion to [26] approach outlined in the literature review, the Modified Lucas Washburn (MLW) dynamics model is used for rectangular microchannels:

$$x^2 = k * t \tag{4.4}$$

where x is the distance the meniscus penetrates into the open microchannel, k is a geometry-dependant mobility parameter, and t is time. It is assumed that the flow is driven by the change in the free energy of the system as the liquid advances along the channel. This advancing flow is opposed by hydrodynamic viscous friction slowing the flow along the channel length. After the inertial phase of the flow when the liquid begins to accelerate near the channel entrance, the capillary force and viscous friction forces balance one another. This force balance is derived in [26] and shown in the literature review section. The mobility parameter k is then:

$$k = \frac{2\gamma D}{\mu} \frac{[2cos\theta - (1 - cos\theta)p]}{p^2} g(p) \tag{4.5}$$

where D is the channel depth and p is the channel aspect ratio Width/Depth.

In the mobility parameter equation, $g(p)$ is then:

$$g(p) = \frac{16}{\pi^5} \sum_{n \geq 0, odds}^{\infty} \frac{1}{n^5} [\frac{n\pi}{2} p - tanh(\frac{n\pi}{2} p)] \tag{4.6}$$

for a no-slip boundary condition and:

$$g(p) = \frac{128}{\pi^5} \sum_{n \geq 0, odds}^{\infty} \frac{1}{n^5} [\frac{n\pi}{4} p - tanh(\frac{n\pi}{4} p)] \tag{4.7}$$

for a full-slip boundary condition. It is presumed that the velocity at the walls in the channel will have some negligible velocity (no-slip), whereas the liquid-ambient interface is a full-slip boundary given there is no solid wall.

Thus for a given range of contact angles, a channel aspect ratio, liquid surface tension, and dynamic viscosity, a range of liquid meniscus front penetration velocities and flow rates can be predicted.

For experimentation verification purposes, two ionic liquids: EMI-BF4 and EMI-IM are studied along with water and a water-isopropyl alcohol mixture (ratio set by volume) to fully determine the model efficacy for a range of liquid properties.

First, a range of expected pressures vs. channel depth for fixed channel widths using the modified-Delamarche rectangular microchannel pressure is attained [38], [39], [40].

$$\Delta P = \gamma(\frac{2cos\theta}{w} + \frac{cos\theta}{h})) \tag{4.8}$$

A range of generalized Cassie contact angles between 70 degrees and 110 degrees show the effect of falling above and below the 90 degree wetting/non-wetting threshold within an open channel of varying depth. When the generalized Cassie angle is below the 90 degree threshold, a negative pressure, relative to the neutral reservoir, is formed at the meniscus front, pulling it into the channel. It is assumed that the channels are fed by an effectively infinite liquid reservoir with negligible pressure. The generalized Cassie angle is simply the fractional contribution of the channel walls and free surface

cross-sections to the contact angle of the liquid filament in the channel given by:

$$\cos(\theta_c) = \sum_{n=1}(f_n cos(\theta_n) \tag{4.9}$$

Where θ_c is the Cassie angle, f_n is the area fraction of each interface present in the flow cross-section (liquid-wall and liquid-gas in this case), and θ_n is the contact angle between each interface in the cross-section (again liquid-wall, which is variable via electrowetting, and liquid-gas, which is assumed to effectively be 180 degrees at all times.) Given that electrowetting only directly changes the contact angle of the liquid-wall interface, this range is crucial to determining an operation window of pressures that grants both flow and no-flow to the emitter. Normalized pressure contours are generated for a variety of channel widths and depths for EMI-BF4, as an example, and one is shown in Figure 4-1. From these contours, it is clear that, for example with EMI-BF4, a contact angle range of 76 degrees to 98 degrees with the walls requires a channel depth-to-width aspect ratio of at least 1.6 to ensure a Cassie angle below 90 degrees that enables wetting of the channel via a negative pressure relative to the upstream reservoir. For that same channel aspect ratio of 1.6, a Cassie angle of approximately 108 degrees is achieved when the contact angle of the liquid with the walls reaches 98 degrees, meaning a positive pressure is then formed by the meniscus, assuming it is not pinned along the wall, that should cause a capillary instability between the two relatively lower pressure end conditions of the channel leading to segmentation.

As is expected in open microchannels, small channel cross-sections produce higher pressures and lower flow velocities while larger channels produce lower pressures and larger flow velocities. These same pressure contours are generated for all liquids tested and for many channel widths to guide the sizing of the necessary channel(s) for each liquid. These additional contours are located in the appendix for reference. To attain a desired flow rate, one can either size a single larger channel or have several small channels acting in parallel. Of course, to enable spontaneous capillary flow into the channel in the first place, the minimum channel aspect ratio is still governed by the

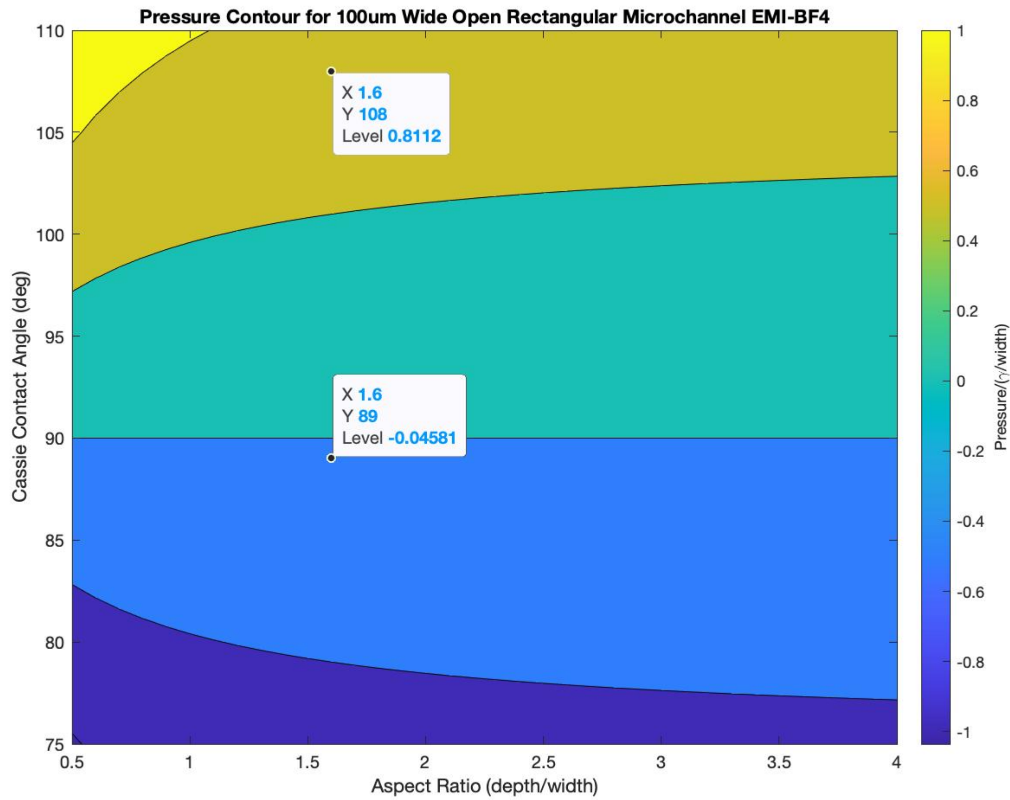

Figure 4-1: Expected normalized pressure contour for a 100 micron wide rectangular channel with varying depths using EMI-BF4. Note the highlight of the 1.6 aspect ratio point highlighting the onset of SCF for a liquid-wall contact angle of 76 degrees.

equation:

$$\frac{p_f}{p_w} < cos(\theta) \tag{4.10}$$

This means that for each liquid, contact angle range attainable via electrowetting must be determined first. Given the many hydrophobic coatings and processes available, this task will be discussed in a following chapter.

Lastly, as mentioned already, meniscus pinning is a phenomenon that is still the focus of much ongoing research. To briefly recap, a liquid meniscus often "pins" when it comes into contact with a sharp interface that it cannot traverse around due to being energetically unfavorable to traverse over a sharp edge. Once this pinning effect occurs, the contact angle becomes indeterminate, subject to change only via external

pressure change. The goal of the electrowetting flow controller device to achieve the opposite, that is, a change in pressure via changing the contact angle. Generally speaking, pinning should not occur on locally smooth and rounded surfaces where the liquid is free to change morphology, even if those surfaces are coated with a low friction hydrophobic coating. This assumption is a crucial hypothesis to the functionality of an electrowetting flow controller utilizing a rounded microchannel. This pinning effect is shown in Figure 4-2 where the liquid flowing into an open rectangular channel pins along the 90 degree wall ledge as it progresses as compared to an exaggerated rounded ledge variant with free meniscus evolution.

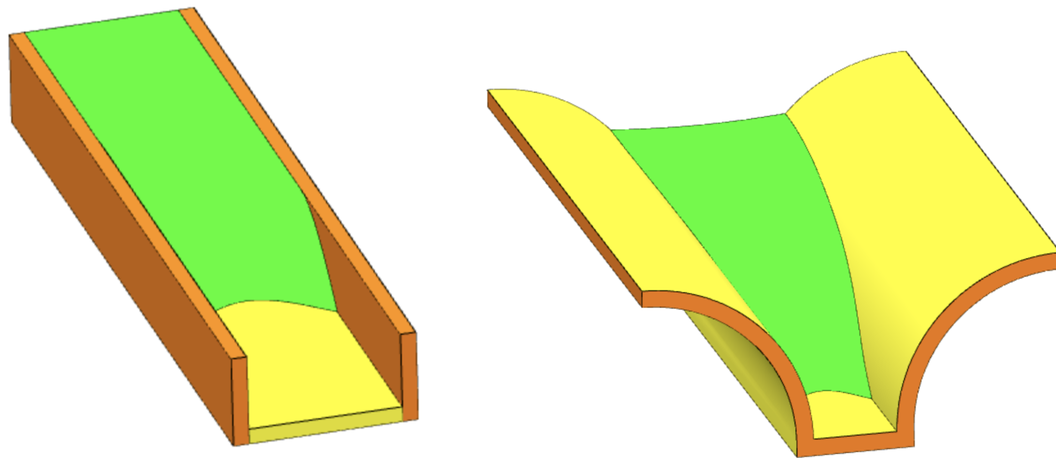

Figure 4-2: Surface Evolver simulated meniscus morphologies in open microchannels. Left:liquid pinning to the ledges of a rectangular microchannel. Right: Liquid meniscus freely terminating at its contact angle with the rounded channel wall.

In order for the electrowetting effect to enact a change in meniscus morphology in an open microchannel that has a liquid boundary condition at either end (such as in an electrospray thruster where a propellant reservoir and saturated emitter are present), the liquid must not be pinned along the channel ledge. If pinning occurs, the channel may wet, but once it reaches the saturated emitter, there will no longer be a free surface that can be manipulated via electrowetting. Therefore, any open microchannel designs must have sufficiently smooth and sufficiently rounded features to prevent this pinning from occurring.

This brings up the possibility of unorthodox "open microchannels" that could be

Table 4.1: Liquid Properties

Liquid	Surface Tension [N/m]	Dynamic Viscosity [Pa · s]	CA Range [deg]
EMI-BF4	0.054	0.037	84-103 w/o O2 plasma
			76-98 degrees w/ O2 plasma
EMI-IM	0.038	0.041	72-84
DI Water	0.072	0.001	81-115
80% DI Water/20% IPA	0.03	0.00225	75-98

formed using two cylinders, sufficiently close enough together to satisfy the general SCF wetting condition. While the focus of this research is on a device that can be implemented into the flow path of an electrospray thruster, a cylindrical device verification experiment will also be discussed.

4.3 Numerical and Analytical Performance Modeling

To analytically estimate the expected flow rate from the microchannels for each liquid, the liquid penetration vs time relation from [26] is used, referred to as the Modified Lucas Washburn or MLW model. A no-slip condition is assumed at the channel walls and a free-slip condition is assumed along the free surface of the channel. This is only an estimate given the liquid is assumed to fill the channel completely as it moves along the channel length as mentioned in the literature review section. As will be discussed in the following fabrication chapter, two channel depths are used for predicting fluid intrusion rates in open rectangular microchannels: 200 micron depth and 400 micron depth. These depths are easily attainable via the preferred silicon etching technique to be discussed later. In addition to these achievable channel depths, electrowetting contact angle values on a fluoropolymer hydrophobic layer (which will also be discussed in greater depth in the experimental results chapter) are used. These contact angles and known liquid properties are shown in the table below:

From the SCF criteria, it is determined that rectangular channel depth-to-width aspect ratios of 4.3 or 1.6 with plasma treatment for EMI-BF4, 1.15 for EMI-IM,

2.7 for DI Water, and 1.55 for a mixture of DI water and IPA are needed to attain spontaneous capillary flow. MLW predictions for the rate of liquid intrusion into open rectangular microchannels that are deep enough to cause spontaneous capillary flow are shown in Figures 4-3 and 4-4.

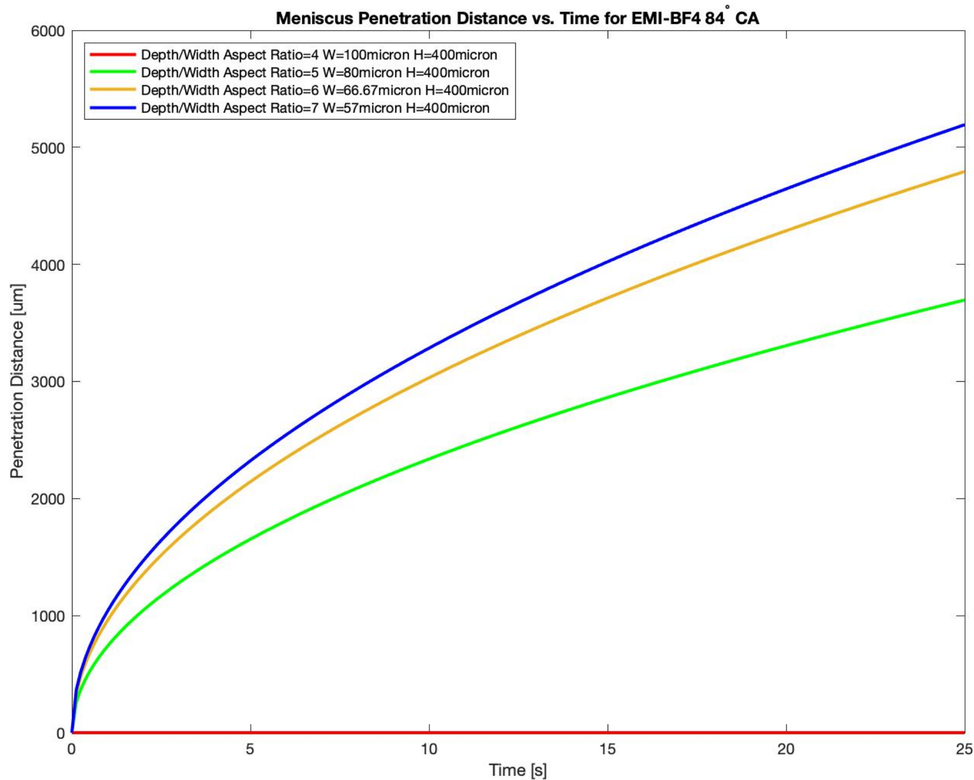

Figure 4-3: Expected liquid penetration distance vs time for EMI-BF4 in a variety of rectangular microchannels.

EMI-BF4 is a viscous ionic liquid with a contact angle range that just barely permits reliable wetting via electrowetting at 84 degrees atop spin-coated fluoropel. However, with an oxygen plasma treatment, the contact angle (and hydrophobicity) can be slightly reduced. In the case of fluoropel and and oxygen plasma treatment that will be discussed in greater detail later, the contact angle for EMI-BF4 is reduced slightly to 76 degree under the influence of electrowetting.

This means that the expected rate of intrusion of EMI-BF4 into the channel should be much slower than a less viscous and/or higher surface tension liquid such

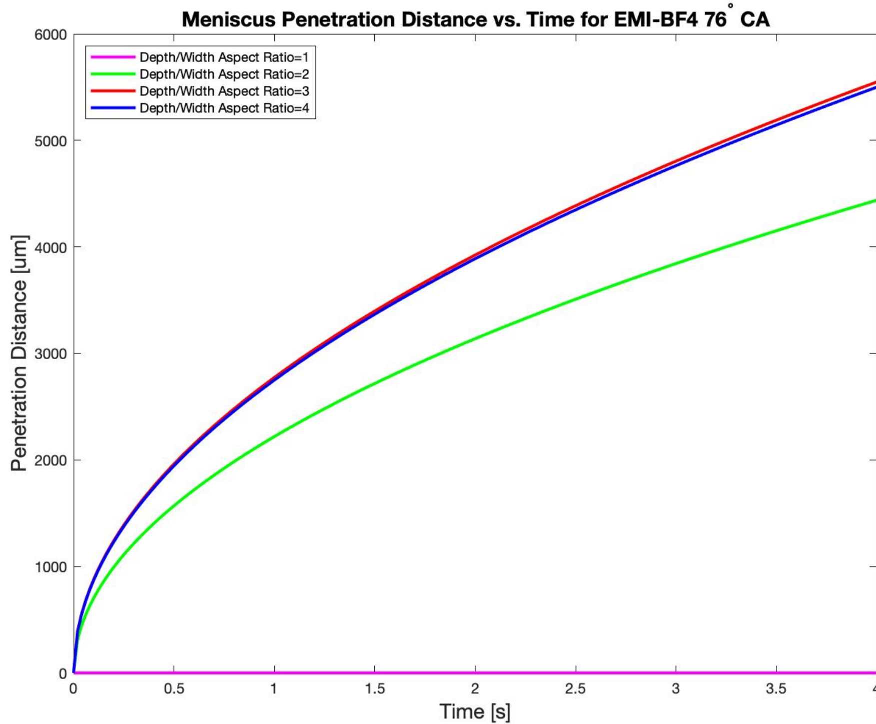

Figure 4-4: Expected liquid penetration distance vs time for EMI-BF4 in a variety of rectangular microchannels coated with an oxygen-plasma-treated spin-coated fluoropel layer. Note that with only an 8 degree decrease in contact angle, necessary aspect ratio decreases from slightly above 4 down to 2. All channel depths are fixed at 400 micron, aspect ratio is varied by channel width.

as water. Given the flow rate requirements for electrospray thrusters are on the order of micrograms per second, this should not be a major hindrance. Also noteworthy, is the fact that the larger 400 micron deep channel (with lower pressure) allows for faster liquid motion, translating to larger flow rates. This lends itself well to the hypothesis that either multiple small channels or a single large channel should be able to provide a firing thruster with sufficient propellant without impacting the overall thruster footprint.

EMI-IM is a particularly appealing propellant due to the fact that it does not absorb water from the atmosphere nearly as much as EMI-BF4 does. This means the contact angle of this liquid should be relatively stable even during storage (perhaps prior to a rocket launch.) However, the contact angle of this liquid, as will be shown in the experimental results chapter, is found to be quite narrow for every hydrophobic

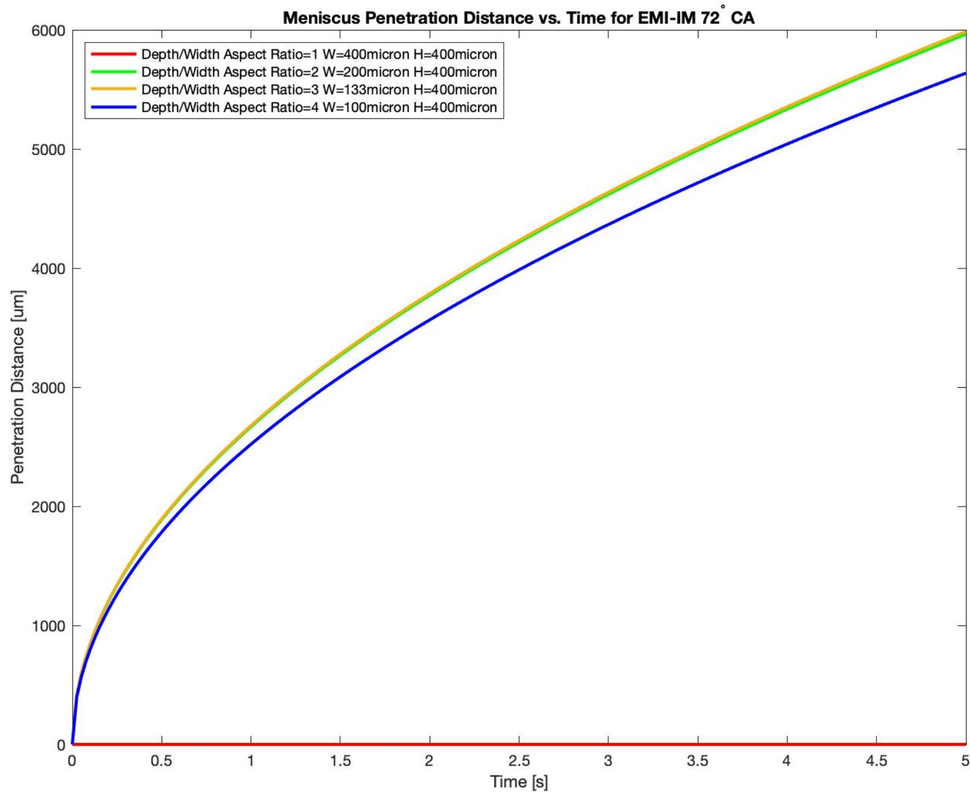

Figure 4-5: Expected liquid penetration distance vs time for EMI-IM in a variety of rectangular microchannels 400 micron deep.

coating tested. This means that without some increase to the contact angle range of the hydrophobic coating used for EMI-IM, or very precise channel geometries, EMI-IM will likely not be suitable for on-off flow control with simple, open rounded rectangular microchannels. Precision control of contact angle within single degrees is quite difficult with electrowetting on smooth surfaces, let alone inside of open channels with rougher side-walls. Nonetheless, EMI-IM channel penetration under electrowetting are estimated in the figures below:

For pure DI water, flow velocity is markedly faster than either EMI-BF4 or EMI-IM. This is reasonable given the substantially lower viscosity and higher surface tension of water compared to the ionic liquids even with a similar contact angle value.

For the mixture of IPA and water, flow velocity is slightly slower than pure water as to be expected given the higher viscosity and larger friction force along the channel,

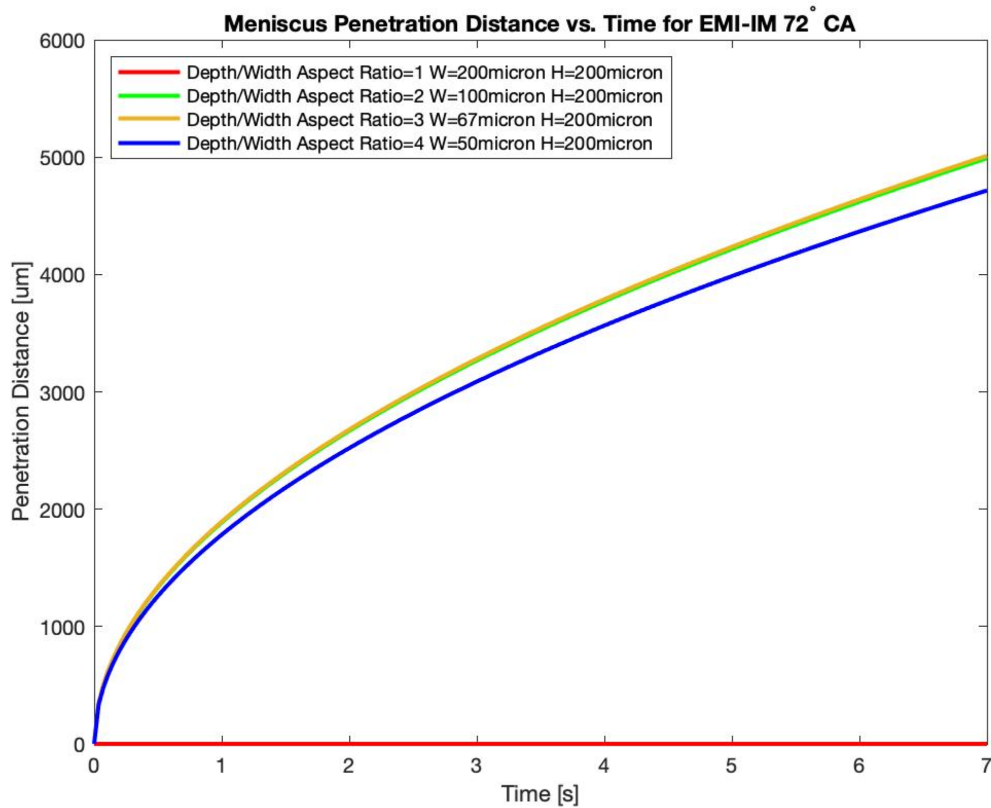

Figure 4-6: Expected liquid penetration distance vs time for EMI-IM in a variety of rectangular microchannels 200 micron deep.

despite the lower contact angle. All of this is to say, in order to tune an open channel flow to a desired flow rate for a liquid with known surface tension, dynamic viscosity, and contact angle, aspect ratio and channel length must permit spontaneous capillary flow and have just enough viscous drag to create the desired flow rate. All of these analytical predicted penetration distance vs time values will be plotted against experimental devices in the results chapter.

Flow into the channel is only half of the problem in flow control, however, once the liquid reaches the end of the channel and wets whatever porous medium is placed there, the challenge is then turning "off" the flow. By changing the contact angle via electrowetting and allowing that change to affect a change in morphology of the liquid in the channel, a change in pressure of should occur. If the central region of the channel is hydrophobic and voltage is removed restoring the initial hydrophobic

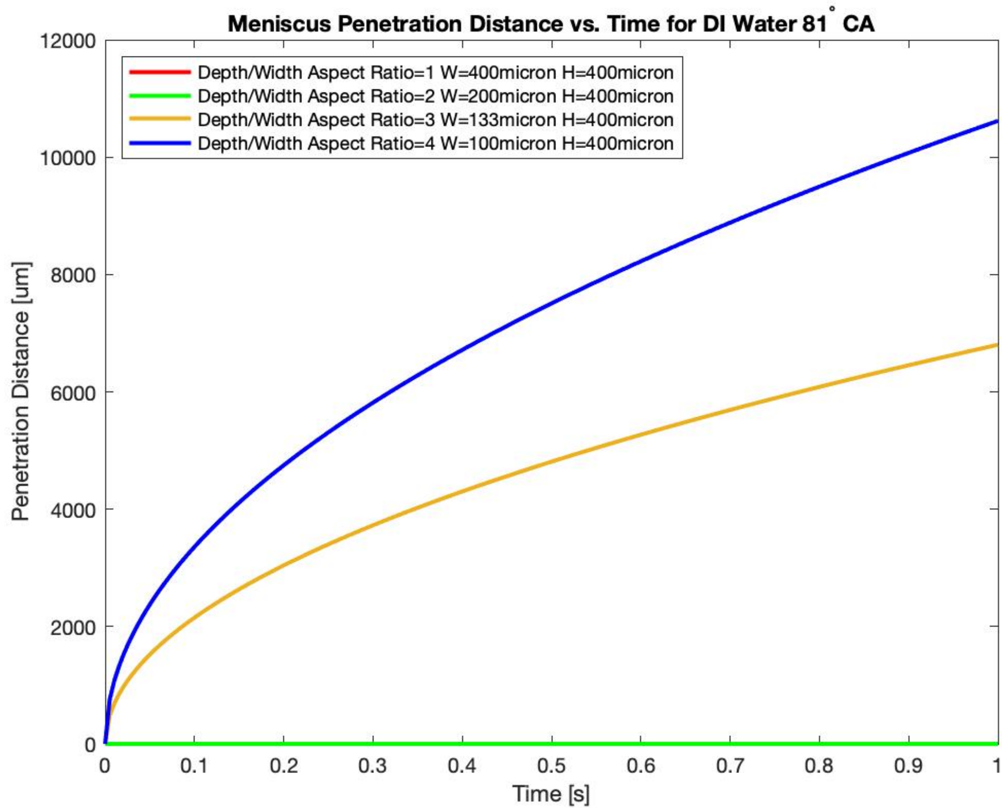

Figure 4-7: Expected liquid penetration distance vs time for DI water in a variety of rectangular microchannels 400 micron deep.

contact angle, a positive pressure region should form atop the hydrophobic region of the microchannel. This positive pressure should be sufficient to cause a capillary instability relative to the neutral or negative pressure ends of the channel that leads to depletion of liquid over the hydrophobic region and to the eventual segmentation of the liquid between the upstream liquid reservoir and downstream liquid reservoir or wetted porous media. It may be the case that even slight pressure perturbations may lead to segmentation instabilities, something that future work should take it account.

In order to analyze this assumption, a numerical volume of fluid method is used in the program FLOW-3D. First, an open rectangular microchannel 100 micron wide by 300 micron deep is set up with a an initial infinite water reservoir at the channel inlet. The FLOW-3D viscous flow and surface tension modules are used with laminar incompressible flow specified. Contact angle is set at 75 degrees with the channel

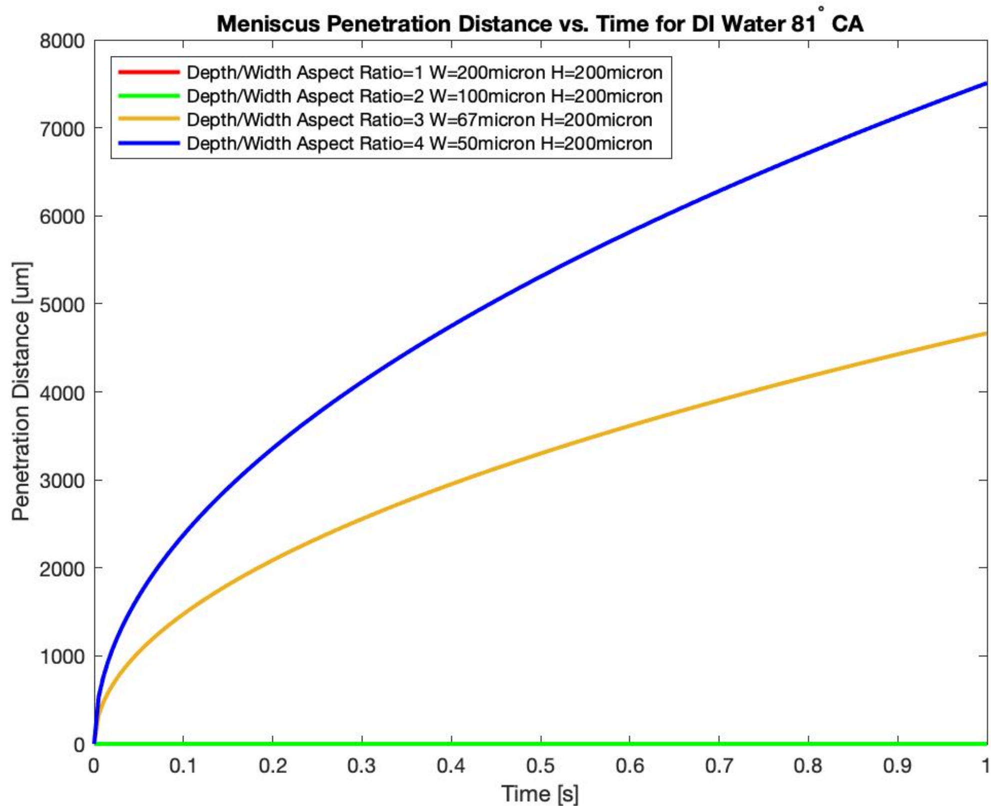

Figure 4-8: Expected liquid penetration distance vs time for DI water in a variety of rectangular microchannels 200 micron deep.

walls and sides. The upstream boundary condition is zero relative pressure with only a water phase present. The channel end condition is a neutral pressure with no liquid present. The top open surface of the channel is also a neutral pressure boundary condition. No evaporation is considered. The initial channel simulation set-up is shown in Figure 4-11.

Once the simulation is started, as expected, the liquid flows into the channel under the effects of surface tension between the liquid and the walls. The location of the liquid phase boundary front along the x-axis of the channel is logged vs time. This data is then plotted against the MLW analytical prediction for a similar 100 micron by 300 micron open rectangular microchannel and shown in Figure 4-12. The initial comparison results between the numerical and analytical values for open microchannel flow dynamics are close in agreement. The numerical simulation underpredicts

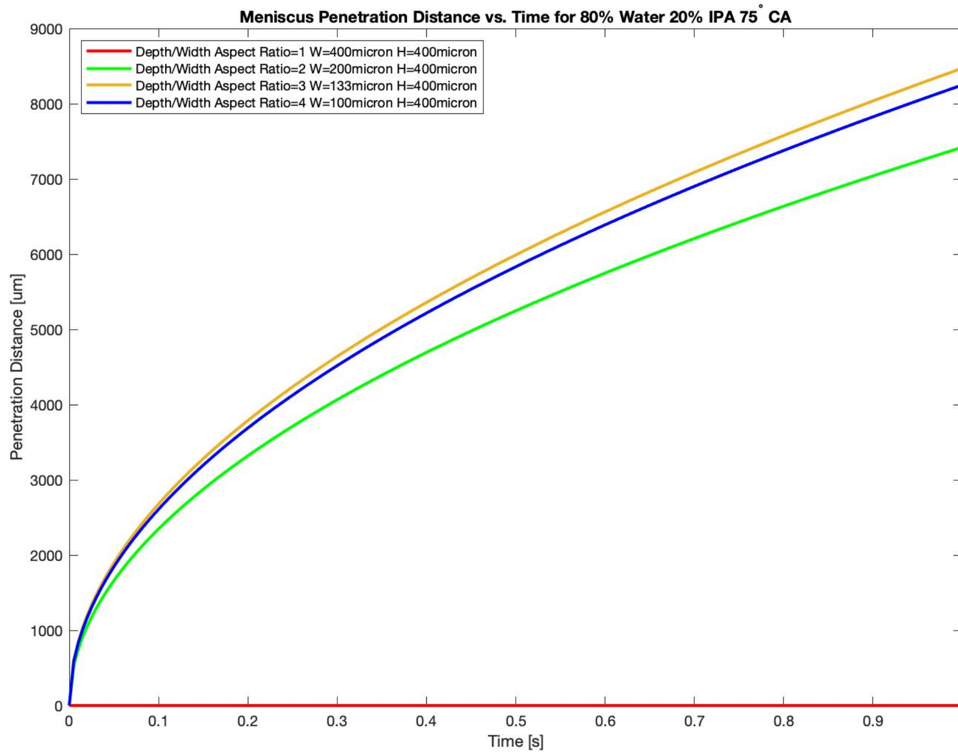

Figure 4-9: Expected liquid penetration distance vs time for 80% water 20% IPA by volume in a variety of rectangular microchannels 400 micron deep.

slightly, likely due to the fact that the liquid phase boundary is not perfectly flat, but rather concave. Only a partial volume of the channel is filled with the liquid in the region where the liquid is progressing. Here, the velocity gradient is higher compared to the upstream volume of the channel where the liquid has already filled. As a result, the shear stress induced drag would be higher at the partially filled portion of the channel, reducing the wetting rate of the channel compared to what the analytical MLW model predicts. This is also in agreement with the results found in [28]. Additional deviation may be explained by the resolution of the mesh used. No adaptive mesh features were utilized in these simulations, so the phase boundary resolution is only as good as the rest of the mesh, in this case each mesh unit was 1 cubic micron.

This comparison was primarily to validate the predictive capability of FLOW-3D for use in simulating the desired liquid segmentation in an open electrowetting microchannel. The next simulation changes the initial and boundary conditions within

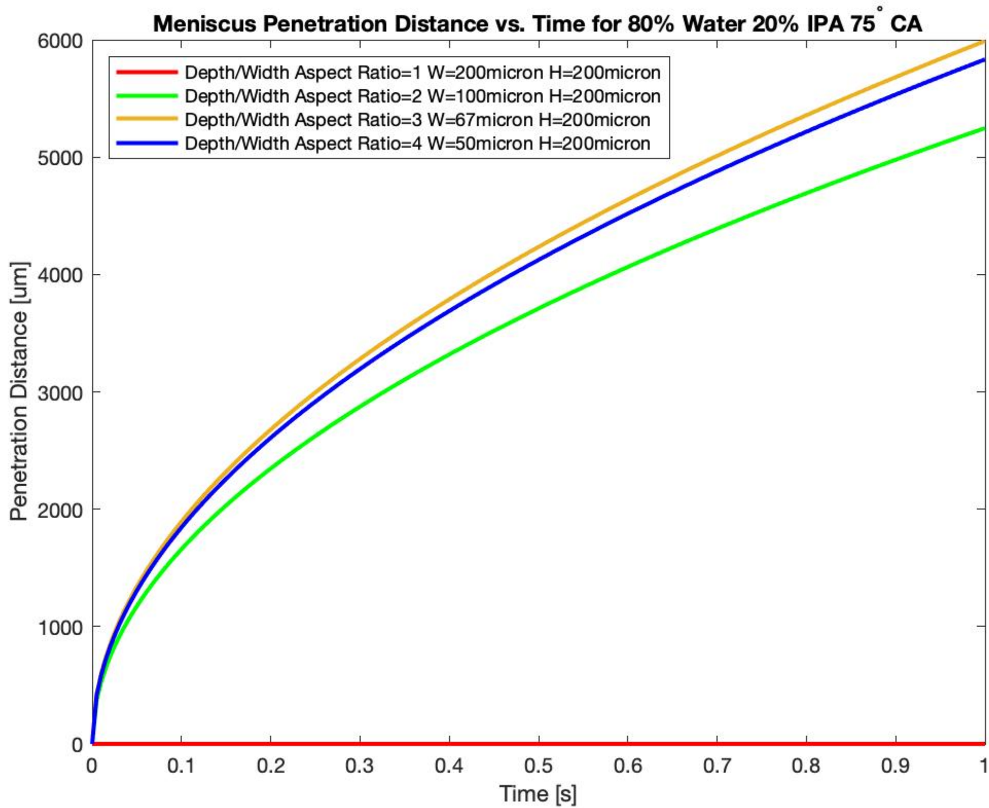

Figure 4-10: Expected liquid penetration distance vs time for 80% water 20% IPA by volume in a variety of rectangular microchannels 200 micron deep.

the same channel geometry. Initially, the channel is filled with liquid (after voltage is applied and the channel is fully wetted) and the upstream and downstream channel openings have a fluid fraction of pure water to simulate the liquid reservoir as well as a saturated downstream reservoir. The contact angle on the walls and bottom of the channel is changed to 100 degrees in this case to simulate the restoration of the hydrophobic nature of the coating needed for electrowetting. The contact line is free to move about the rounded ledge of the channel. The results of this simulation are shown in Figure 4-13 Once the hydrophobic contact angle is restored to the channel walls, the liquid depletes in the direction of the lower relative pressure regions until a thin liquid film left at the base of the channel eventually breaks, leaving the hydrophobic region of the channel dry. The pressure of the liquid in this now hydrophobic region is on the order of 400 Pascals which is quite close the predicted Laplace pressure

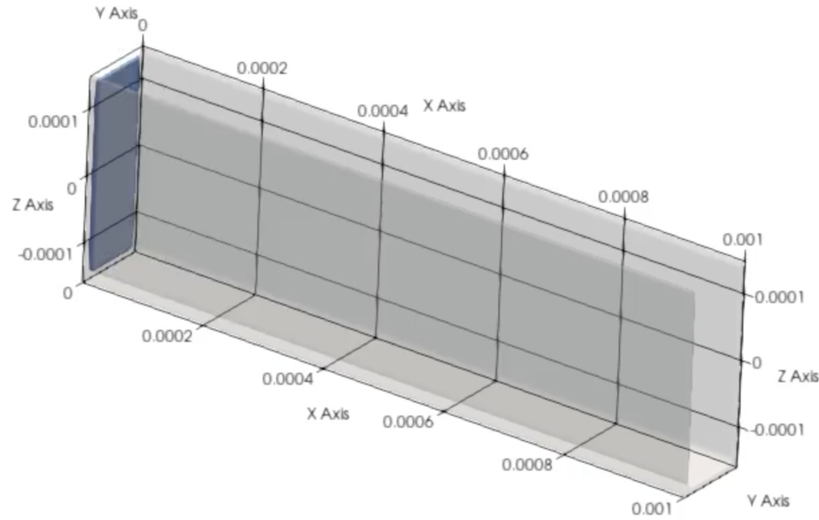

Figure 4-11: A rounded open microchannel 100 micron wide by 300 micron deep with an infinite upstream reservoir of water at zero pressure. This numerical simulation is run as a comparison to the MLW liquid filament propagation length vs. time.

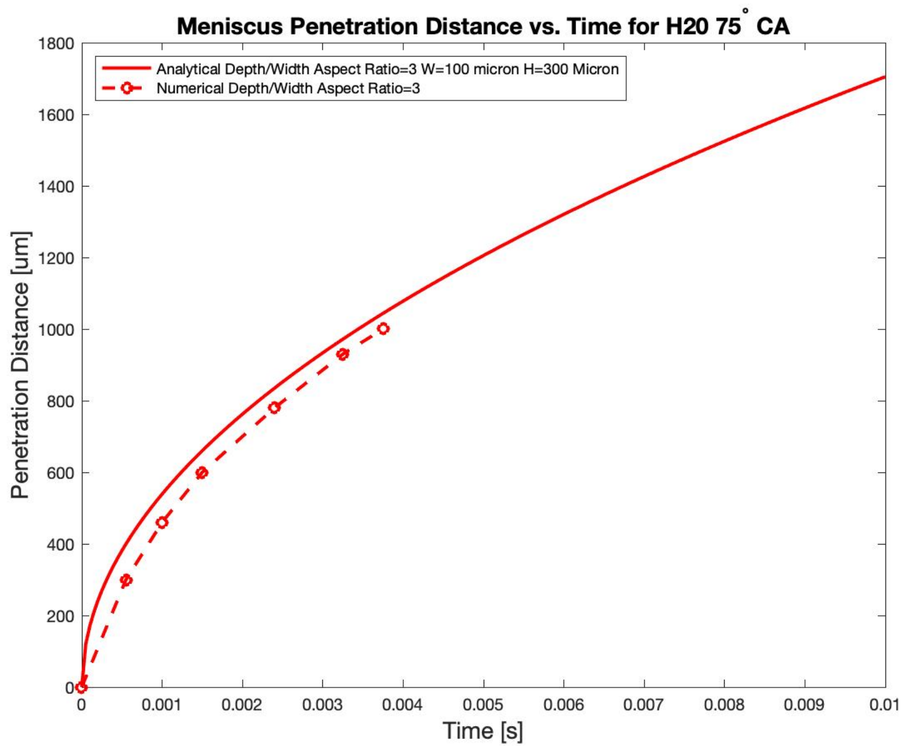

Figure 4-12: A comparison of the liquid phase boundary front propagation down an open rectangular microchannel of 100 micron width and 300 micron depth with water. Both MLW analytical and FLOW3D numerical simulation data is plotted.

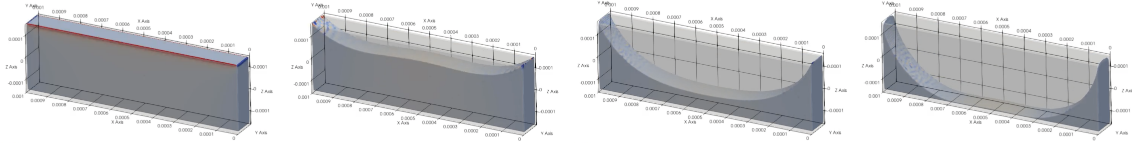

Figure 4-13: Segmentation of a liquid water filament in a hydrophobic open microchannel 100 micron wide by 300 micron deep. Note that the curvature of the meniscus is ever so slightly convex (Cassie angle of approximate 106 degrees) indicating the desired positive pressure in the channel region.

using 4.9 which suggests a pressure of 438 Pascals for water in a similar 100 micron wide and 300 micron deep channel. This is exactly the desired behavior of a physical device implemented in an electrospray thruster, albeit the end condition opposite the liquid reservoir will be slightly negative. To model this, the same channel was again simulated but with an upstream liquid reservoir relative pressure of zero and a downstream liquid reservoir with a negative 1000 Pa pressure to act as a porous media with suction.

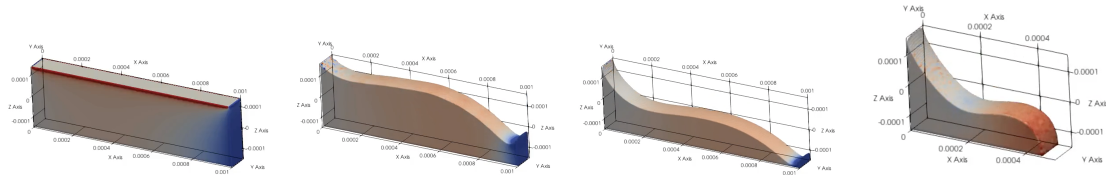

Figure 4-14: Segmentation of a liquid water filament in a hydrophobic open microchannel 100 micron wide by 300 micron deep. Relative pressure boundary condition at right end of channel is -1000 Pa.

In the case with negative reservoir pressure at one end of the channel, the segmentation still occurs, but closer to the side with negative pressure than the central channel region as in the case where the channel end boundary pressures are both neutral. Again this is beneficial to the use-case in electrospray so long as the channel is sized to provide enough propellant to the emitter that the negative pressure does not prematurely segment the liquid even when electrowetting is applied. To analytically or even numerically model this would rely on too many assumptions of perfect uniformity in porous media and perfect uniform operating conditions for the thruster, therefore a set of experimental device parameters are determined in order to demonstrate this desired segmentation with not only water, but the ionic liquid

EMI-BF4 commonly used in electrospray thrusters.

Going back to the cylindrical microfluidic device variation, a similar basic analysis of SCF onset from a neutral pressure reservoir along the gap between two cylinders, sufficiently close together, reveals that the two cylinder configuration can provide flow for liquid-solid contact angles at or below 75 degrees. We also need not be limited to strictly two or strictly cylindrical geometries, so long as sufficient rounding is present to prevent pinning (for example, a square rail would have the same pinning issues present in square microchannels), the liquid should form a negative pressure region pulling the liquid along the rails for contact angles below 75 degrees. Shown in Figure 4-15, is a Surface Evolver simulation for two cylinders (small enough to neglect gravitational effects, in this case 2mm rod diameters) are submerged slightly into an infinite neutral pressure liquid reservoir with a liquid-solid contact angle of 75 degrees. The pair of cylinders spaced at a pitch of 2.2 cylinder radii does not satisfy the SCF wetting threshold, whereas the pair spaced at a pitch of 2.04 radii does, causing the liquid to flow along the capillary rail formed by the two cylinders.

Figure 4-15: Left:Surface Evolver showing two cylinders too far apart to initialize capillary flow. Right:Surface Evolver showing two cylinders close enough together to initialize capillary flow.

By incorporating a dielectric coating and similar hydrophobic coating as in the the 3-walled microchannel devices, the cylinders would behave as the electrowetting flow controller capillary device between the reservoir and the downstream porous material.

4.4 Experimental Device Design Parameters

While there are many combinations of aspect ratio, length, and number of channels that can provide a similar flow rate, not all combinations are simple to fabricate or simple to collect data from. For the purposes of this research in demonstrating reversible electrowetting flow control for ionic liquids, channel depths between 200 micron and 1mm are explored. This will ensure that the channel widths necessary to produce SCF are large enough to capture the meniscus dynamics using a microscope in a lab environment while still neglecting gravitational effects. Additionally, for each rectangular channel device iteration, the sharp interfaces must be rounded to a degree that prevents pinning during operation. While there are analytical ways to determine these values, the degree of sufficient rounding will be experimentally iterated via multiple fabrication approaches leading to the final device design. The cylindrical configuration trial will utilize commercially available polished metal cylinders no larger than 0.25 inches in diameter. The experimental device fabrication approaches will be outlined in the following chapter.

Each microchannel will also require a liquid reservoir as well as a second reservoir at the other end of the channel if emitter material is to be in contact with the liquid in the channel. This "dumbbell" layout is shown in Figure 4-16.

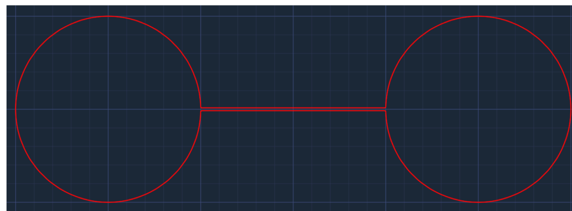

Figure 4-16: A 2D design of an open microchannel device with 2 circular reservoirs at either end.

The cylinder configuration will simply be submerged into a shallow dish filled with liquid, and a piece of filter paper used in the electrospray fluid path will be placed at the top of the cylinders to simulate the end condition of a downstream emitter.

Lastly, in order to accurately and repeatably control where the change in contact angle of the liquid in the channel (and hopefully liquid segmentation) occurs, selective

hydrophobic coatings should be employed. This ensures that the liquid can segment in the same location every time and no portion of the test set-up can interfere with the liquid near the reservoirs of a device.

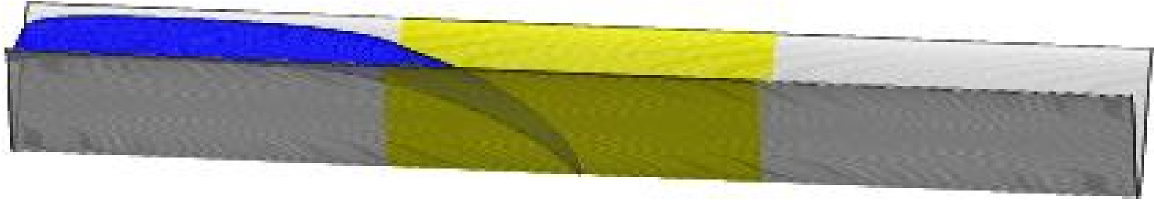

Figure 4-17: A rounded open microchannel with a hydrophobic region located in the central region (yellow) and hydrophilic regions on either end (gray.)

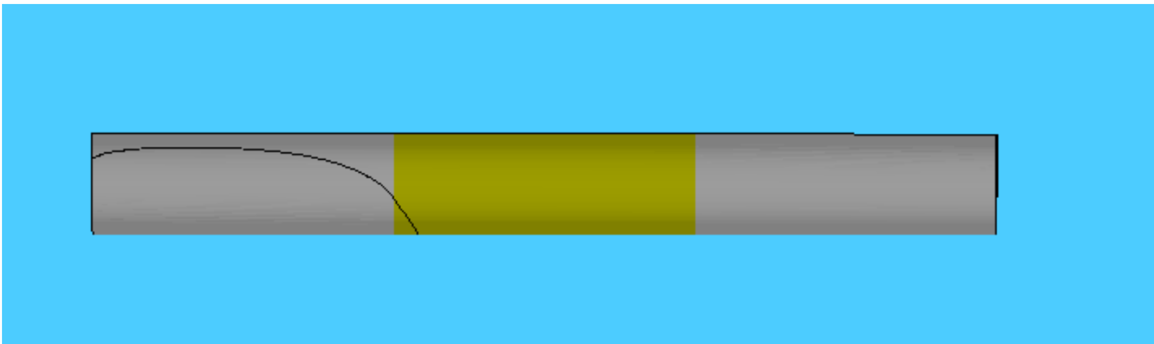

Figure 4-18: Surface Evolver simulation of liquid flowing up to point of the hydrophobic region.

Shown in Figures 4-17 and 4-18 are sinusoidal (rounded and smooth) open microchannels with a central region that is hydrophobic. The inlet and outlet regions of the channel are still hydrophilic as to ensure that the liquid always is present at the boundaries of the electrowetting control region. The operation of this style of device is not unlike that of an electrowetting droplet splitter. The liquid from the upstream reservoir flows into the channel up to the hydrophobic region where the contact angle is not sufficient to continue flow. Application of a voltage to lower the contact angle via electrowetting will then allow flow to traverse this region onto the third and final hydrophilic region that will then transport the liquid to some porous media at the end of the channel (in this case an electrospray emitter.) When the voltage is removed, the meniscus is free to evolve based on the increase in contact angle in the central channel region where the hydrophobic coating is located. Once

this liquid in this region forms a positive pressure relative to the reservoir ends, a capillary instability should form and liquid segmentation should occur in a similar fashion to the segmentation shown in the numerical simulations discussed earlier. Although designing a curved open microchannel with a selective hydrophobic region may be a simple exercise on a computer, fabricating such a small device is quite the challenge.

THIS PAGE INTENTIONALLY LEFT BLANK

Chapter 5

Fabrication Techniques for Experimental Electrowetting Flow Controller

Open microchannels are physically very simple structures. Rectangular microchannels being one of the simplest of them all. This simplicity lends itself to easier methods of fabrication, however, due to the small scale of the channels, smoothness and uniformity in the channel walls is crucial to achieving devices that come close to the predicted performance values which presume perfectly smooth and uniform walls.

5.1 Conventional Fabrication Techniques

For the purposes of this section, "conventional" fabrication refers to methods such as machining, pressing/stamping, and 3D printing of metals and plastics. All of which are generally suitable for features no smaller than about 0.5mm.

5.1.1 Machining

For larger single channel devices with greater flow rate capacities, metallic milling was explored. Given that these devices would be tested in a lab setting in the presence

of gravity, they would still need to be small enough in characteristic length to ensure the Bond number is below (ideally well-below) unity. This ensured that the capillary forces of interest are sufficiently more dominant than gravitational effects.

6061 aluminum blanks of 1/8 inch thickness and 1/4 inch thickness were used for mill work. Two 1 inch diameter reservoirs are milled to the desired channel depth with enough length separating them for a microchannel to be milled between them. A 1/32 and 1/64 end mill were used to mill the rectangular channels in this case. Once the channel is milled, the exposed edges are then radiused with a radiusing mill bit. Overall, this is probably the easiest form of manufacturing an electrically conductive microchannel base for use in these electrowetting flow controller tests. One of these aluminum microchannel devices is shown in the figure below:

Figure 5-1: Several milled microchannels in an aluminum bar prior to sawing into individual devices.

5.1.2 Stamping

Also within the category of conventional fabrication techniques is stamped channel geometries. Given the aspect ratio needed for liquids like water and EMI-IM being less than 3, stamping was investigated as a potential channel manufacturing technique, albeit likely not suitable for the higher aspect ratios needed for liquids like EMI-BF4. To stamp a microchannel, a tool steel positive was first milled via CNC. This approach has the added benefit of having tight control of the edge radiusing of each channel. A steel positive device is shown in the figure below:

Figure 5-2: A CNC milled steel positive microchannel device used to stamp softer metals.

The steel positive device is then used to stamp the milled geometry into a softer polished metal substrate. Both copper and aluminum were used as a stamping metal with decent success. Copper has better ductility and thus provided better capture of the impressioned geometry although requiring a larger stamping force. To stamp the polished copper and aluminum, a pneumatic press was used to generate the approximately 4000 psi necessary to press the steel fully into the copper. A stamped copper device is shown in Figure 5-3.

After the stamping process was completed, the channel cross section was inspected with an optical profilometer and the profile results are shown in Figure 5-4.

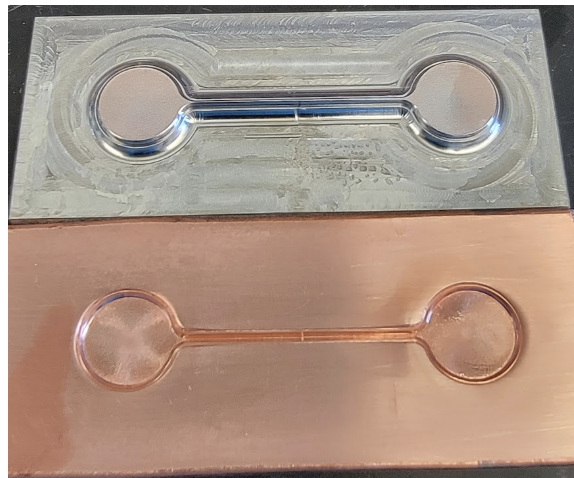

Figure 5-3: A stamped copper substrate with the steel positive geometry transferred into the softer copper under 4000psi.

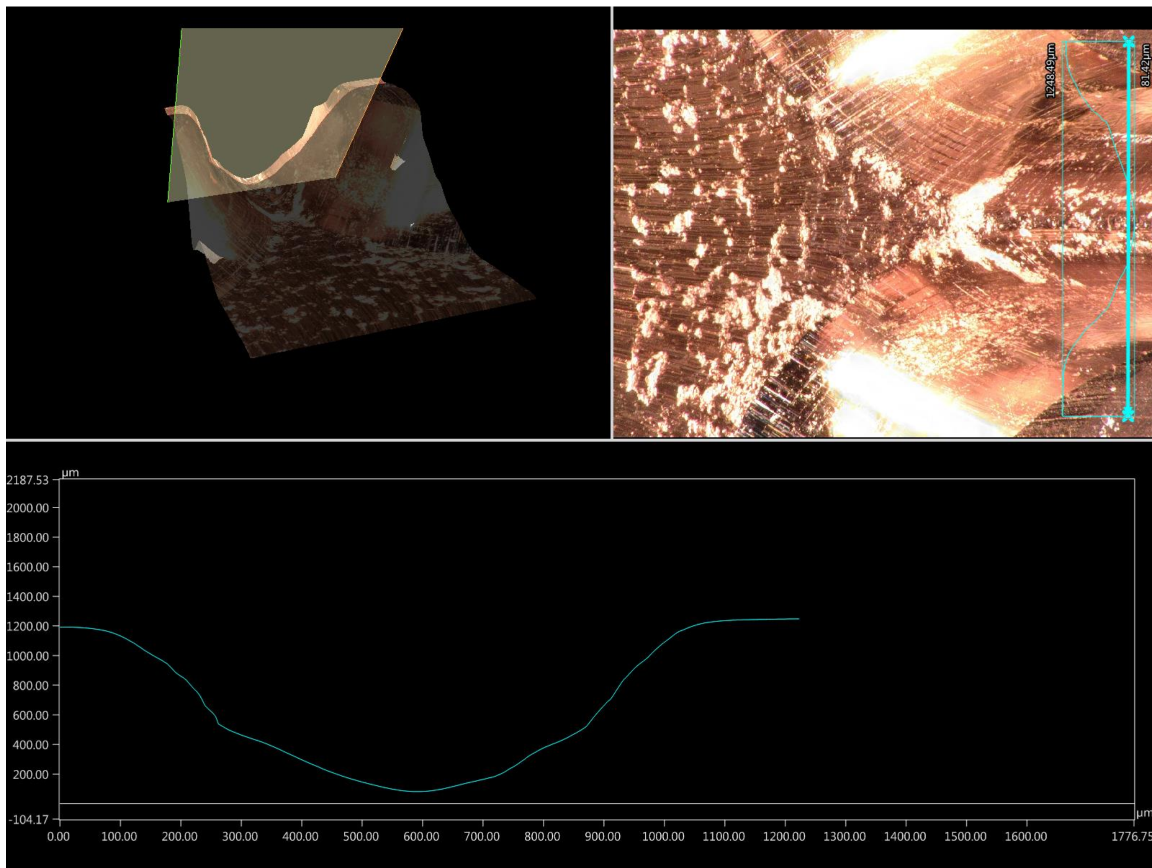

Figure 5-4: Profilometer results for the stamped copper microchannel. Note the extensive rounding of the channel edges. Also note the difference in axis scale in the cross-section measurement profile.

As far as rounded rectangular microchannels with aspect ratios less than 3 are

concerned, stamping is a relatively straightforward and cost-effective fabrication technique. Deeper channels with higher aspect ratios require such high stamping loads that even ductile metals like copper eventually fracture before capturing the entire channel imprint, although this does have a scale-dependency. It may also be feasible to stamp softer materials and then deposit metallic and dielectric layers atop them, but for the purposes of this research, metallic stamping was too varied in outcome.

5.1.3 3D Printing

With the maturation of consumer and commercial grade 3D printing technology over the years, it has never been easier to 3D print small and delicate parts. The Space Propulsion Lab has an in house Formlabs Form 2 sterolithographic 3D printer capable of printing microchannels in a variety of plastics. While metallic 3D printing is also an option, the peceding methods discussed worked suitably well in metals with better surface finish than is easily achievable from 3D printing. A test device was designed and printed with the Form 2 printer in ABS plastic, but again, the desired channel aspect ratios were not captured well by the 3D printer even on its finest resolution settings. A test print of a device is shown in the figure below:

Figure 5-5: A 3D printed ABS plastic variant of the milled tool steel microchannel device.

Given that the electrowetting device would need to be conductive, even a perfectly printed plastic microchannel device would then need a conformal electrode coating to be a viable fabrication candidate. Although there are likely tools and combinations of coatings and platings available, 3D printing was not deemed a suitable candidate for fabricating the electrowetting flow controller test devices.

5.2 Microfabrication

Microfabrication or micro-electromechanical system fabrication (MEMS) is a fabrication method that relies on the addition or subtraction of small featured from a planar (typically silicon) substrate via the use of thin film deposition, photolithography, and etching. It is the basis for fabricating a variety of micro-scale components such as microchips, microfluidics, integrated circuits, and many other sub-millimeter technologies.

5.2.1 Binary Photolithography

Photolithography is a very common MEMS fabrication process widely used at nearly every level of cleanroom microfabrication. Simply put, photolithography begins with coating a silicon wafer with a photo-curable polymer, often using a centrigugal spin coater, baking it in an oven to evaporate solvents, then exposing the photoresist to a UV source. As with oxides, there are a variety of photolithography processes available. Photoresist is generally classified as either positive or negative. For positive, the UV light degrades the cross-linking of the photocurable polymers. For negative, the UV exposure promotes cross-linking. The extent of the cross-linking during exposure decides whether the photoresist is removed by the chemical developer, typically a mixture with tetramethylammonium hydroxide (TMAH), for positive resist, or left intact in the case of negative resist. For the work in this thesis, two types of positive photoresist are commonly used: AZ-3312 and AZ-10Xt, often referred to as "thin" and "thick" resist respectively. Thin resist is typically used to produce one micron thick layers, while thick resist is used for coatings in the tens of microns. Thin resist is less viscous and easier to coat, while thick is much more viscous and more difficult to deposit correctly. Thick resists are usually only needed for when etching times may compromise the thinner 1 micron resist masks. This spin coating is shown in Figure 5-6.

Photolithography used in this work falls in the two categories of optical projection, "contact" photolithography, or maskless "contactless" photolithography. Contact

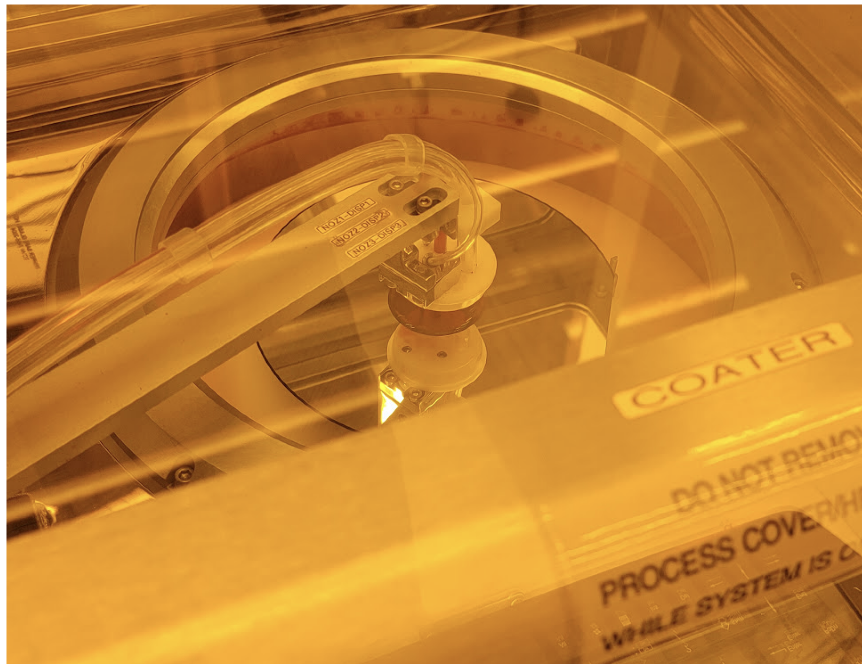

Figure 5-6: Spin coating a wafer with photoresist.

photolithography has readily become the standard approach due to simplicity, speed, and high resolution. For this approach, a transparent mask usually backed with a chrome layer has the pattern to be transferred onto the photoresist layer. The solid mask is brought into contact with the wafer, then UV light is projected onto the mask for a set amount of time. The exact time depends on the feature size, resist thickness, and resist type. While this process is highly reliable, the chrome backed masks are custom made for each design and add to the overall development time and cost.

Enter maskless photolithography. Instead of creating an entirely new physical mask for every feature/design change, a finely tuned UV laser can be precisely manipulated across the surface of a resist-covered wafer to expose a unique pattern without a mask. This form of photolithography is not without its drawbacks, however. First, it is much slower than optical projection with a mask. It typically takes about an hour to produce a full six-inch wafer pattern at acceptable quality. With larger features, lower resolution, and less area exposed, this can be trimmed down though. Another point: the laser spot size limits the critical feature size to about 1 micron. Anything below that will suffer a spot size exposure larger than the detail

needed. While cheaper than designing and building a contact mask for development work, it does cost significantly more to run this process when compared directly to contact photolithography once the mask is on hand. If the design is constantly changing, this process obviously has a significant advantage. New designs can be drawn, converted for use in the maskless aligner tool and exposed in an afternoon. To that end, in the MEMS world, this tool is analogous to a 3D printer of sorts.

Both of these tools are generally able to exposure aligned patterns from either top or back-side alignment marks. The UV source is exposed only to the top surface, but it is common to pattern a complementary design on the back side of the wafer. To enable this, cameras are mounted to the top and bottom of the wafer chuck. The alignment of the pattern in the mask to the complementary pattern is achieved using alignment crosshairs. Using the cameras, the wafer chuck can be adjusted so the alignment marks pair with the mask. This ensures the patterns are aligned to each other on both sides of the wafer. For back-side alignment, the mask alignment marks are on the opposite side of the patterned wafer. This requires alignment locations on the mask to be noted by the bottom cameras. The wafer is then loaded in to the chuck and aligned to these locations before exposure.

Another useful technique within photolithographic fabrication is known as "nested mask" photolithography. This technique entails the patterning of an oxide layer beneath a photoresist layer to enable several etch steps with differing features. In the development work for the electrowetting flow controller, a technique for very shallow (approximately 10 micron) nested masks where both are made of cured photoresist. This is necessary to have a open-channel pattern as well as a wick retaining border on the same wafer side. This is permitted by first masking the channels, etching no more than 10 microns deep and then spin coating more photoresist on top of this side for further pattern exposure. This can be done using either contact or contactless approaches with thick resist, but may have vortices induced in thin resist interacting with the etched features.

5.2.2 Grayscale Photolithography

Whereas traditional lithography techniques result in binary features being left in a photoresist after development, "grayscale" lithography utilizes a multi-dose exposure technique, typically using a variable output laser, to produce 3D photoresist features after development. This means that more complex, curved profiles can be produced in a photoresist prior to etching into a silicon substrate. As mentioned prior, rounded profiles are crucial for the electrowetting flow controller device to avoid liquid pinning on sharp ledges or interfaces that are typically present in binary lithography etch results. Shown in Figure 5-14 is an SEM image of a multi-dose grayscale photoresist mask after development.

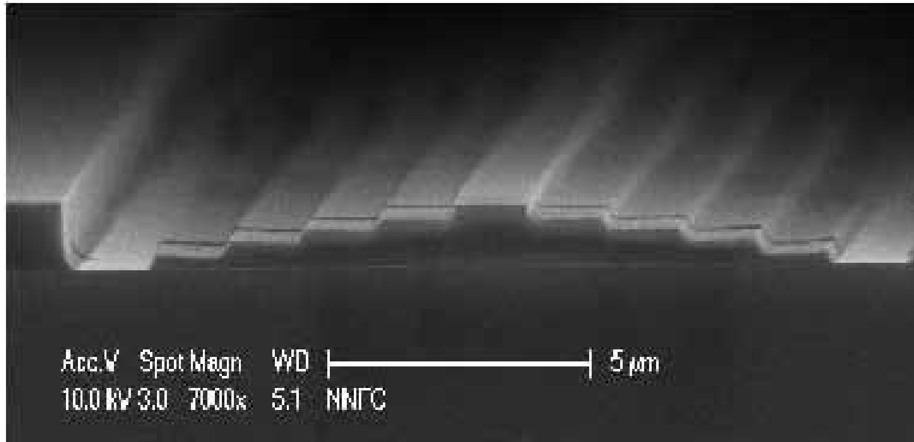

Figure 5-7: SEM image of developed grayscale lithography "stairsteps." Image: SY Lee - Auburn University

Grayscale was initially seen as the most promising fabrication method for the rounded rectangular microchannels desired for the electrowetting flow controller. Given the need for various aspect ratio channels for testing, several grayscale exposure trials were conducted using MIT Nano's Heidelberg MLA150 tool. First, a 7 micron thick layer of 10XT photoresist is spun onto a silicon wafer and pre-baked. A series of DXF files with multiple layers corresponding to specific dosages was created in order to determine the dose-depth profile for grayscale in the 10XT resist. The minimum feature size in 10XT the MLA150 can readily handle is about 1-2 microns, so each strip was made to be 10 microns for ease of measurement and replicability.

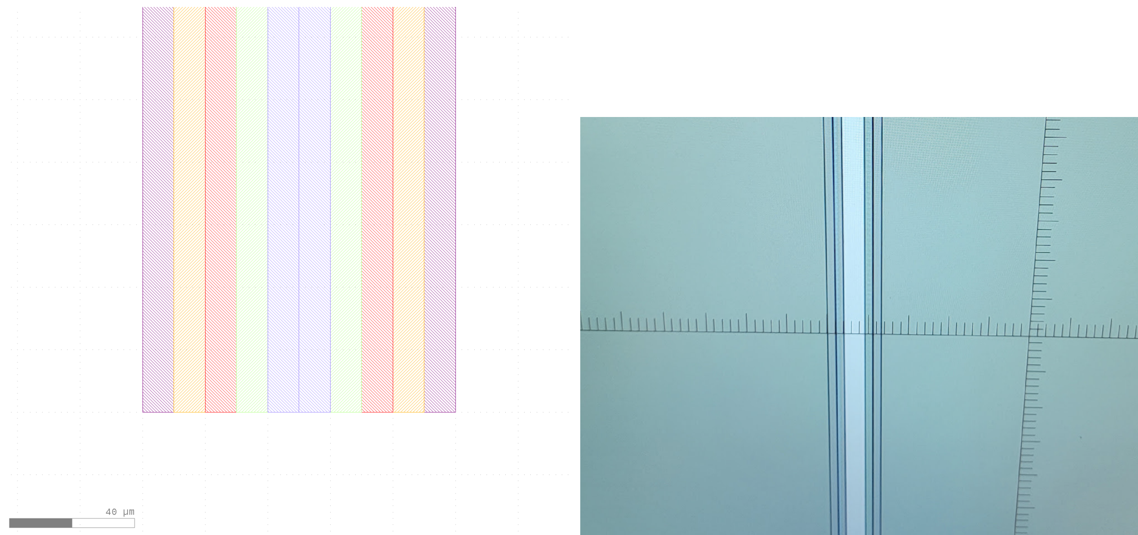

Figure 5-8: Left: Grayscale multi-layer design file for simple stripes; total width is 100 microns. Right: Exposed and developed pattern viewed through microscope, note distinct lines correspond to different dose strips; total width is 100 microns.

The preliminary exposure results from the design file are shown in Figure 5-14. Once every exposure was complete and developed, a profilometer was used to measure the strip depth in order to back out the dosage-depth profile needed for creating rounded features. An example of one profilometer readout is shown in Figure 5-16.

Once the clearing dose for the resist was known and dose-depth relation was known, 255 gray values are available for tuning the curvature of the desired feature. Effectively meaning there is a depth resolution of 7 micron divided by 255 gray values which works out to about 27 nanometers be gray value option, although not strictly linear.

In order to translate these grayscale photoresist mask features into silicon, the wafer still needs to be etched anisotropically via deep reactive ion etching. But before that process, the grayscale features need to be smoothed slightly to minimize the sudden step changes with each dosage value. This process is collectively called resist reflow.

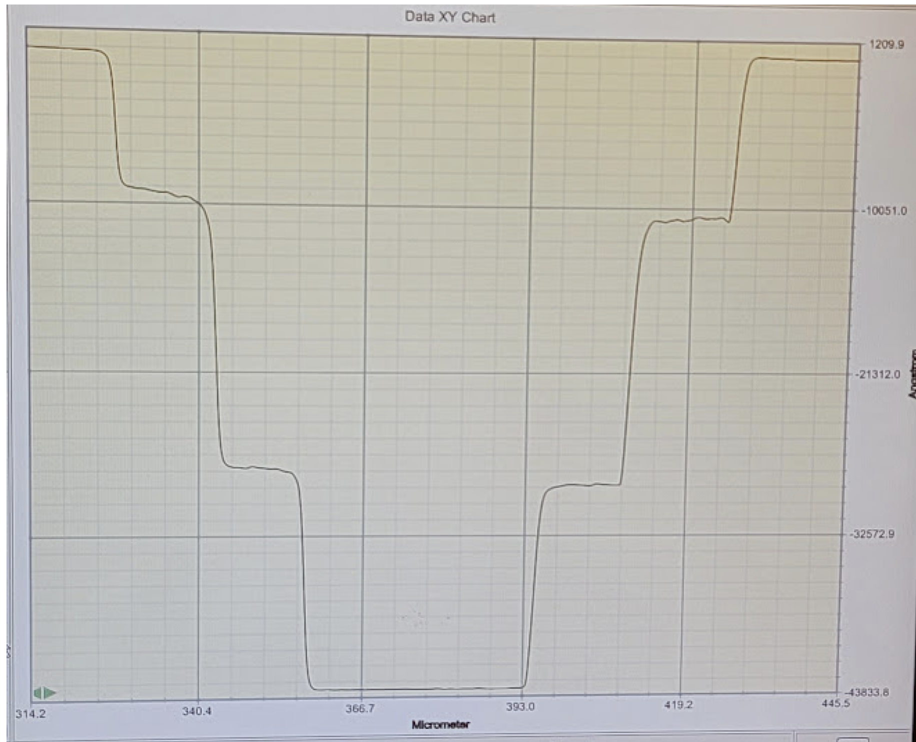

Figure 5-9: Profilometer data for a grayscale test exposure of several differing-dosage strips in 10XT resist.

5.2.3 Resist Reflow

Whether binary or grayscale lithography is used, the photoresist mask layer is almost always going to still be made up of features that have 90 degree transitions. These sharp transitions, once transferred into silicon via etching, will be perfect spots for liquids to pin to, therefore, smoothing them out prior to etching is essential. Once the photoresist is exposed and developed, the wafer with resist may be placed back onto a hot plate at a temperature slightly above the resist's softening point to purposefully "reflow" the structure and soften the transitions between regions with different dosages received during exposure. This method is very cheap, takes only minutes to complete, and results in very smooth topologies. It is not without its drawbacks, however, as it will become clear, reflow results are not always predictable or perfectly repeatable, especially across the surface of a large silicon wafer. Nonetheless, the grayscale exposed open microchannel profiles were subjected to a variety of reflow tests using a hot plate set at 150 degrees Celsius.

It was found that a 60 second post-bake reflow at 150C on a hotplate of the developed grayscale patterns, sufficiently smoothed the edge transitions and resulted in very smooth curved mask features. Figures 5-10 and 5-11 show the smoothing effect of the reflowed grayscale resist mask.

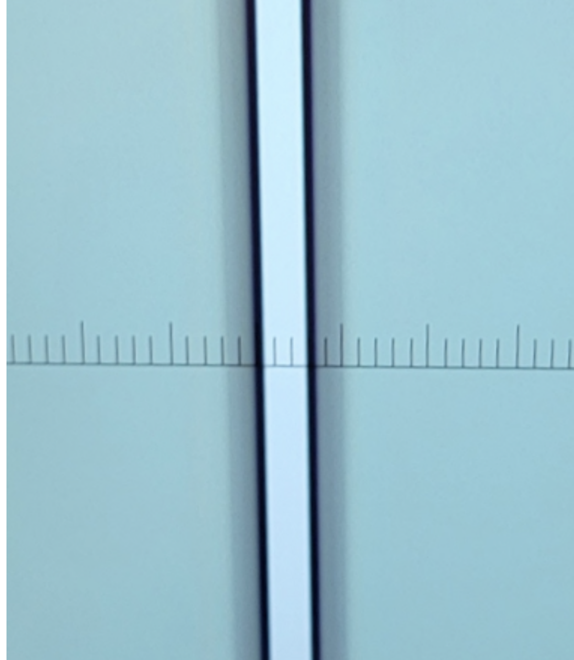

Figure 5-10: Microscope view of reflowed grayscale photoresist mask, note the lack of distinct dosage strip lines after reflow.

Despite these very smooth lithography mask features, the curved portions of the channels can only transfer into silicon fully once the resist that makes up the curve is fully etched away. As will be discussed in the next section, etching these smooth profiles into silicon comes with many difficulties in preserving the desired profiles in silicon after etching.

5.2.4 Deep Reactive Ion Etching

DRIE (deep reactive ion etching) is a standard anisotropic silicon etching technique used in MEMS fabrication. This process is widely employed with very successful results. The contemporary recipe is called the Bosch process. It includes alternating steps of plasma etching and isotropic passivation. During the plasma etching phase,

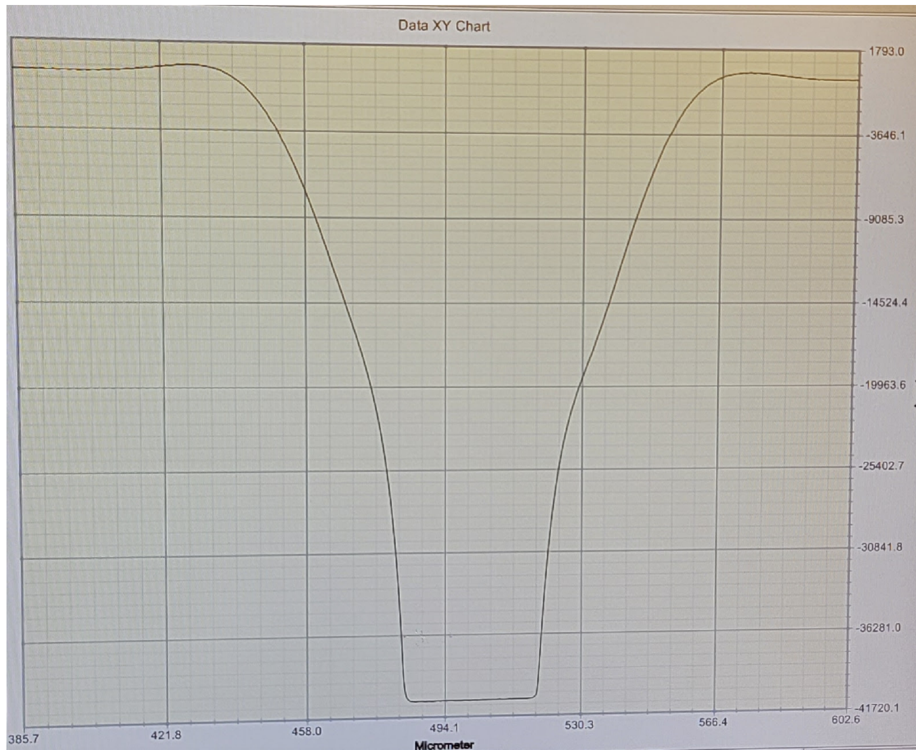

Figure 5-11: Profilometer data for a grayscale test exposure following a 60 sec 150C hot plate reflow.

a sulfur hexafluoride (SF_6) plasma is directed at the silicon wafer to be etched by applying a voltage between the source and the wafer chuck. The SF_6 partially dissociates while the fluorine atoms react and etch the silicon away. During the passivation phase, a C_4F_8 fluorocarbon plasma is produced and adsorbed onto the wafer surface and polymerizes to form a thin non-reactive fluoropolymer film. The SF_6 plasma is unable to etch the fluoropolymer layer. However, with a bias applied, the ions can sputter away the coating normal to the biased wafer chuck, and etch the underlying silicon away. This repeated process produces very small etched scallops that, together, provide a very directional anisotropic etch result. As mentioned, thermally grown oxide resists chemical etching very well. However, the oxide will eventually be etched away. Typical selectivity ratios of 200:1 can be expected for etch rates between silicon oxide and bare silicon.

While very much different depending on tool and/or process used, etch aspect ratios of 20:1 can typically be achieved with DRIE, When the aspect ratio reaches its

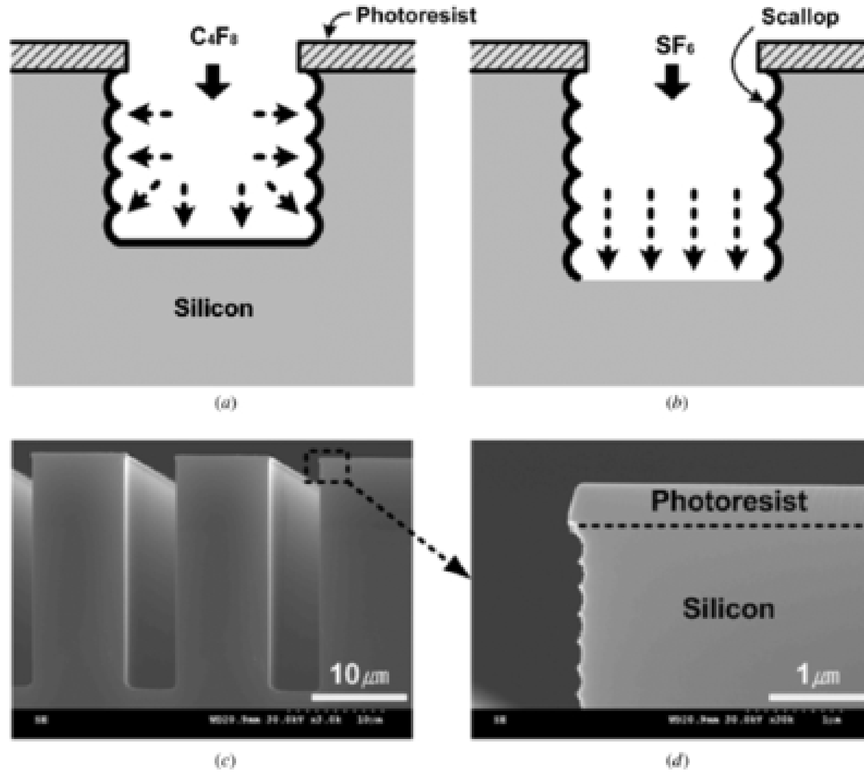

Figure 5-12: DRIE etch effect in silicon substrate. The etch and passivation steps (Bosch process) show the scalloping effect. [41]

maximum, the etch slows due to lack of plasma reaching the silicon surface. Formation of black silicon can occur when this happens which further slows etch rates and requires an increase in SF_6 to undercut and clear any black silicon forming. These tools are also capable of providing isotropic etching for undercutting the oxide mask layer or to stop the production of black silicon. By turning off the applied bias as well as the passivation step, the etch becomes strictly SF_6 plasma driven and isotropic.

For simple rectangular microchannels, a binary lithography (single dosage instead of multiple like grayscale) resist mask is suitable to achieve many aspect ratios. Shown in Figure 5-13 is a SEM cross-section of a microchannel produced with simple binary lithography and a DRIE etch profile. While DRIE often leaves slightly rounded corners in the bottom of deep trench feature such as a microchannel, the top ledges, once the photoresist is removed, remain quite sharp which would lead to the undesirable liquid meniscus pinning to them.

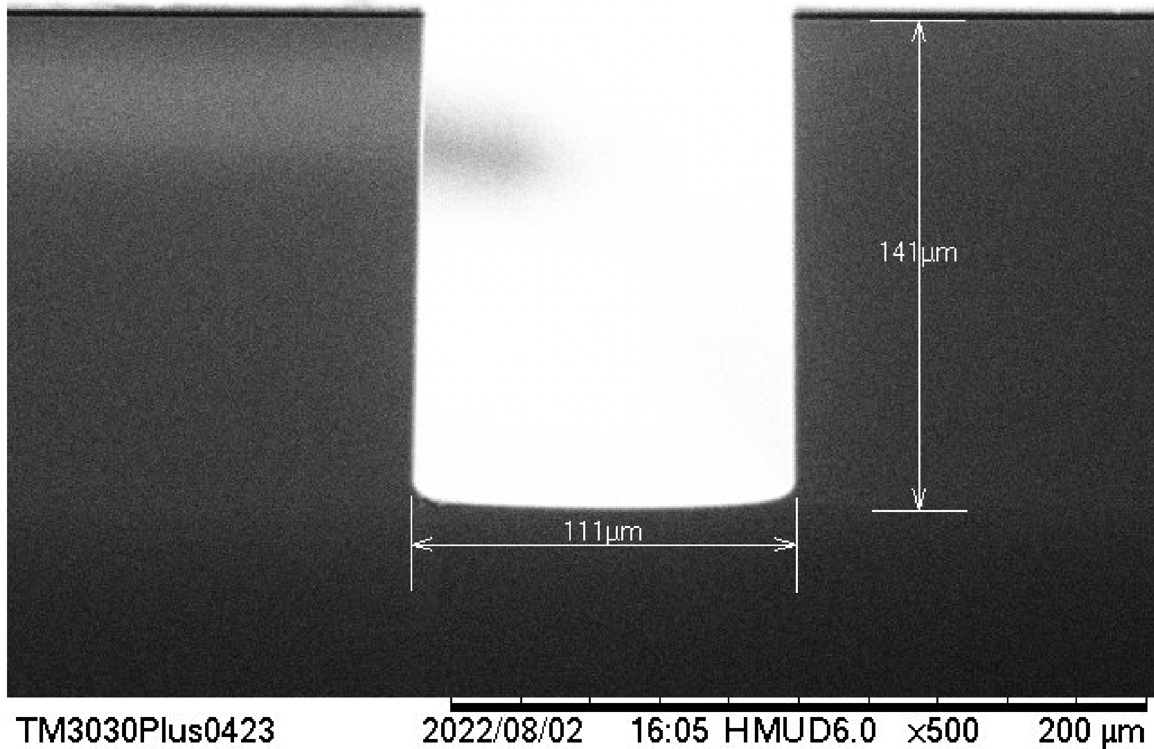

Figure 5-13: SEM cross-section view of a partially etched microchannel using DRIE and binary lithography. Note the black line showing the remaining thin film of photoresist at the top of the silicon wafer.

Deep Reactive Ion Etching of Grayscale Patterns

As seen in the grayscale lithography and resist reflow images in the prior sections, smooth, rounded features can be readily achieved in a thin film photoresist mask. However, these features need to be transferred into silicon to achieve the much larger hundreds of micron scale microchannels. By utilizing directional deep reactive ion etching with a silicon to photoresist etch selectivity of approximately 60, these smooth features were expected to transfer into the underlying silicon scaled by the selectivity of the etch recipe. This selectivity effectively means that for every 60 microns of silicon etched, 1 micron of photoresist is etched away. After using the same parameters used to generate the microchannel profile seen in Figure 5-11 on a wafer with multiple

single-channel devices. This grayscale device mask is shown in Figures 5-14 and 5-15. This mask was generated by spinning a 7 micron thick layer of photoresist onto a silicon wafer. Then rectangular regions are exposed to give a film height of 5 micron post-development in order to determine when the etch has fully transferred the curved microchannel geometry and reservoirs into silicon.

Figure 5-14: Grayscale exposure photoresist mask atop a silicon wafer. Devices are 100 micron wide microchannels 5mm long with two 5mm diameter reservoirs at either end.

Figure 5-15: Top down microscope image of the grayscale device mask. Note the "cornrow" features that remain atop the 5 micron thick region of the grayscale photoresist mask even after reflow of the resist.

After several etch trials using an STS Pegasus with a silicon to photoresist etch selectivity ratio of approximately 60, it was determined that film thickness variations on the order of a hundred nanometers or less were creating significant variations in etch depth in the silicon. Variations in silicon feature sizes may also be due to inconsistencies from resist reflow.

After three attempts at grayscale lithography transfer of rounded microchannels,

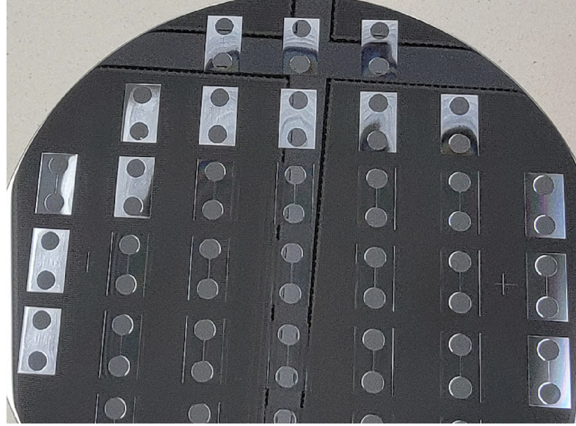

Figure 5-16: Etched grayscale photoresist mask. Note that some devices reached the silicon layer before others due to photoresist being slightly thicker in the lower half of the wafer.

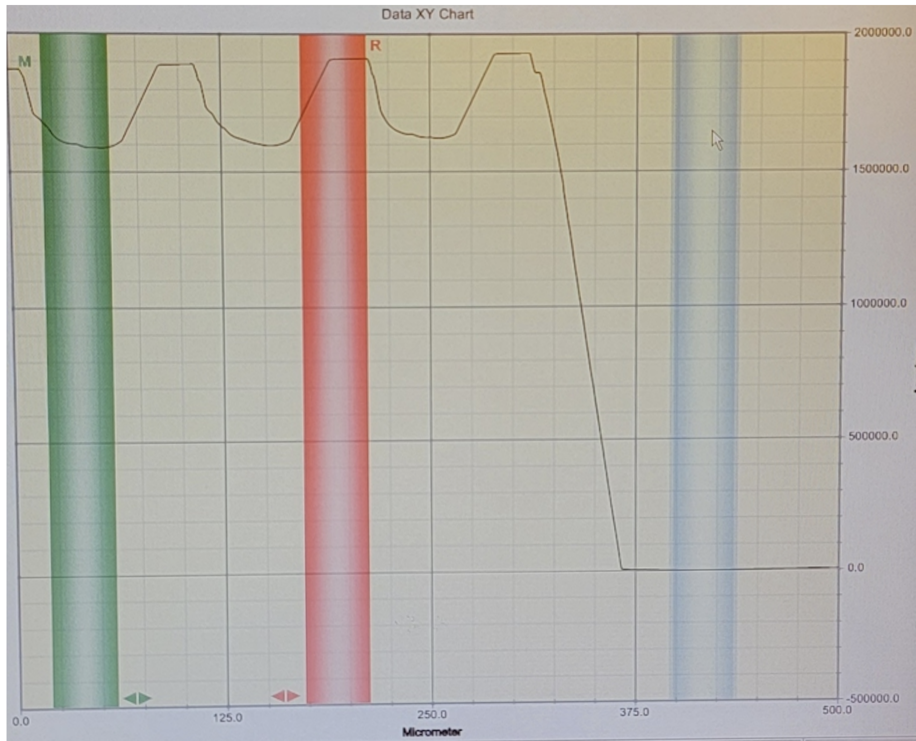

Figure 5-17: Profilometer data of the etched grayscale lithography devices. Note the transfer of the small "cornrow" features in the resist scaled up by the etch selectivity ratio.

the silicon features rarely achieved the same smoothness that is present in the reflowed resist mask. Therefore, it was determined that a simpler binary lithography approach coupled with an isotropic secondary etching process to smooth sharp interfaces present

in silicon after DRIE would best ensure no unwanted liquid pinning occurs. That being said, grayscale was very close to achieving a reliably consistent feature-rounding effect. It was also learned that optical interference patterns were present in the tool used to produce the grayscale masks that lead to the small lines that transferred into the silicon. Once this issue is addressed, the tool, and subsequent grayscale process, may be a very viable fabrication option.

5.2.5 Isotropic Etching

In order to attain smooth, rounded features in the open microchannel devices, one possible technique is isotropic etching. Isotropic etching can be done either via wet chemical etching with a hydrofluoric acid or buffered oxide solution if the substrate is silicon dioxide or with a plasma if the substrate is silicon. An SF6 plasma etch serves as the isotropic etching technique utilized in this work. Following the DRIE etching of simple rectangular microchannels of varying aspect ratio, a short SF6 plasma etch sufficiently rounds the sharp features while preserving the approximate aspect ratio. To avoid creating undercuts or sharp interfaces, the photolithographic mask must first be removed and all silicon intended to be etched must be exposed and clean.

The radiusing effect of the SF6 etch on the corner leaves the desired smooth, rounded ledge to prevent liquid pinning once the microchannel has wetted. This does widen the channel somewhat as the exposed channel walls and bottom surface are etched outward more as well, so this must be accounted for in the initial mask design.

5.2.6 Silicon Oxidation

In nearly all micro and nano fab processes in silicon, oxidation is the first step. This is primarily due to the nature of silicon dioxide being a strong dielectric as compared to silicon as well as being much more resilient to DRIE plasma etching as compared to silicon. Per micron deposited, it takes on the order of 1 kilovolt to cause dielectric breakdown. As a mask material, selectivity is often on the order of 200:1 compared to silicon, meaning high-aspect ratio features can be preserved more readily than with

a photoresist mask with selectivity around 60:1 with silicon.

Figure 5-18: Wafers entering a furnace for thermal oxide growth. The quartz holder is needed to withstand the hot environment.

To produce this oxide layer, two techniques are commonly used: thermal oxide growth and plasma enhanced chemical vapor deposition. For thermal oxide growth, the first step is a thorough chemical cleaning of the wafers which removes organic materials, particles, and the imperfect native oxide layer. The bare silicon wafers are then placed into a tube furnace, supplying a uniform oxidizing atmosphere at very high temperatures, on the order of 1000 $°C$. This high temperature speeds the rate of diffusion of the oxidizing agents into the silicon. Two variations of thermal oxide exist: "wet" oxidation, which uses H_2O as the oxidizer, and "dry" oxidation employs O_2. Wet oxidation is a much faster growth option due to diffusion of water through silicon being higher than O_2. There are penalties to oxide density and uniformity with this option, however, but the length of time needed for micron-scale oxide from

dry oxidation is prohibitively long.

The Deal-Grove model of silicon shows a decreasing rate of oxide growth as thickness increases. For a set oxide thickness X:

$$X(t) = \frac{A}{2}\left[\sqrt{1+\frac{4B}{A^2}t}-1\right] \quad (5.1)$$

where A and B correlate with the temperature and chemical kinetics. [42] The thickness is directly proportional to the root of the growth time. Therefore, longer deposition times begin to asymptote with thickness of oxide gain, typically around a few micron.

The wet thermal oxidation technique is used as one possible dielectric for the electrowetting flow controller devices. Once the channels are etched into the silicon and rounded as desired, they are cleaned and oxidized in the following steps:

1. Load wafers and heat furnace to 1050°C, with constant nitrogen flow.

2. 20 minute N_2 purge.

3. 20 minute dry oxidation.

4. 50 minute wet oxidation.

5. 20 minute dry oxidation.

6. 20 minute N_2 purge.

7. Cool to 300°C and unload wafers.

These steps result in a roughly 500 nanometer thick oxide layer, verified via ellipsometry metrology, suitable as a dielectric layer for electrowetting applications. Additionally, one can grow a thermal oxide into silicon and then etch away the oxide to achieve a similar rounding effect on any sharp features left from the DRIE process. An example of this rounding effect is shown in Figure 5-19.

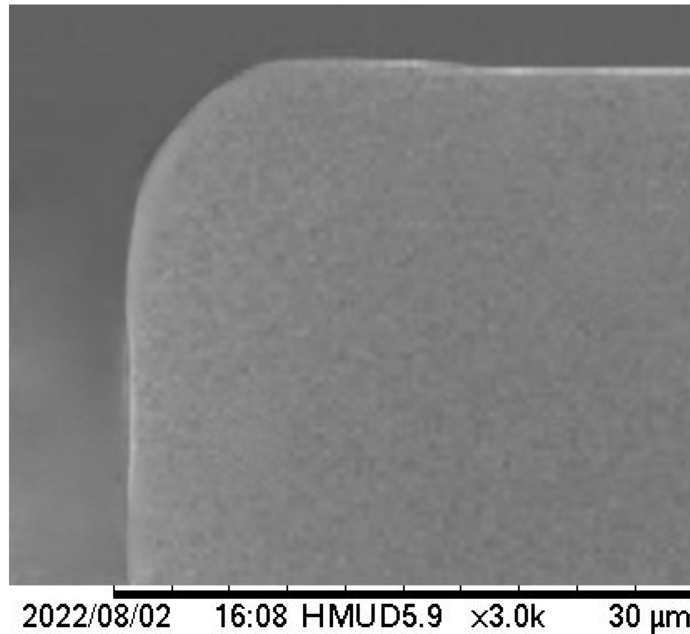

Figure 5-19: SEM cross-section view of a DRIE etched and subsequently cleaved rounded-microchannel corner. A 2 micron thermal oxide layer is grown into the silicon then etched away with a buffered oxide etch to leave a rounded ledge.

Unlike oxide growth into the silicon substrate, with oxide deposition, the oxide is developed on top of the substrate through chemical vapor deposition (CVD). A typical reaction may be between silane and oxygen:

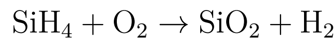

$$SiH_4 + O_2 \rightarrow SiO_2 + H_2$$

When done in an ionized environment, this process is sped up dramatically. This deposition is known as plasma-enhanced chemical vapor deposition (PECVD). [1]

Thermal oxidation is an excellent dielectric for use in electrowetting devices since it is grown into the silicon and effectively a conformal dielectric. However, as will be noted in the testing results sections, 500nm thermal oxidation of silicon would occasionally leave small pinhole defects inside of the etched microchannels where a short would form once in contact with a conductive liquid held at a higher voltage. Therefore, alternative and/or additional dielectric coatings are needed for robustness.

5.2.7 Evaporative Parylene Coating

Parylene is an exceptional conformal polymer dielectric material used in many biomedical devices due to its compatibility with a wide array of materials. It has the added benefit of having no pinhole defects when applied via chemical vapor deposition (CVD) technique. The application process generally involves three steps: generation of the monomer gas, absorption on the cleaned device surface, and polymerization of the adsorbed film.

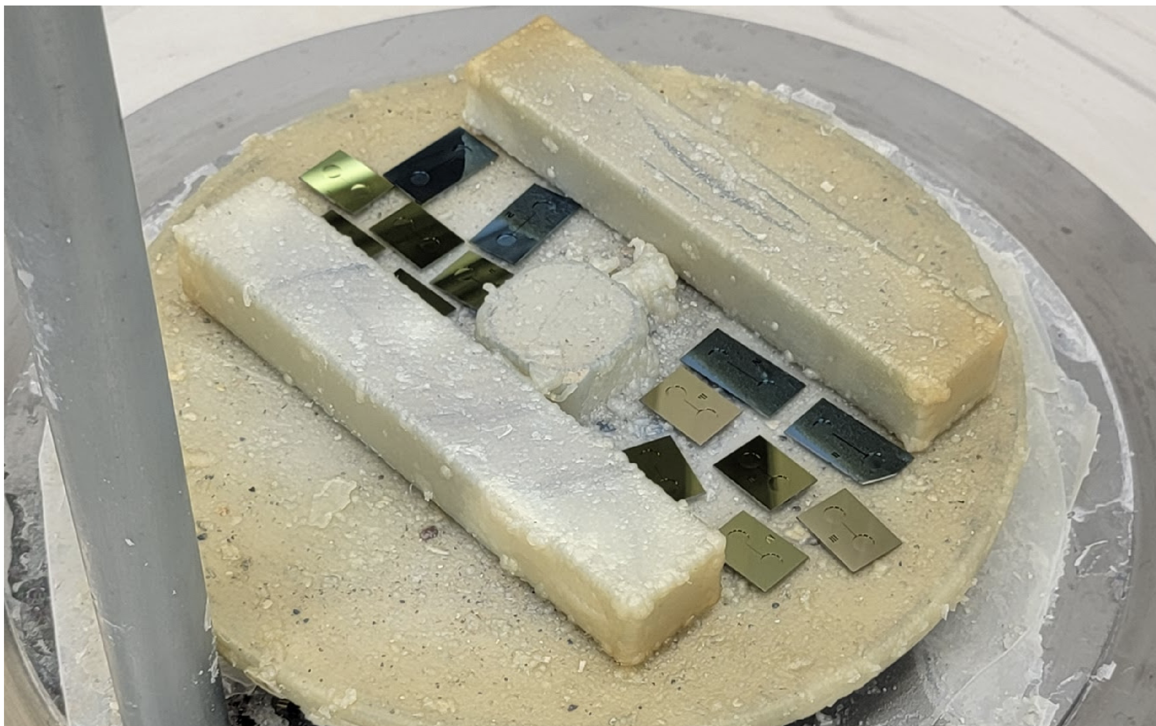

Figure 5-20: Open microchannel devices after coating with parylene via CVD.

Parylene deposition is done effectively at ambient temperature inside of the deposition chamber. Meaning a wide range of compatible materials can be parylene coated. Parylene C is often used as a dielectric in electrowetting devices and can even be modified via O2 or SF6 plasma to increase or decrease its surface wettability. [43], [44]. However, many hydrophobic coatings are available to achieve electrowetting in microfluidic devices.

5.2.8 Hydrophobic Coatings

Hydrophobic coatings are effectively any thin film that results in a water droplet contact angle greater than 90 degrees at the interface between the water and the hydrophobic surface. Chemical vapor deposition, plasma enhanced chemical vapor deposition, spin coating, spray coating, dip coating, and sputtering are all viable application methods for common hydrophobic coatings used in electrowetting. Most of these coatings come in the form of a fluoropolymer that exhibits a low surface energy. Teflon AF, CYTOP, Trichloro(octadecyl)silane (OTS), Fluoropel, and various plasma deposited fluoropolymers are of interest for the purpose of this research.

Prior electrowetting single-use valves utilized a PECVD deposited CHF3 fluoropolymer to achieve a hydrophobic surface. This method results in a conformal thin film building up over time in a low-pressure plasma environment. This method is good for applying a hydrophobic film to very small or delicate features. Similar to the PECVD approach is utilizing the passivation step of the Bosch process used for DRIE etching as mentioned earlier. This is also a low-pressure plasma deposition technique, but offers a different fluoropolymer chemistry.

Teflon is a very common hydrophobic film and also used extensively in electrowetting research. It can be sputtered, spin coated in solution, and spray coated in some forms. Given the need for a conformal and very thin layer of hydrophobic film needed for the microchannels in this work, sputtering was an attractive option. The samples are placed inside of a vacuum chamber attached to a rotating planetary stage. A Teflon sputter target is bombarded by ions of an argon plasma and Teflon particles are ejected from its surface onto the rotating stage below. Over time, this builds up a thin film of conformal Teflon coating on a device.

Also used in prior electrospray research is OTS silane thin films for hydrophobic layers. This deposition process is relatively simple if a thin film and not a monolayer (single molecule thick layer) is needed to conformally coat a surface. The device is cleaned thoroughly, and placed inside of a vacuum chamber along with a few drops of OTS solution on a clean glass slide. The chamber is evacuated and left to sit until

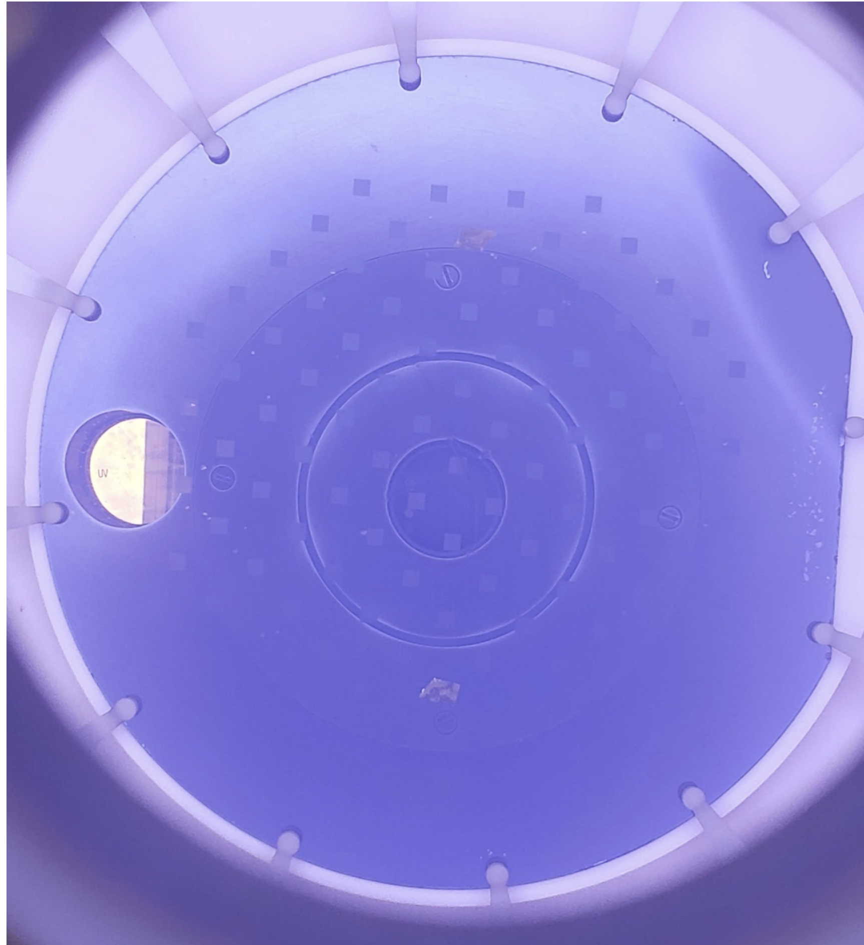

Figure 5-21: Depositing a thin film of hydrophobic C4F8 fluoropolymer using the passivation step of a DRIE etch process.

the droplets evaporate and disperse around the chamber over the course of at least 4 hours. Following the evaporation, the chamber is brought up to ambient pressure and the devices are allowed to dry for 24 hours to achieve a superhydrophobic surface.

Lastly, several commercially available fluoropolymer solutions such as CYTOP and Fluoropel are viable options for electrowetting hydrophobic coatings. Both of these fluoropolymer solutions are often spin coated and baked to achieve the desired low surface energy film. The typical process involves spin coated a small amount of the liquid fluoropolymer to conformally coat the surface, the baking the device in steps to fully dry out and cure the film. All of these hydrophobic coatings have their unique characteristics, therefore, each liquid to be tested in the electrowetting flow controller will be characterized via electrowetting for each of these hydrophobic films.

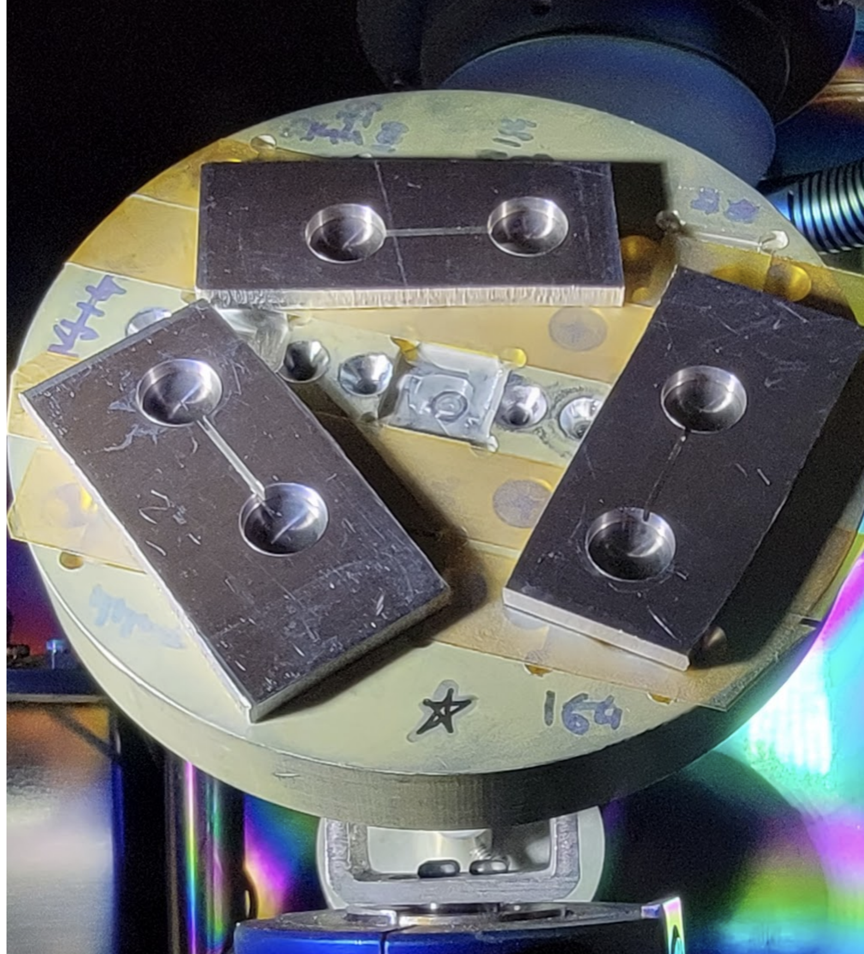

Figure 5-22: Aluminum microchannels inside of a sputter chamber attached to a rotating planetary stage.

5.3 Fabrication of the Experimental Electrowetting Flow Controllers

This section serves to outline the general fabrication steps used for the electrowetting flow controller as well as accompanying electrowetting test chips.

To characterize the hydrophobic coatings, several silicon wafers were thoroughly cleaned and thermally oxidized with approximately 500nm of silicon dioxide. This wafer was then diced into 10mm square dies. These individual chips were then either given an additional dielectric layer with parylene and/or given one of the aforementioned hydrophobic coating treatments.

The process used to fabricate the electrowetting contact angle measurement chips

Figure 5-23: Silicon microfluidic device after spin coating with a fluoropolymer solution.

Figure 5-24: Fabrication cross-section evolution of the electrowetting test chip.

for each dielectric/hydrophobic coating combination is as follows:

1. Clean silicon wafer
2. Grow 500nm thermal oxide
3. 1um Parylene C deposition (optional)
4. Hydrophobic coating or plasma treatment

For the electrowetting flow controller devices, the device design required curved channel features in addition to a conformal hydrophobic layer in the central region of an open microchannel. Both of which are difficult to achieve in the micron scale and in silicon.

While isotropic etching can provide sufficient rounding of silicon features in the microchannel, conformally coating a region of a capillary with a hydrophobic layer is quite the challenge. Sputtering with a planetary stage can achieve the conformal and region-specific aspects, but lacks the hydrophobic performance of spin-coated flouropolymers. The process to achieve this conformal and selective hydrophobic coating relied on the application of a thick layer of 10XT photoresist after the channel features were etched in silicon and coated with a dielectric. This photoresist is then masked using silicon pieces. The masked device is then flood exposed for approximately 20 minutes. Once developed, only the central region of the capillary channel is free of resist and clean down to the dielectric surface. A spin-coated fluoropolymer can then be applied to the central region without coating the ends of the channel or reservoirs, meaning only the central region of the capillary channel should resist wetting without electrowetting actuation. After baking the fluoropolymer, it is very resilient to solvents such as acetone, which can then be used to remove the photoresist mask. Once the resist is fully removed down to the dielectric, the device is left with a spin-coated fluoropolymer layer present only in the center of the channel as desired. A cross sectional evolution of this process is shown in Figure 5-25

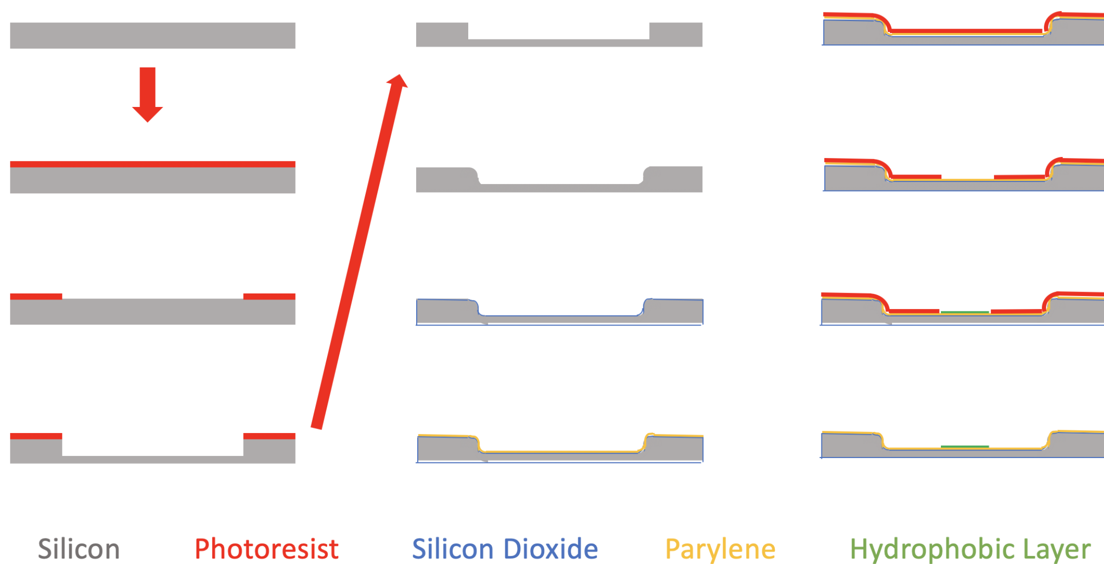

Figure 5-25: Fabrication cross-section evolution of the test electrowetting flow controller devices.

Figure 5-26: Left: masked device with photoresist coating atop the dielectric layer. Right: Post-development resist mask shows empty region where UV flood exposure occurred.

The process used to fabricate the electrowetting flow controller devices is as follows:

1. Clean silicon wafer
2. Coat with photoresist and bake
3. Expose microchannel/reservoir patterns
4. DRIE etch
5. strip photoresist
6. Isotropic SF6 plasma etch to round features
7. Piranha and HF to clean and strip native oxide layer
8. 500nm thermal oxidation growth

9. 1um Parylene C deposition
10. O2 plasma treatent of parylene
11. Spin thick photoresist and bake
12. Mask outer thirds of chips
13. Flood exposure 20 minutes
14. Develop
15. Deposit hydrophobic coating
16. Bake
17. Acetone and IPA clean to strip resist off of parylene
18. Dice wafer

Lastly, as a proof-of-concept cylindrical rail device, two polished aluminum cylindrical rods are cut to 2 inch lengths. They are then either anodized or coated in parylene similar to the silicon devices. The hydrophobic coating is then applied to a central region of each rod. The finished rods are then electrically connected via a small length of wire soldered to the end of each rod. This will provide the voltage necessary to spur electrowetting and the flow between the liquid reservoir and filter paper, just like in the silicon microchannel devices.

THIS PAGE INTENTIONALLY LEFT BLANK

Chapter 6

A Monodisperse Thruster Emitter Material

6.1 Material Formulation

A single thruster emitter tip is only capable of emitting approximately 0.5 micro-amps of current, therefore, a typical thruster multiplexes 500 tips to form an emitter array that emits current greater than 100 micro-amps. There exists a geometric condition, that will be discussed further later in this work, for these many emitter tips that, when satisfied, favors the formation of negative pressure ionic liquid menisci between emitter tips that wants to propagate up the tips towards the extractor. This phenomenon is referred to as "emitter flooding" and is effectively irreversible during thruster operation, however, if the tips were be cylindrical and aspect ratio were controllable, this effect could be more controllable.

Tip geometry also plays a crucial role in the emission characteristics and overall thruster performance. The angle of the ion beam, if intercepted by the extractor grid, can slowly erode the grid surface over time and even deposit liquid on it in the form of neutral from fragmentation that can also build up and short the extractor-tip gap. Tip height and sharpness variation also contribute to different start-up voltages for each tip, and can contribute to non-uniform ion emission currents across the thruster.

All of these failure modes and thruster performance issues have a common root in

the material of the emitter itself. To date, no porous emitter material has been made of truly uniform particles (monodisperse). This means that every thruster emitter is likely to have tip geometries that differ across the 480 tips that make up each emitter array leading to the aforementioned performance and lifetime issues. In Figure 6-1, the current uniformity was measured on an emitter array made of sintered borosilicate shards, with a pore size range of 1 to 10 micron. This study was able to take a look at the issues with non uniform current emission and their reliance on emitter material uniformity as well as tip geometry.

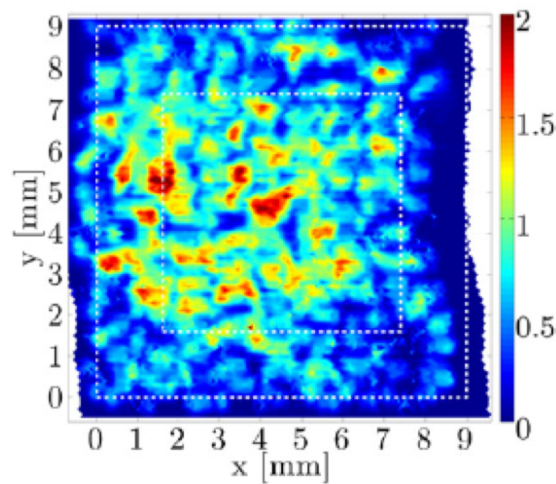

Figure 6-1: Current emission heat map from an electrospray emitter array. Note certain tips emit more ion current than others. [45]

A methodology used in the manufacturing of aerogels and other materials reliant on colloidal silica mixtures serves as a useful baseline. The goal of creating a porous silica emitter material to address these non-uniformities was set. A porosity between 40 and 60 percent as well as pore sizes around 1 micron are desired for this new material, as ion emission has been reliably seen with past emitters of similar value ranges. By combining silica nanoparticles with a UV-curable resin solution and strategically sintering, a new monodisperse emitter material is created, characterized, and integrated into several thrusters and fired to see the impact on performance. An added benefit of using spherical nanoparticles is the natural negative-pressure that should remain on the spheres' surface for any liquid contact angle above zero. The following

sections detail the derivation of this process and the resulting material created by it.

6.1.1 Coloidal Silica Solution

Previous work in the Space Propulsion Lab [1], investigated the use of coloidal silica solutions and the use of press forming and casting to form a porous silica green to then be sintered into a porous emitter material. While the post-sintered results were promising, the frequency of voids, and fractures of the chips suggested a variation in the chip formation would be needed.

6.1.2 UV Curable Resin Solution

To facilitate a monodisperse porous emitter material, uniform nanoparticle particle distribution is necessary. The nanoparticle (in this case nanosphere) powder used to achieve a monodisperse emitter chip was monodisperse silica, with spheres of a mean diameter of 1.5 micrometer. Additionally, a UV-curable resin base was also identified as necessary to be usable in both casting and printing applications. A commercially-supplied photoactive base resin (Genesis High Load Development Resin Base, Tethon 3D) formed the polymer matrix in which these particles were trapped during casting. A silane coupling agent (KH560, analytically pure, Energy Chemical, China) was also utilized to modify the surface of the silica particles to enable better adhesion to the resin polymer matrix. To formulate a photoactive, monodisperse nanoparticle resin, the silica particles were first modified to include hydrophobic surface structures. Xing et al. had success using KH560 in a 5 percent dilute solution with ethanol, where the coupling agent was measured to 2 percent powder weight [20]. For this work, the ethanol was doubled to enable more complete coating of the particle surfaces. An appropriate amount of silica was then incorporated and the solution was placed in an ultrasonic vibration environment at 60°C for one hour. This step ensures adequate coating of the particles and evaporates excess ethanol. Additional experimentation showed that the addition of KH560 was also necessary for maintaining the low viscosity needed for casting. The modified silica was then mixed to eliminate clumps

and incorporated into the base resin at a 75 percent mass fraction. Finally, a three to five-hour ball milling process was used to complete the silica's integration into the polymer matrix. As this resin is photoactive, additional care was taken to shield the solution from any ambient UV light. While degassing would be advantageous to eliminate bubbles (and any possible material voids they would create during sintering), doing so in a vacuum chamber appeared to greatly increase the viscosity, making this method infeasible.

6.2 Material Molding

A positive mold was designed using SolidWorks and 3D printed using a FormLabs® Form 2 SLA printer. According to thruster specifications, the final chip dimensions must be 1 cm square, with a depth of 1 mm. However, to account for the 15 percent shrinkage that occurs during firing, these values were re-scaled accordingly. The wells were set to be 1.15 cm square, with a depth of 2 mm. Increased thickness was also necessary to reduce warping as the cured chips dried, with extra material removed during a polishing phase. The mold was designed to produce 12 wells, enabling a casting batch size of 12 chips.

A negative mold was then made using polydimethylsiloxane (PDMS), which is UV-transparent. The PDMS was first mixed and degassed in a vacuum chamber, and then poured into the positive mold. It was degassed once more to remove any remaining bubbles. The mold was left to cure at ambient conditions for 24 hours. Although heat can aid in the curing process, this was found to warp the plastic and cause deformation in the PDMS. The final mold was carefully removed following the curing process. It is shown in Fig. 6-2.

Casting was performed by pipetting the milled resin mixture into the mold. The wells were generally overfilled to help prevent the introduction of air during the capping process. Once filled, UV-transparent sapphire glass slides were placed on the mold to eliminate the meniscus over each well and create a flat chip surface. This was done carefully, first touching the long edge of the slide against the mold and then

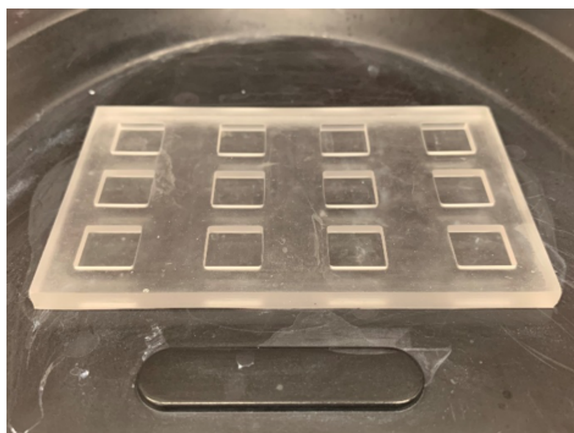

Figure 6-2: PDMS mold with 12 emitter chip wells.

slowly lowering the other until a seal was made. Thus, bubbles would not get trapped within the wells.

Without disturbing the resin, the mold was placed within a generic UV curing station. The chips were cured for 10 minutes, with the mold flipped halfway through to ensure even exposure. Although the resin solidifies fairly quickly when exposed to ultraviolet light, this precautionary step encouraged the bottom of the chips to adequately cure. Following the 10 minutes, the chips were demolded from the PDMS. Generally, they would remain attached to the slides and would thus need to be carefully separated with a razor blade. Any excess resin attached to the chips would then be cut away. Immediately after curing, they would be placed in deionized water to prevent warping, which occurs as they dry.

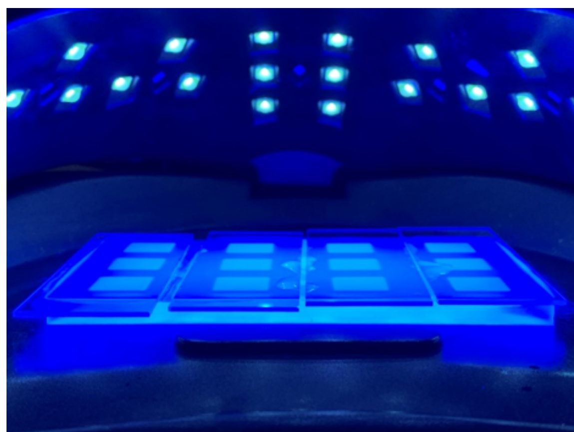

Figure 6-3: Curing chip greens under UV light source

When demolded, the chips are still wet with a residue from the resin (shown in 6-4), perhaps containing unevaporated volatiles. This liquid dries quickly, leaving behind surface imperfections. Adding the chips to water limits some of these flaws, however an ultrasonic bathing step was necessary to improve quality. The chips were placed in an ultrasonic bath of deionized water at room temperature for 30 seconds to remove residual material. Longer times were avoided to prevent the formation of microfractures in the chips.

Figure 6-4: Cured chip greens prior to sintering.

Prior to firing, the chips were left to dry at ambient conditions. This step caused some warping, though the impact was reduced by the chips' thickness. The post-firing polishing process smoothed out both sides such that any warping was nonetheless eliminated. To prevent deformation altogether, one approach was to press the chips between pieces of porous Teflon as they dried. This enabled the water to evaporate while constraining the chips in a flat orientation. However, because polishing was still necessary to reach the final desired thickness, the pressing approach was not used.

6.3 Material Sintering

Firing is a high-temperature treatment that allows the chip body, or powder compact, to transform into a rigid and solid material. Sintering is the corresponding thermal process occurring in the material that allows contacting particles to bond into a solid

object [21]. In this research, the firing schedule was modeled after the FormLabs® Ceramic Resin Firing Schedule [22].

In stage 1, the chips are heated to a burnout temperature of 240°C, where the polymer matrix is vaporized. The duration of the burnout hold in stage 2 is proportional to the thickness of the chips. Namely, the thickness in mm corresponds to the duration in hours. For these chips, a 120 minute burnout hold was selected. Stages 3 and 4 conclude the burnout phase at a slightly elevated temperature to ensure no remaining resin is left. Next, the chips are heated to a maximum sintering temperature during stage 5, where the individual nanosphere particles fuse together. One area of interest is how sintering temperature and duration affect chip strength and porosity. While strength is crucial, a more porous material can attain better electrospray efficiencies. For this work, a range of temperatures was selected and the resulting material properties were studied. The chips were normally held at their sintering temperature for only 5 minutes during stage 6, before cooling back down in stages 7 and 8. FormLabs® recommends parts be cooled at a rate of 2°C per minute from 900°C to around room temperature to avoid cracking and additional slumping [22]. This profile is shown in Fig.6-5 and summarized in Fig. 6-6.

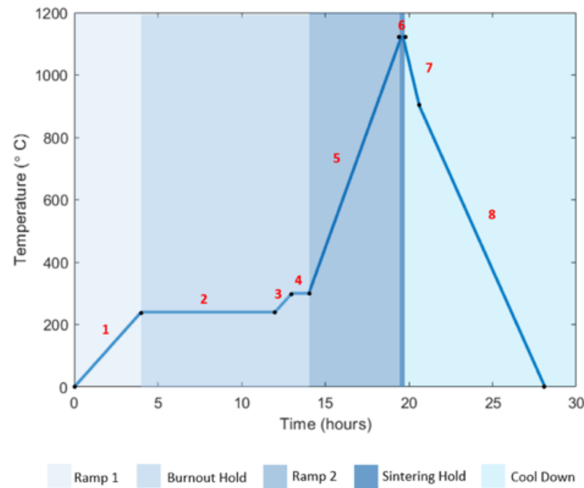

Figure 6-5: Sintering temperature profile.

Chips were placed on a platinum sheet during firing to prevent them from sintering to the furnace's ceramic surface. While there are certainly cheaper alternative

Stage	Total Time (min)	Time to Temperature (min)	Temperature (°C)	Phase
0	0	0	0	Ramp 1
1	240	240	240	
2	360	*120	240	Burnout Hold
3	420	60	300	
4	480	60	300	
5	772	292	1150	Ramp 2
6	777	5	1150	Sintering Hold
7	817	40	900	Cool Down
8	1267	450	0	

Figure 6-6: Sintering temperature ramp rates and hold times.

methods to avoid this, platinum has the benefit of a very high melting point and excellent chemical resistance in case any of the resin ingredients were to cause issue. The layout of the chips in the furnace is shown in figure 6-7.

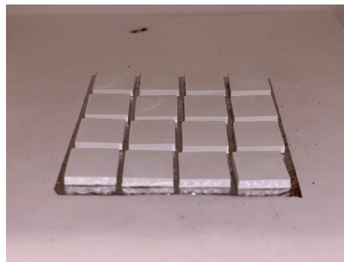

Figure 6-7: Chips greens in the sintering furnace atop a platinum sheet to avoid reactions with furnace walls.

6.4 Material Thruster Integration

To mount the sintered emitter chips onto a thruster frame, they first had to be polished to approximately 1 mm in thickness. After several trial polishing steps, it was determined that a fine grit diamond lapping film would provide smooth surface finish useful for laser ablation of emitter tips as well as Vickers hardness testing on non-thruster samples. Using 9 micron, 3 micron, and 1 micron diamond lapping films with de-ionized water, the chips are polished by hand prior to being mounted on the thruster frame. The chip-frame pair is then ready for tips to be laser ablated.

Chapter 7

Experimental Methods

7.1 Flow Controller

In order to characterize the performance of the electrowetting flow controller, several tests are needed. Namely, contact angle measurements, capillary wetting measurements, and filming of the flow dynamics and expected segmentation of the liquid filament in the device during operation.

7.1.1 Experimental Testing Set-up

There are many hydrophobic coatings to first characterize in order to pick the coating that gives the most usable wetting and non-wetting contact angle range during electrowetting. Contact angle data is collected for a variety of liquids (water, water/IPA, water/glycerol, EMI-IM, and EMI-BF4) via a standard horizontal-plane measurement set-up. A long working distance microscope is placed in plane with a silicon-silicon dioxide test chip coated with the desired hydrophobic surface layer. A 2.5 microliter droplet of liquid is placed on the hydrophobic surface, and a small electrode wire is placed into the droplet but not touching the chip surface. The resting contact angle is then photographed using the digital microscope. Then, in 10 Volt DC increments, the voltage from a 120VDC power supply is ramped up and the contact angle is photographed with each step up to 120VDC and back down to 0VDC. Following this

sweep, the voltage is then switched from 0VDC to 120VDV cyclically to measure and photograph any degradation in the hydrophobic properties over multiple actuations. To further prevent any large spikes in current from a short-circuit, the devices are grounded through a one Megaohm resistor. With the contact angle ranges for all

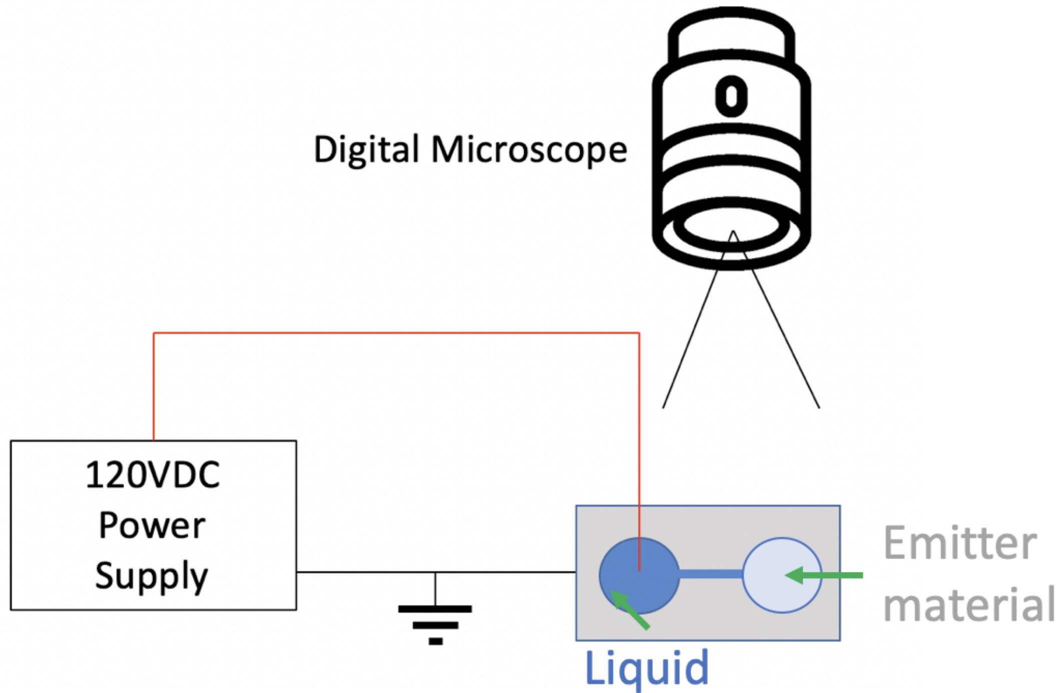

Figure 7-1: Experimental diagram for filming electrowetting flow control devices.

liquids and hydrophobic coatings known, the microchannel devices are then tested. To compare wetting dynamics of the open microchannels with the Modified Lucas Washburn (MLW) approach, a single reservoir device with an open microchannel of a particular aspect ratio, dielectric, and hydrophobic coating is placed into a Teflon jig with electrical contacts alongside the chip. The liquid of choice is loaded into the open reservoir with a micropipette and a small wire electrode is again placed into the liquid in the reservoir without touching the chip surface. A Keyence VHX digital microscope is used to film the wetting (or lack thereof) as voltage is applied to the liquid in the reservoir at 50 frames per second. The time stamped footage will correlate meniscus location and time that can then be plotted against the MLW prediction.

With spontaneous capillary flow wetting data collected, a second set of test devices with a reservoir on either end of the channel and a hydrophobic coating localized only in the central region of the channel are then tested. The second reservoir can be coated or not coated with hydrophobic coatings and can also include a porous emitter material piece to act as the "thruster" in the fluid system. Again the chips are placed in a Teflon jig beneath the VHX microscope. Liquid is placed in one reservoir and is subjected to voltage to drive wetting to other side of the channel. Once the second reservoir/emitter material piece is saturated, voltage will be removed to film the desired liquid breakup and segmentation in the channel where the hydrophobic region is located.

For the cylindrical device, the same power source is used, but instead of the VHX microscope, a horizontally mounted digital microscope is used to film the vertical progression of the liquid along the capillary rail. The cylinders are mounted into two optical stages to accurately control and measure the separation of the cylinders.

7.1.2 Voltage Control and Data Logging

Voltage control for these tests is supplied by a 120VDC power supply with 0.01 VDC resolution and operated in the current limited mode. A time-stamped video of the power supply voltage readout is collected and correlated to the time-stamp in the microscope footage in order to mark exactly when and what voltage is applied to the device.

7.2 Monodisperse Emitter Thrusters

7.2.1 Vickers Hardness Testing

Preliminary estimates of porosity, SEM imaging, and Vickers Hardness testing are used to characterize each batch of chips to ensure batch-to-batch precision. Porosity is estimated by first measuring the chips using calipers and weighing them on a precision scale. This weight is used to compare to expected weight of a chip of the

same volume that is solid amorphous SiO2. The air fraction of the chip volume is the porosity percentage.

SEM imaging of cleaved chips is used to inspect nanoparticle packing density and sintering effects. These images also provide an approximate measurement of pore size throughout the chip. Vickers Hardness testing utilizes a Struers DuraScan Vickers hardness testing machine to approximate material hardness. A square pointed tip is plunged into the material at a set weight-force and the resulting imprint dimensions are used to calculate the Vickers hardness according to Equation 1.

$$HV = \frac{F}{A} \approxeq \frac{1.8544F}{d^2} \tag{7.1}$$

Where F is the force applied to the square pointed tip in kgf, A is the area of the resulting imprint (also captured by d^2 if the imprint is truly square.) Resulting values are written as Hardness-HV-load force or 40HV0.3, for example. A porous glass or ceramic can range anywhere from 3-100HV0.3 or more if sintered long enough and/or hot enough. 0.3 kgf is used for potentially brittle materials such as ceramics so as not to cause a fracture in the sample.

7.2.2 SEM Tip Profiling

In order to ascertain the end-result tip profile uniformity in the monodisperse emitter material, a scanning electron microscope is used to measure tip height and radius of curvature following laser ablation. 10 emitter tips across the array are measured and their dimensions logged for each emitter made. This data is useful for laser ablation process development in addition to understanding the effects of material uniformity on the resulting tip produced by the laser.

7.2.3 Emission Current-Voltage Characterization

To characterize the general start-up and steady-state operation of the electrospray thruster, the current and voltage relation is crucial. In order to "condition" the thruster, a slow ramp to 300V and hold is followed by a second ramp to 700V and a

final hold. After this hold, a ramp up in voltage is continued until current emission is observed. This point is referred to as "start-up" voltage and is well correlated to the sharpness of the emitter tips; blunt tips tend to have larger start-up voltage than sharper tips. Once stable emission is achieved (typically around 1000VDC), the same process is applied to condition the thruster in the opposite polarity emitting the opposite charge of ion. Once both polarities have demonstrated emission, a square wave voltage profile is used to switch between polarities to decrease any beam transients associated with initial start-up.

Once the thruster is fully conditioned, the thruster current-voltage or IV data is collected by applying a triangle wave voltage profile starting at 0 volts and ramping up until the intercepted current (ions and or droplets that are intercepted by the extractor grid electrode) is no longer negligible, typically around 10% the emitted beam current. This data is collected in both the positive and negative polarity to understand thruster start-up, steady-state emitted and intercepted current, and the voltage value at which interception is non-negligible.

A typical I-V curve is shown in the figure below:

7.2.4 Time-of-Flight Mass Spectrometry

Time of flight or TOF mass spectrometery is a standard test to characterize the beam composition of an electrospray thruster. The principal behind TOF spectroscopy is that for a given accelerating electrostatic potential, the accelerated species of differing charge-mass ratios will be emitted with distinct velocities, according to the following equations:

$$v_i = \sqrt{\frac{2q_i}{m_i}V} \tag{7.2}$$

$$t_{arrival} = \frac{L}{v_i} \tag{7.3}$$

where L is the distance between the thruster emitter and the time-of-flight detector, q_i is the ion species charge, m_i is the mass of the ion species, and V is the

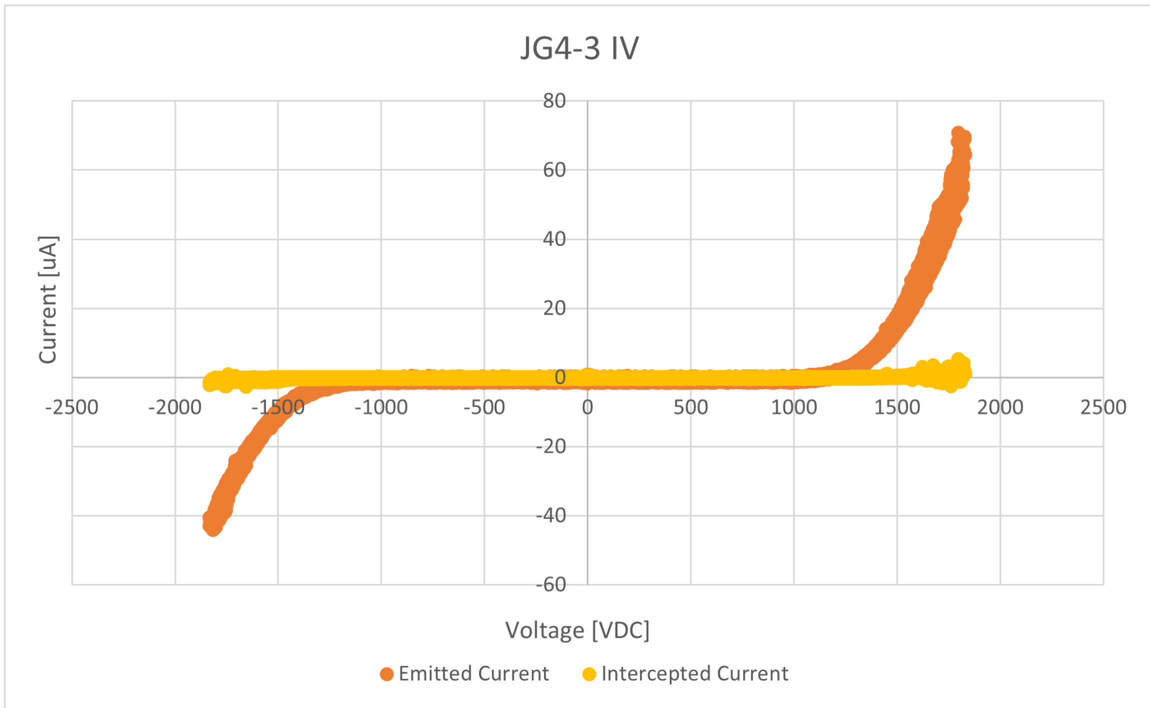

Figure 7-2: Emitted and intercepted current vs applied voltage for an ion electrospray thruster.

applied electrostatic potential. By actuating the detector gate (as opposed to the thruster which is a fluid system and thus has transients) and collecting data via a high-sampling rate oscilloscope, distinct time steps can be observed corresponding to emitted monomers, dimers, and even trimers confirming or denying the operation of the thruster in the desired "ionic mode" as compared to a droplet emission mode or mix of both. An example of this captured data from an electrospray thruster is shown in the following figure:

The combination of TOF and IV data is sufficient to compare new emitter material thruster performance to prior emitter materials.

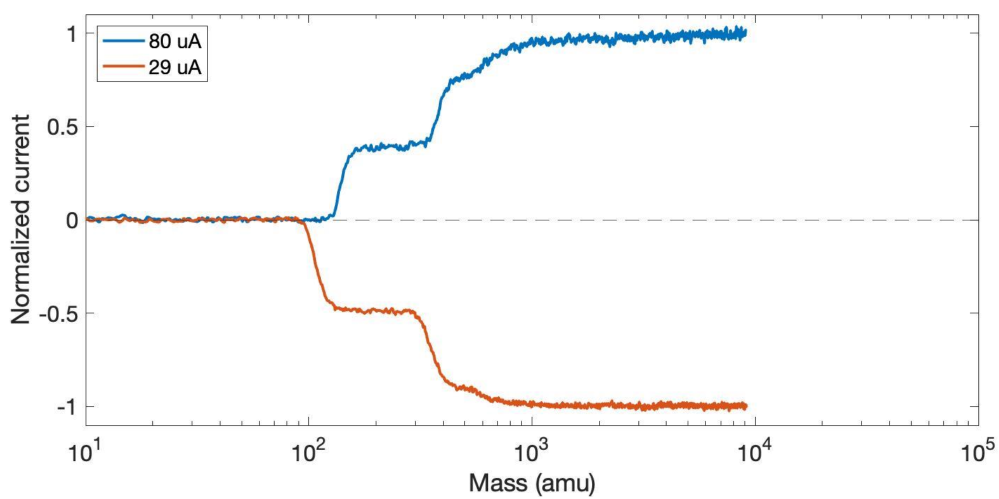

Figure 7-3: Time of flight data for electrospray ion emission. Note the stair steps corresponding to monomer and dimer species with sloped regions showing fragmented species.

THIS PAGE INTENTIONALLY LEFT BLANK

Chapter 8

Data Analysis Methods

8.1 Flow Controller Data Analysis

To properly characterize the fluid dynamics of the electrowetting flow controller, contact angle data is necessary. Image data taken from the contact angle test setup is analyzed using imageJ and a plugin called "LB-ADSA drop analysis" to accurately measure the contact angle between the liquid and hydrophobic layer interface. This is done for every non-electrowetting and electrowetting test including for every voltage step recorded. A sample image analysis in imageJ is shown in figure 8-1.

Following the analysis of contact angle measurement data, flow rate measurements for liquids in a variety of open microchannels is conducted. Several microchannel geometries are tested but all are filmed during operation with a Keyence VHX digital microscope that can imprint length scale on images. These length scales are paired with the 50 frame-per-second high-resolution video footage of the fluid dynamics at play with the devices. Flow rates are measured according to time-stamp and length-scale correlation. The relatively large contact angles mean the fluid front does not extend drastically beyond the top of the channel as it progresses down it, making velocity measurements a relatively simple procedure.

When the devices are switched off and the contact angle is restored to a hydrophobic state, the liquid is expected to deplete to either end of the channel and eventually segment. This phenomenon is captured via angled filming of the open channels. This

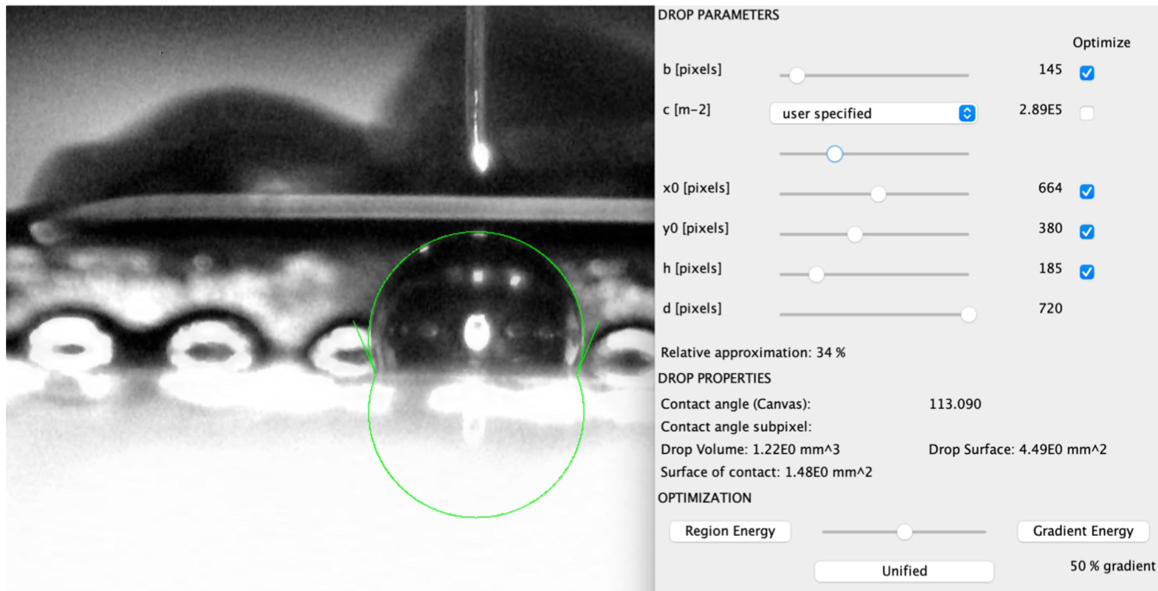

Figure 8-1: Contact angle measurement for a droplet of water on a hydrophobic surface.

analysis is simply a binary, either the liquid segments as desired or does not.

When emitter materials are introduced to the end of the channel to act as a wettable media, similar to the thruster use-case, a small volume of loose nanoparticle silica spheres are added to the reservoir along with the chip. This enables the analysis of reversed flow conditions in some open microchannel geometries. Once the liquid reaches the reservoir with the emitter chip and nanoparticles, any reversed flow will bring the reflective nanoparticles back along the channel to its origin reservoir. Similar to aforementioned flow rate analysis, this motion is analyzed with time stamp and length scale legends to determine flow velocity and mass flow rate of the liquid in the device.

8.2 Monodisperse Emitter Data Analysis

Given the goal of the new monodisperse emitter material is focused on improving tip uniformity, start-up voltage, and demonstrating sustained operation in pure ionic mode emission, little data analysis needs to be done on Time-of-Flight data and I-V curve data to show improvements in these areas. Tip uniformity is characterized

via SEM imaging of several tips in an "X" pattern across each emitter chip after laser ablation. The tip height and radius of curvature is logged along with variation across the measured group. Height variation is intended to be less that 10 micron and radius variation less than 5 micron with an average tip radius of less than 10 micron. These values would put the new material in a position to outperform current materials on tip uniformity and sharpness. Vickers hardness data is processed is simply applying the Vicker's hardness equation to the known indentation dimensions of the imprinting tip along with applied force to derive overall Vicker's hardness. For the thruster firing data, TOF data will be post-processed according the methods outlined in Appendix B. This analysis will provide derived values for mass flow rate, thrust, and specific impulse for each thruster's TOF dataset. TOF curve steps will be noted corresponding to monomer, dimer, and possibly trimer molecular species. Lifetime testing is very straightforward data to analyze, the thruster must operate continuously in both polarities for as long as possible. The lifetime test is ended as soon as thruster can no longer fire reliably or runs out of propellant, whichever comes first. The continuous operational time is logged as the "lifetime" value for a particular thruster.

THIS PAGE INTENTIONALLY LEFT BLANK

Chapter 9

Experimental Results

9.1 Electrowetting Flow Controller

The experimental results for the electrowetting flow controller are broken into the three primary experiments run: electrowetting contact angle results, initial SCF wetting of open channel, and flow segmentation and tracking results.

Electrowetting Contact Angle Ranges of Liquids

Contact angle ranges were collected for a variety of liquids: DI water, 80% DI Water/20% IPA by volume, EMI-IM, and EMI-BF4. EMI-IM and EMI-BF4 were of the most interest given they are usable propellants for electrospray applications. Knowing that the contact angle must be hydrophobic without electrowetting and hydrophilic with electrowetting, a variety of hydrophobic coatings were also tested. These coatings included: a thin PECVD deposited fluoropolymer, a spin-coated and thermally baked fluoropolymer, and an evaporated trichlorosilane coating. The following plots show the contact angle achieved in these tests.

Figure 9-1 shows the first test of electrowetting on a previously used silane coating process. The hydrophobicity of the 2.5 microliter droplet of DI water on the coating is excellent at first, but the contact angle pins and no angle is restored when voltage is removed. This behavior was seen in multiple droplet tests. While trichlorosilane monolayers have been used successfully in the past for reversible wetting, they are

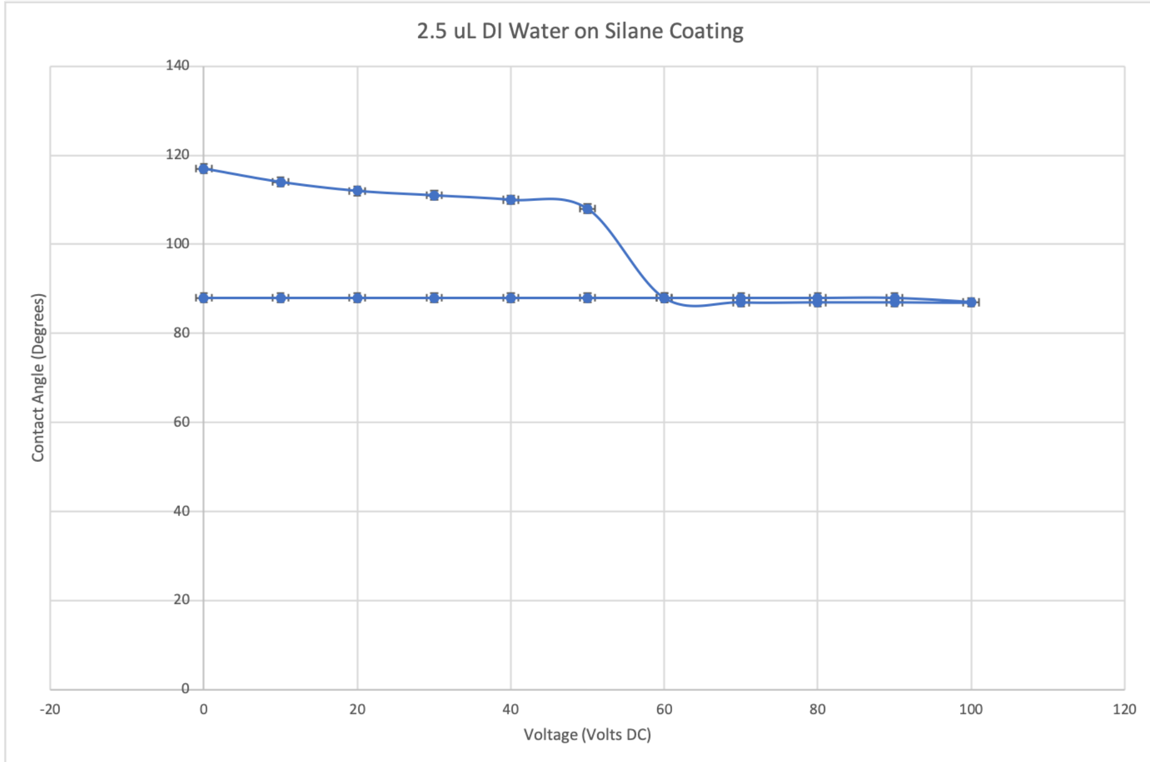

Figure 9-1: Preliminary electrowetting curve for DI water on the trichlorosilane hydrophobic treatment on a silicon-silicon dioxide chip. Note the large hysteresis in the angle restoration.

very thin and delicate. It is possible the evaporation process used here did not have a thorough enough cleaning step and the layer failed to adhere completely throughout the surface.

Figure 9-2 shows an additional electrowetting test performed on a PECVD deposited fluoropolymer (CHF3) also used in previous electrospray component tests. Unlike the silane treatment, CHF3 showed a reversible electrowetting contact angle change for DI water with angles above and below the 90 degree wetting threshold. However, when EMI-BF4 was applied to this coating, that angle range decreased (as expected given the lower surface tension) to a value below 90 degrees with very little change over voltages. This narrow range, coupled with the discovery that this fluoropolymer layer did not withstand multiple electrowetting cycles (angle chane decays to zero after a couple voltage application cycles), meant that CHF3 PECVD hydrophobic layers were not sufficient for the flow control application.

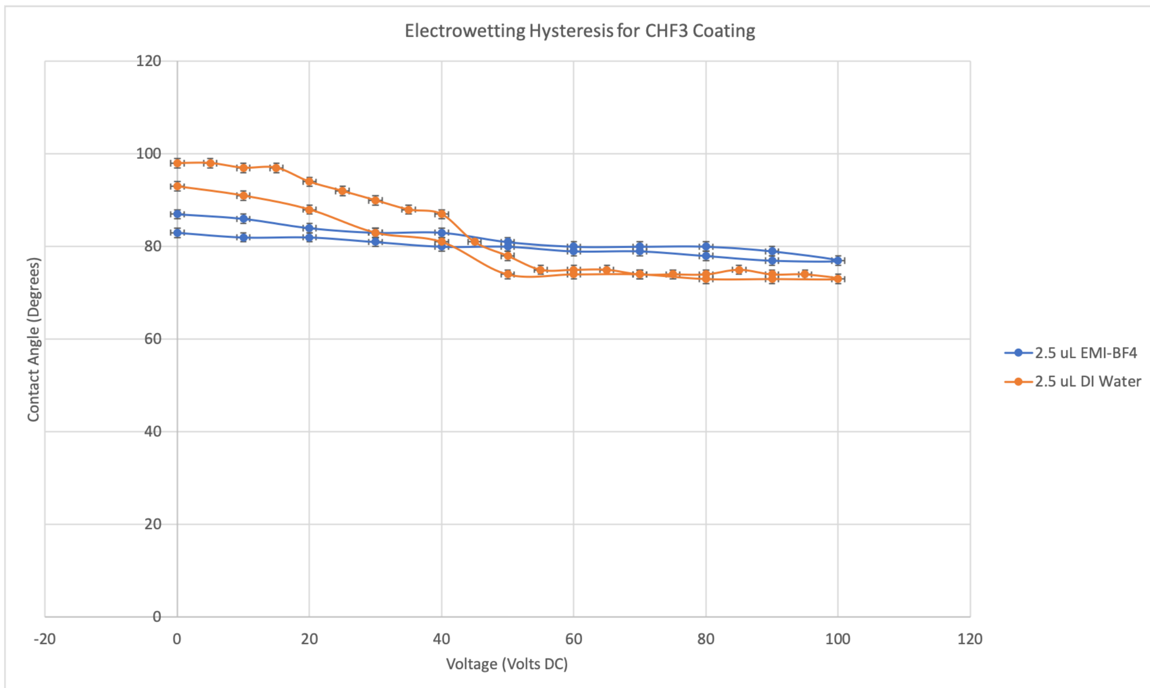

Figure 9-2: Electrowetting curve for DI water and EMI-BF4 on a PECVD fluoropolymer hydrophobic coating. Note the narrow range of angle change for EMI-BF4.

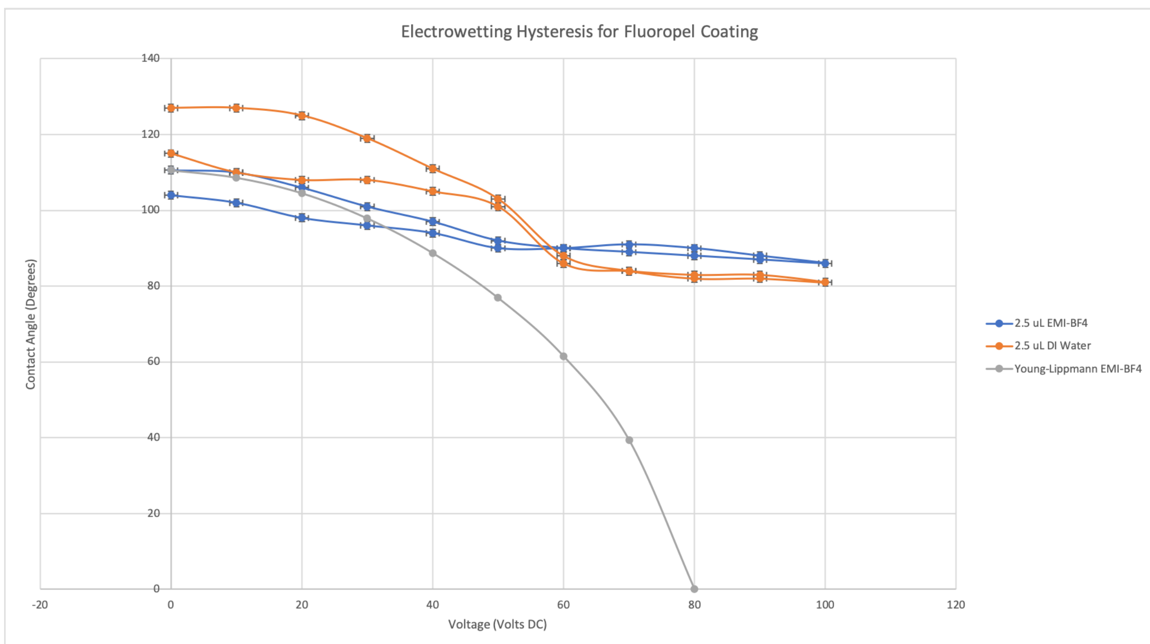

Figure 9-3: Electrowetting curve for droplets of DI water and EMI-BF4 on a silicon-silicon dioxide chip coated with Fluoropel. Note the addition of the Young-Lippman curve to the EMI-BF4 data to show where saturation begins.

Figure 9-3 shows the electrowetting contact angle change for DI water and EMI-BF4 on a commercially available Fluoropel hydrophobic coating. This coating provided a much more desirable and repeatable contact angle range for both water and EMI-BF4. Even with 6 degrees of angle hysteresis after the initial voltage application with EMI-BF4, the contact angle range provided both a non-wetting and wetting contact angle of 104 degrees and 85 degrees. This coating was then tested again with both EMI-BF4 and EMI-IM droplets.

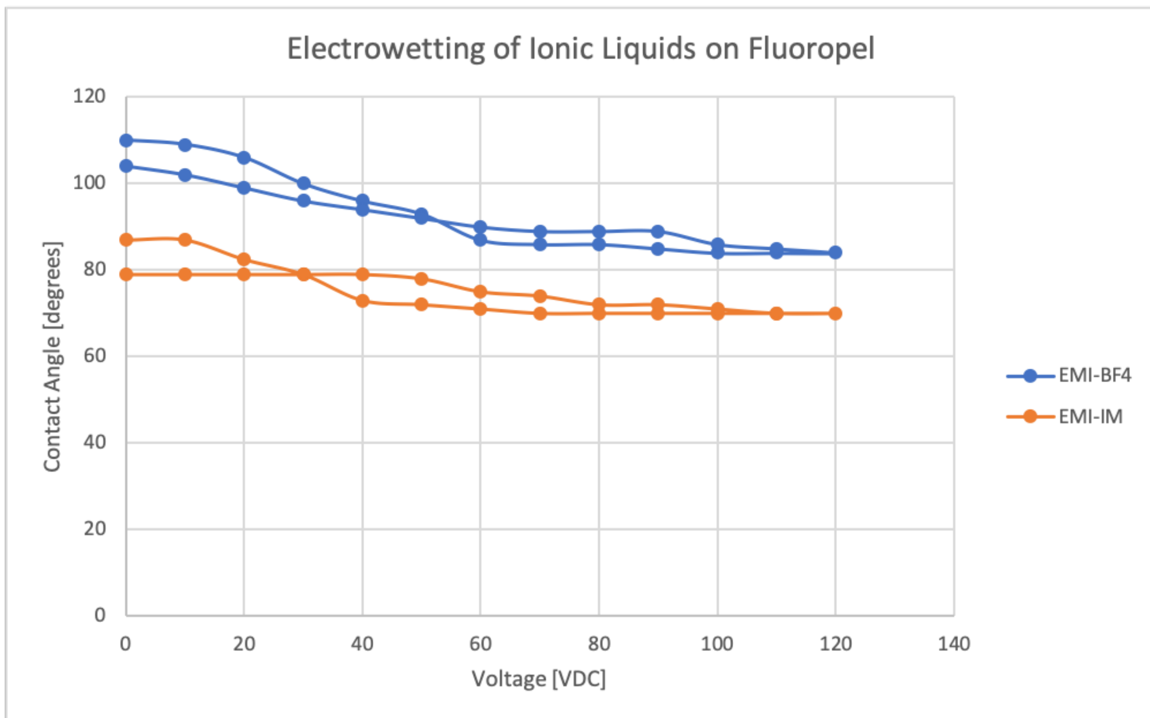

Figure 9-4: Electrowetting curve for droplets of EMI-BF4 and EMI-IM ionic liquids on a Fluoropel coated test chip.

Figure 9-4 shows the follow-on test of electrowetting contact angle behavior of EMI-IM and EMi-BF4 atop a Fluoropel hydrophobic coating. Given the lower surface tension of EMI-IM as compared to EMI-BF4, the contact angle is a bit lower to begin with, and the range of contact angle after initial hysteresis loss is only 80 degrees down to 70 degrees. This means that EMI-IM on fluoropel would not be able to provide a positive pressure morphology in the microchannel, at least not without very tight geometry controls. However, the higher surface tension EMI-BF4 does still maintain a viable range of 104 degrees down to 85 degrees. This 85 degree value, although

technically wetting, is a very small window to work within for the microchannel flow. Nonetheless, cyclic testing for both EMI-IM and EMI-BF4 ionic liquids on Fluoropel is conducted.

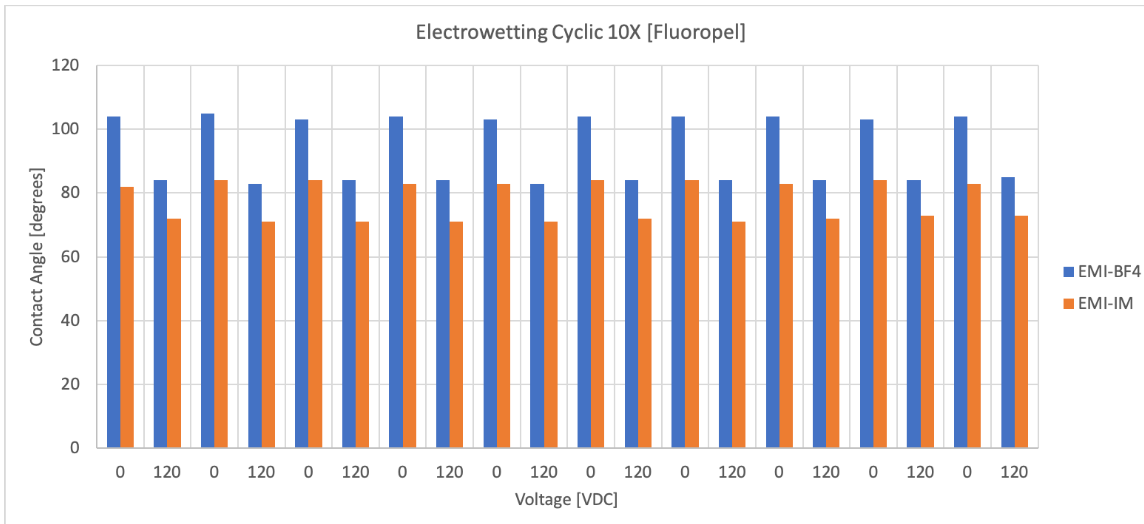

Figure 9-5: Cyclic electrowetting actuation of EMI-IM and EMI-BF4 droplets on Fluoropel. 120 VDC is applied and removed multiple times to measure any degradation in contact angle restoration.

Figure 9-5 shows the cyclic electrowetting testing of EMI-BF4 and EMI-IM droplets on Fluoropel. After the initial activation, where angle hysteresis is about 6 degrees, negligible angle loss occurred within 10 cycles. This is a promising result for the pairing of EMI-BF4 with Fluoropel. To further characterize this coating, a mixture of H2O and IPA (lower surface tension) as well as H2O and glycerol (higher surface tension) are also tested.

While the range of contact angles was decent for EMI-BF4 and water on Fluoropel, ideally the wetting angle would be a bit lower than 85 degrees to ensure wetting. It was, however, found that by lightly treating the fluoropel with an O2 plasma for 30 seconds decreased the contact angle range down to 76-98 degrees from 85-104 degrees for EMI-BF4 and down to 73-108 degrees from 81-115 degrees for water. This more desirable wetting range is shown in Figure 9-6.

Figure 9-7 shows the electrowetting curve for the mixture of H2O and IPA atop fluoropel. This test is primarily to gauge the contact angle range of a liquid with

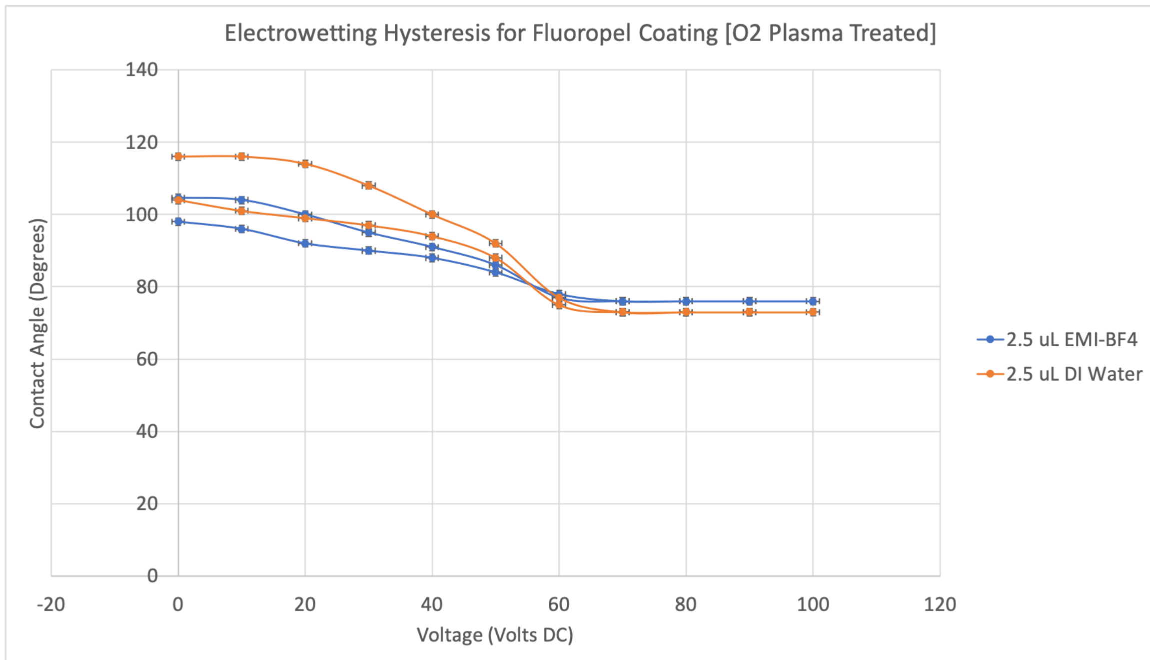

Figure 9-6: Electrowetting curve for EMI-BF4 and water atop an O2 plasma treated fluoropel hydrophobic coating.

lower surface tension and dynamic viscosity than EMI-BF4 for use in flow rate tests in the open microchannel devices. This mixture showed a repeatable range of contact angles between 95 degrees and 75 degrees.

Figure 9-8 shows the electrowetting curve for a mixture of 50% water with 50% Glycerol by volume on fluoropel. This test is also to gauge the contact angle range of a liquid with higher surface tension than EMI-BF4. This mixture showed a repeatable contact angle range between 113 degrees and 77 degrees after the initial actuation hysteresis.

Similar to the plasma treated fluoropel, a final hydrophobic coating to be tested was a plasma treated parylene C coating in the hopes of attained a lower wetting contact angle under electrowetting effect while keeping a non-wetting angle without voltage applied similar to the plasma treated Fluoropel.

Shown in figure 9-9 is the electrowetting curve for droplet of EMI-BF4 on a layer of parylene C treated by O2 plasma followed by SF6 plasma to enhance roughness and increase hydrophobicity. This treated parylene provided similar magnitude range of contact angle as fluoropel but with an overall lower value between 105 degrees and

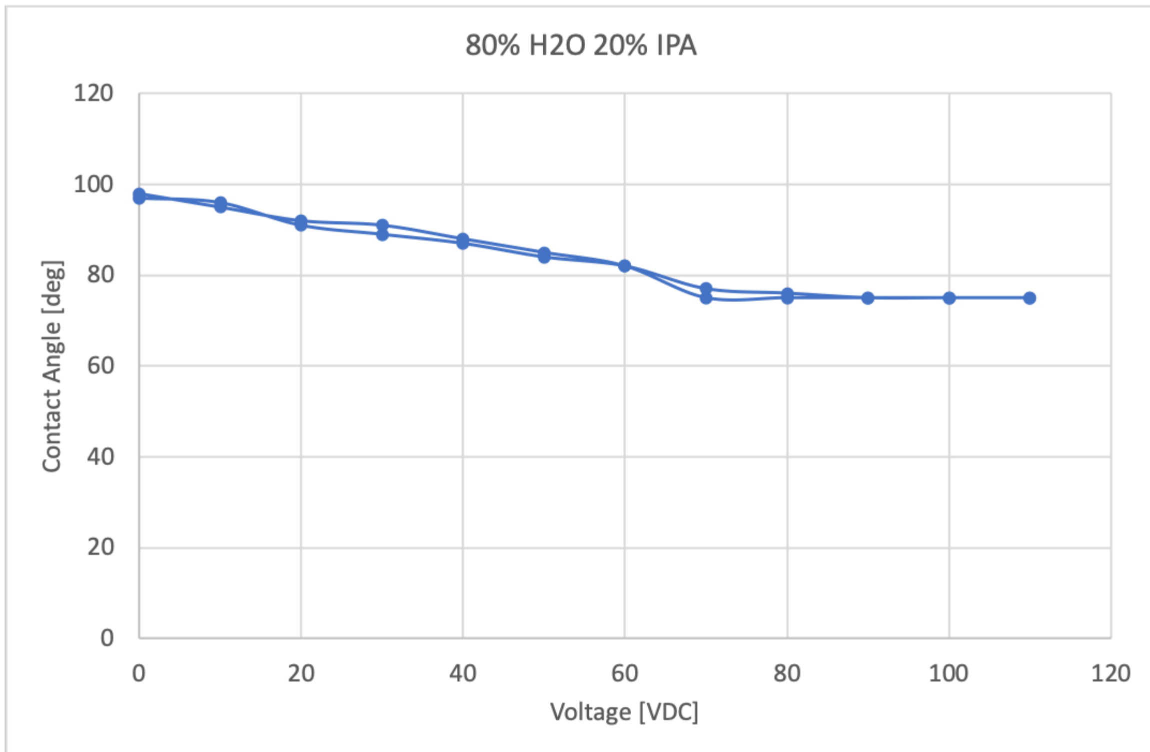

Figure 9-7: Electrowetting curve for a mixture of 80% water with 20% IPA by volume atop a fluoropel hydrophobic coating. Note the negligible angle hysteresis for this mixture.

77 degrees. This coating is also very promising when paired with EMI-BF4. However, Figure 9-10 shows that this coating has noticeable contact angle hysteresis with cyclic voltage application up to 10 times, meaning reversible control is unlikely with this coating, at least for any number of measurable cycles.

Following the many tests of hydrophobic coatings, O2 plasma treated Fluoropel provided the most desirable contact angle range for EMI-BF4 of 76 to 98 degrees within a 5 minute test window. This 5 minute window was chosen as to mitigate the effects of absorbed water on the measured contact angle change over time. In other studies [47], Fluoropel has shown good repeatability of contact angle modification via electrowetting within a few hundred cycles, but around 2000 cycles, the contact angle change decreases to the point where the contact angle with voltage applied is approximately the same as the contact angle without voltage applied. In order to ascertain the repeatability of contact angle modification atop the O2 plasma treated

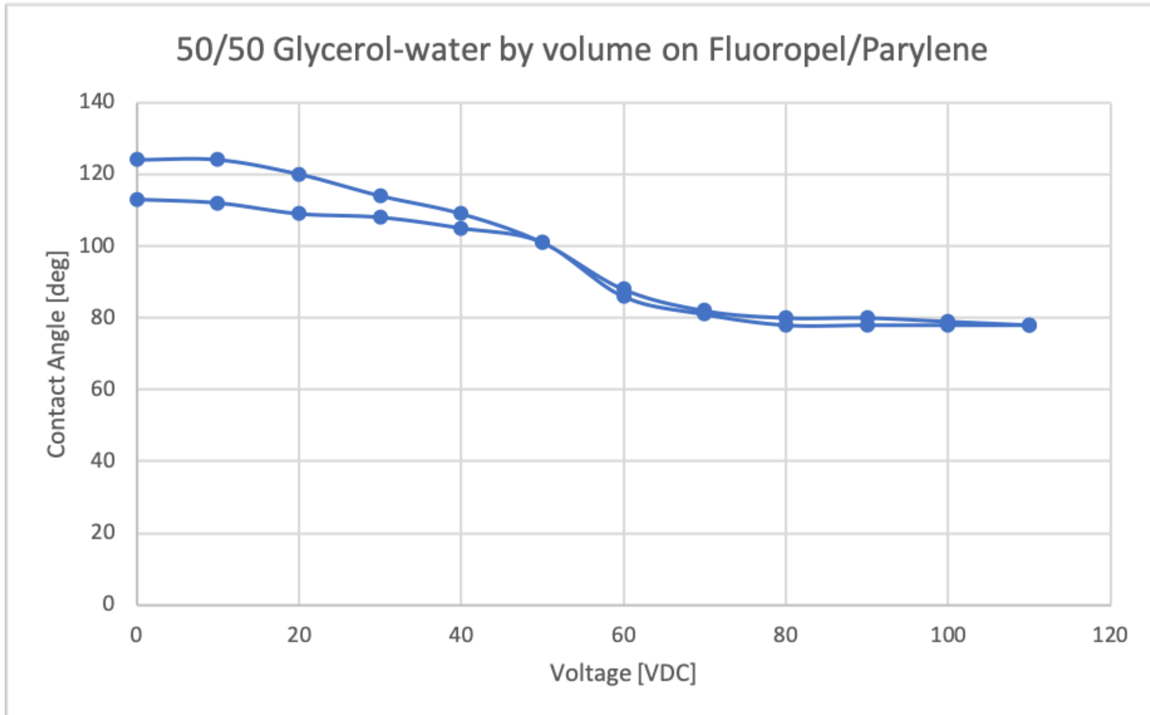

Figure 9-8: Electrowetting curve for a mixture of 50% water with 50% Glycerol by volume atop a fluoropel hydrophobic coating. Note the very similar range as pure water.

Fluoropel layer, a 100 cycle test was performed with a voltage off value of 0VDC and voltage on value of 120VDC. After 100 cycles of electrowetting of EMI-BF4 atop the plasma treated fluoropel layer, a maximum loss of overall contact angle modification value was found to be less than 2 degrees. This could also be attributable to ambient water absorption by EMI-BF4 over the course of the test. The cyclic test results are shown in Figure 9-11.

With the contact angle ranges for a variety of hydrophobic coatings known, these angles are used to analyze and design the necessary microchannel devices to enable flow control to a porous thruster emitter material. The most promising coating for all of the liquids is the parylene coating followed by spin-coating Fluoropel followed finally by a light oxygen plasma treatment to lower the hydrophobicity slightly. The next set of results demonstrate these best-case coatings applied to devices where wetting velocities are measured in channels as they are filled under the influence of electrowetting-induced capillary flow.

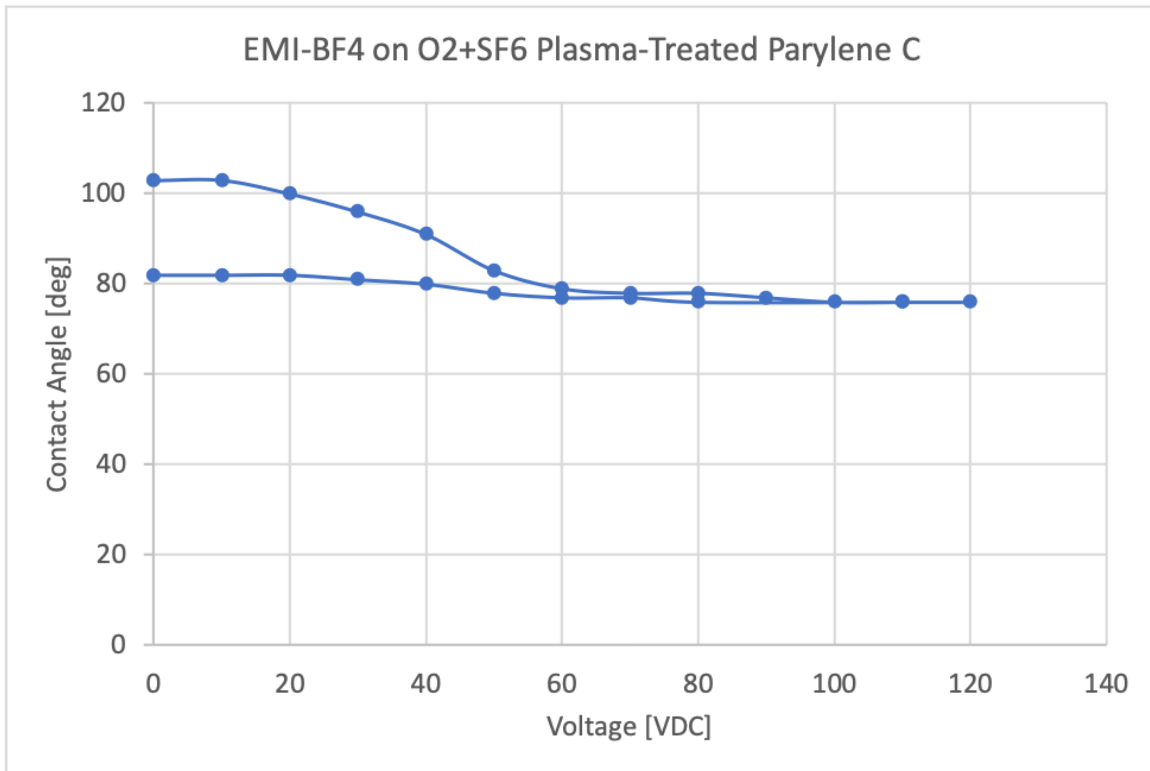

Figure 9-9: Electrowetting curve for EMI-BF4 on an O2 plasma and SF6 plasma treated parylene C hydrophobic layer.

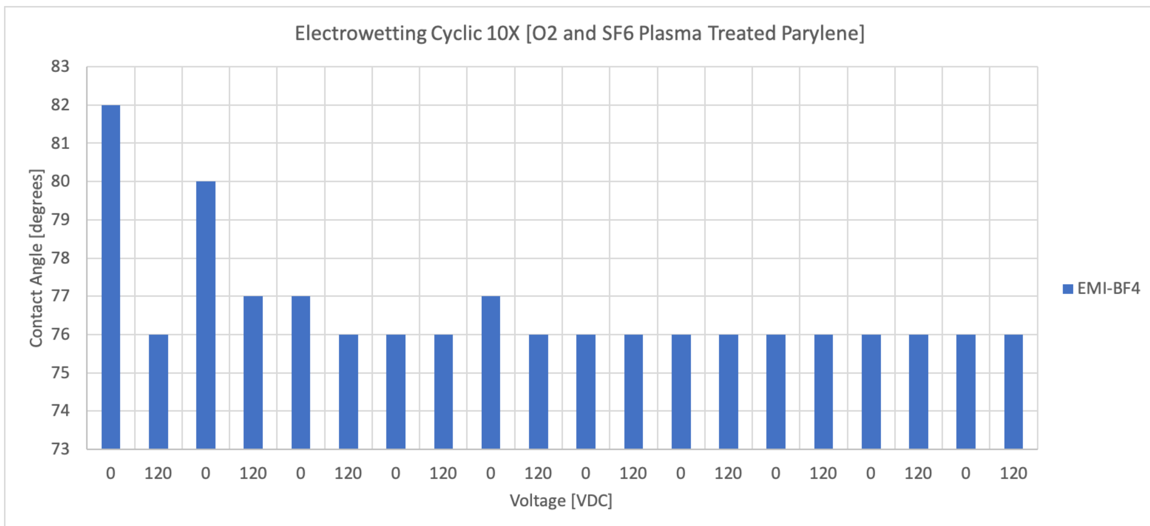

Figure 9-10: Cyclic electrowetting of O2 and SF6 plasma treated parylene coating with EMI-BF4.

Electrowetting-induced SCF in Open Microchannels

A series of test devices made in silicon and aluminum were put into the electrowetting jig and filled with a variety of liquids including EMI-BF4, EMI-IM, water, isopropyl

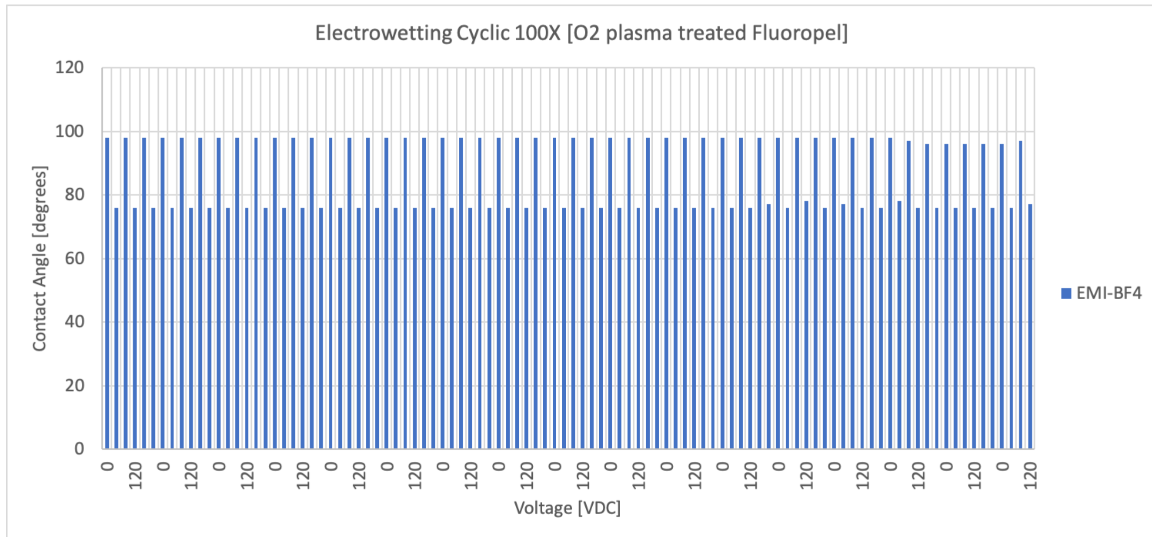

Figure 9-11: Cyclic electrowetting of O2 plasma treated Fluoropel coating with EMI-BF4.

alcohol, and glycerol. The first round of tests focused on channel geometry and hydrophobic coating pairings that would produce SCF wetting of the channel under the influence of electrowetting. The liquid wetting velocity down the channel was recorded and logged for successful device-liquid pairings. Figure 9-12 shows a silicon device with silicon dioxide and a PECVD CHF3 fluoropolymer as a hydrophobic dielectric undergoing SCF once 100 Volts of bias is applied to electrowet EMI-BF4 in the device's reservoir. This particular device was made prior to the implementation of the isotropic etch rounding step to avoid meniscus pinning along the edge of the channel and utilized the much less robust PECVD CHF3 fluoropolymer hydrophobic coating.

The aluminum-fabricated devices showed correlation with expected flow velocities from the MLW model [26] up to the point where the liquid reaches a suspected pinhole defect in the sputtered dielectric film, causing a short. Failure in the dielectric layers on these devices was the primary reason the remainder of the tests are in silicon devices with more robust conformal dielectric layers.

Figure 9-13 shows the liquid filament penetration distance vs. time for a mixture of 80% H2O and 20% IPA by volume. At a contact angle of approximately 75 degrees and with surface tension and dynamic viscosity values of 0.03 N/m and 0.00225 Pa s,

Figure 9-12: EMI-BF4 undergoing SCF into a plasma-treated fluoropel coated channel. Channel width is 100 micron and depth is approximately 300 micron. Note the clear meniscus pinning along the sharp ledge of this particular device.

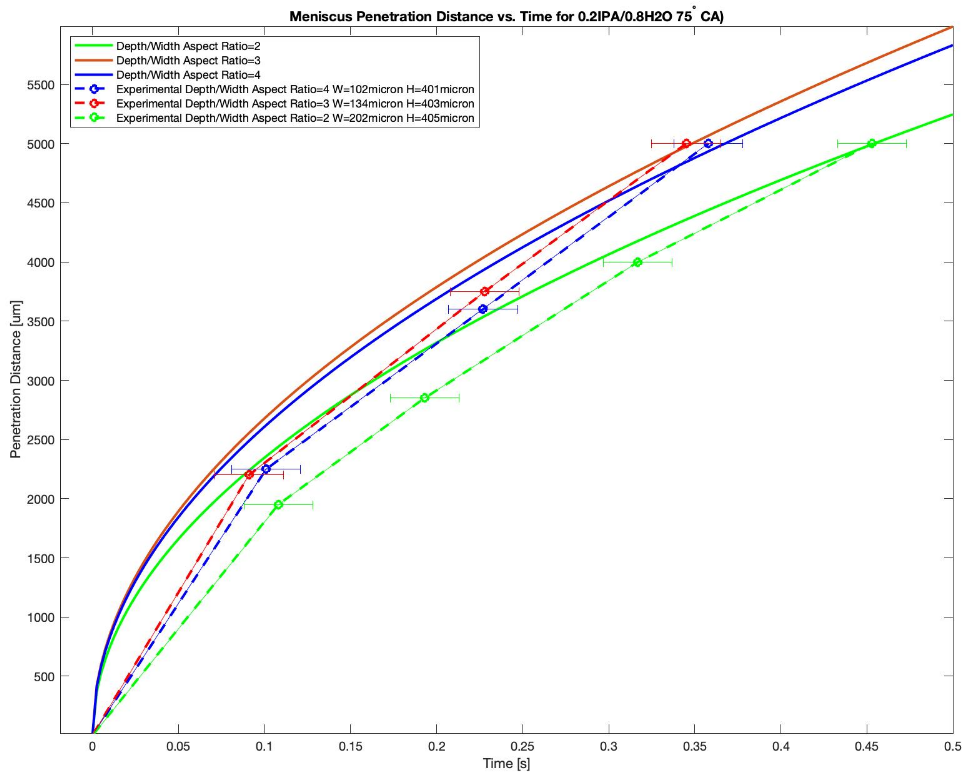

Figure 9-13: MLW approximation vs experimental test results of SCF wetting in open rectangular microchannels with a mixture of 80% H2O and 20% IPA by volume.

the motion observed under electrowetting at 100V correlated well with the expected dynamics estimated with the Modified Lucas Washburn approach. Given the low viscosity of the liquid, the motion, as expected, is quite fast. Thus, the error bars in this data set are limited by the frame rate of the video camera attached to the microscope (50 frames per second.) A minimum depth-to-width aspect ratio of 1.5 is required for this liquid to experience SCF in the open microchannel, and it is seen that all aspect ratio devices wetted as expected.

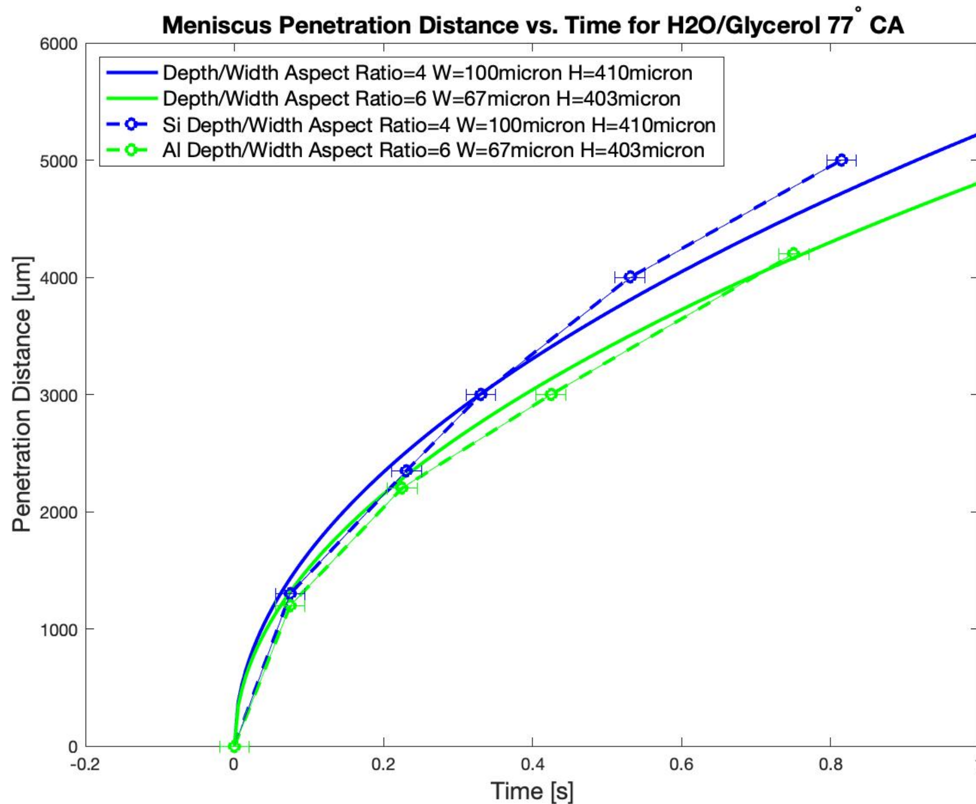

Figure 9-14: MLW approximation vs experimental test results of SCF wetting in open rectangular microchannels with a mixture of 50% H2O and 50% Glycerol by volume.

Figure 9-14 shows the liquid filament penetration distance vs. time for a mixture of 50% H2O and 50% Glycerol by volume. At a contact angle of approximately 77 degrees and with surface tension and dynamic viscosity values of 0.068 N/m and 0.01 Pa s, the motion observed under electrowetting at 100V also correlated well with the expected dynamics estimated by the Modified Lucas Washburn approach. Given

this mixture's much higher viscosity (and larger surface tension) than the H2O/IPA mixture, a slower liquid penetration velocity is seen (about double the time to reach 5mm as H2O/IPA). A minimum aspect ratio for this liquid to undergo SCF is about 2, however, this liquid was used in deeper channel (aspect ratio of 4 and 6) devices to highlight the effects of wall-drag in high-viscosity liquids.

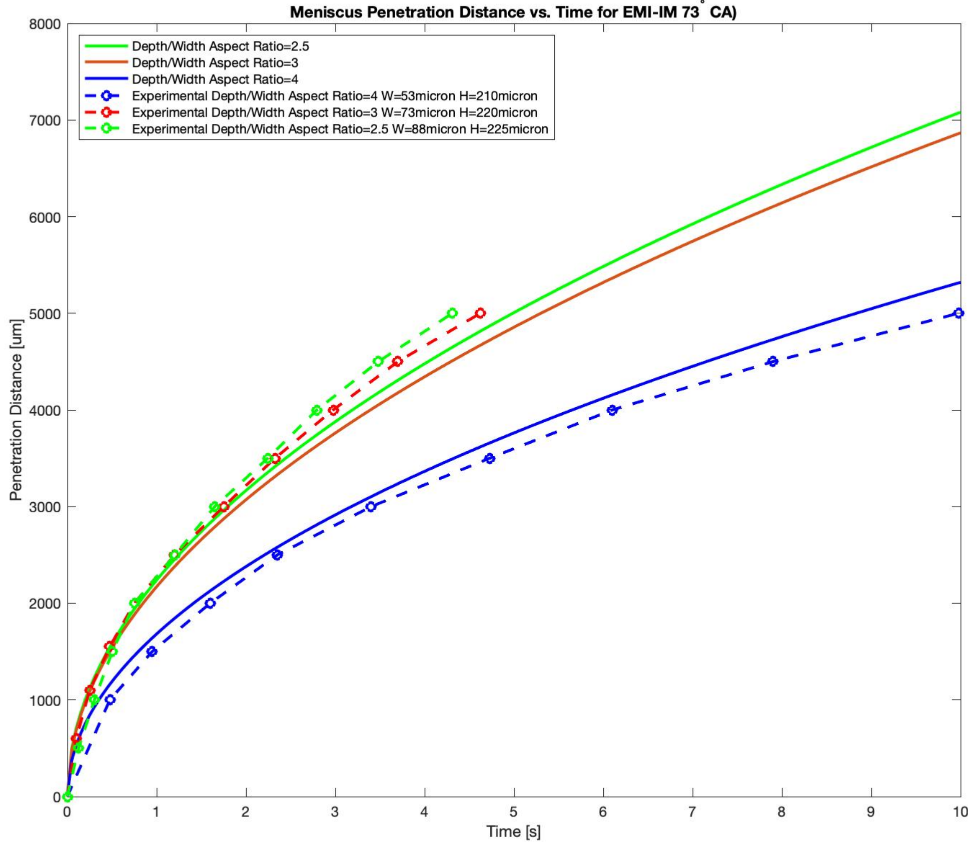

Figure 9-15: MLW approximation vs experimental test results of SCF wetting in open rectangular microchannels with EMI-IM.

Figure 9-15 shows the liquid filament penetration distance vs. time for EMI-IM. At a contact angle of approximately 73 degrees and with surface tension and dynamic viscosity values of 0.0381 N/m and 0.041 Pa s, the motion observed under electrowetting at 100V correlated well with the expected dynamics estimated with the Modified Lucas Washburn approach. Additionally, the minimum SCF criteria for EMI-IM contact angle ranges suggested an aspect ratio of 1.25 or higher would grant

wetting. This is in agreement with the fact that all tested channel aspect ratios (2.5, 3, and 4) wetted. However, given the contact angle range of EMI-IM on the most hydrophobic coating available falling below 90 degrees, this liquid is not tested further in this thesis work, as it would not be able to achieve a positive pressure meniscus with a contact angle above 90 degrees.

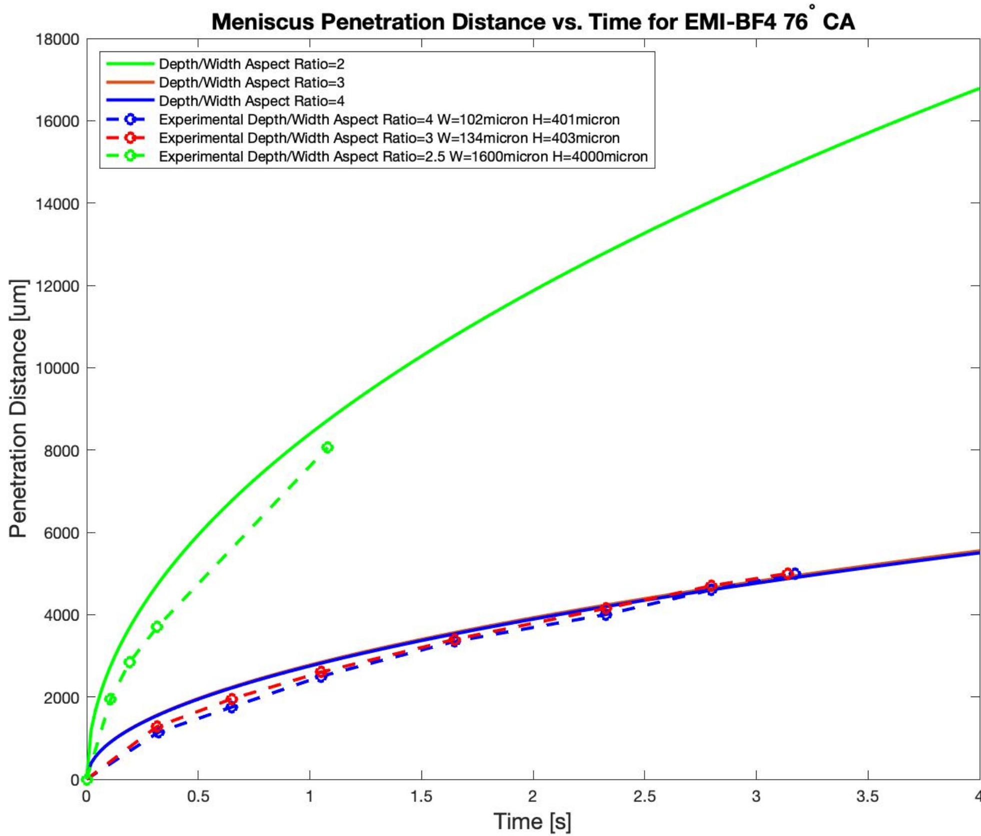

Figure 9-16: MLW approximation vs experimental test results of SCF wetting in open rectangular microchannels with EMI-BF4.

Figure 9-16 shows the liquid filament penetration distance vs. time for EMI-BF4 in a channel coated with Fluoropel and treated with O2 plasma. At a contact angle of approximately 76 degrees and with surface tension and dynamic viscosity values of 0.03 N/m and 0.0502 Pa s, the motion observed under electrowetting at 100V correlated well with the expected dynamics estimated with the Modified Lucas Washburn approach. EMI-BF4 has the most appealing contact angle range on Fluoropel for the

generation of both positive and negative pressure meniscus morphologies in rectangular grooves. However, it tends to absorb water in atmosphere, changing it's contact angle over time. In order to neglect these effects, the EMI-BF4 is desiccated for 30 minutes prior to every test in a device in a similar manner done for the contact angle measurements. Furthermore, tests using pure water are also conducted in order to find the minimum aspect ratio that works for both liquids reliably.

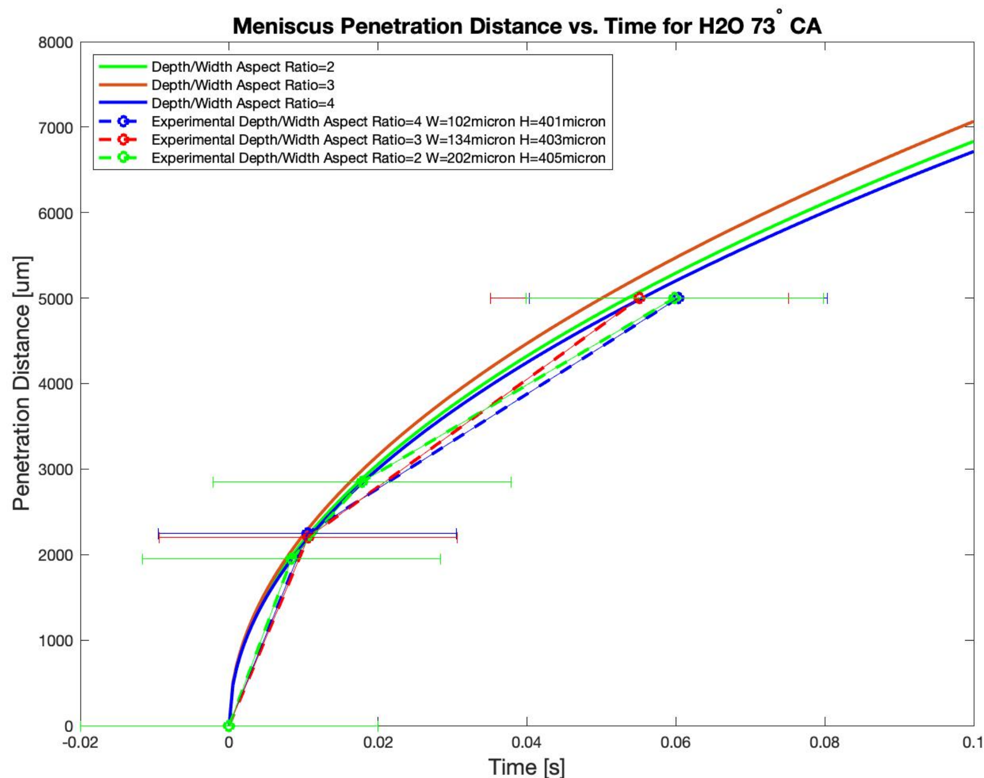

Figure 9-17: MLW approximation vs experimental test results of SCF wetting in open rectangular microchannels with H2O.

Lastly, Figure 9-17 shows the liquid filament penetration distance vs time for H2O also in a channel coated with Fluoropel and treated with O2 plasma. At a contact angle of approximately 73 degrees and with surface tension and dynamic viscosity values of 0.072 N/m and 0.001 Pa s, the motion observed under electrowetting at 100V correlated well with the expected dynamics estimated with the Modified Lucas Washburn approach, albeit with large error bars given the speed of the liquid in the channel captured on video. The few frames with distinguishable meniscus fronts

were logged and did correlate with the MLW model. The next set of tests focused on replicating the operational thruster boundary conditions. That is, a negligible pressure upstream liquid reservoir and a either a neutral pressure (non-firing) saturated porous emitter at the end of the microchannel or a negative pressure (firing) non-saturated porous emitter at the end of the microchannel. The goal of these tests is to demonstrate the capillary instability and segmentation of the liquid filament in the channel atop the hydrophobic coating.

Flow Stopping and Segmentation

Following the data collection on wetting in open microchannels for a variety of liquids, the two-reservoir devices are tested to simulate end conditions similar to a thruster. One reservoir is filled with a liquid just to the point where there is negligible curvature (neutral pressure in reservoir.) The other reservoir at the end of the channel has a piece of porous emitter material adhered via photoresist. This gives each device the chance to show flow dynamics when the porous material provides a negative pressure suction as well neutral pressure once the emitter material is saturated. Shown in Figures 9-18 and 9-19 are the two reservoir devices with a hydrophobic coating in a central region of the open microchannel.

For these tests, priority is on EMI-BF4 given it is actually used as an electrospray propellant unlike water. The device used for the following images has a depth-to-width aspect ratio of 4. Voltage is switched on at 100VDC to the electrode placed in the filled reservoir, liquid then wets the channel fully over the hydrophobic region in the same manner as prior tests. Once the liquid fully saturates the porous emitter, voltage is removed, restoring the hydrophobic contact angle of the liquid filament in the region with Fluoropel coating in the channel. This region of the filament begins to divit, eventually depleting the hydrophobic region completely of liquid, segmenting the filament between the reservoir and saturated porous emitter chip. The liquid then moves to either end of the channel, ready for re-application of voltage and restoration of the filament in the channel. This repeatable motion effectively confirm the hypothesized electrowetting flow control effect desired in open microchannel with

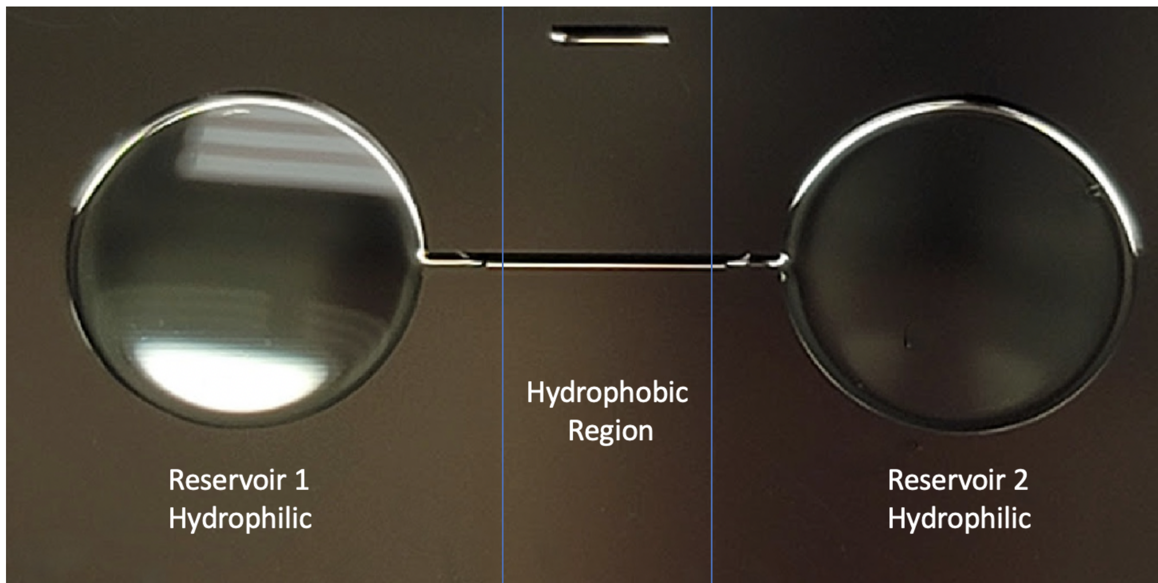

Figure 9-18: Two reservoir device with hydrophobic coating strip in middle, note that the liquid in the reservoirs stops at the hydrophobic region in the channel.

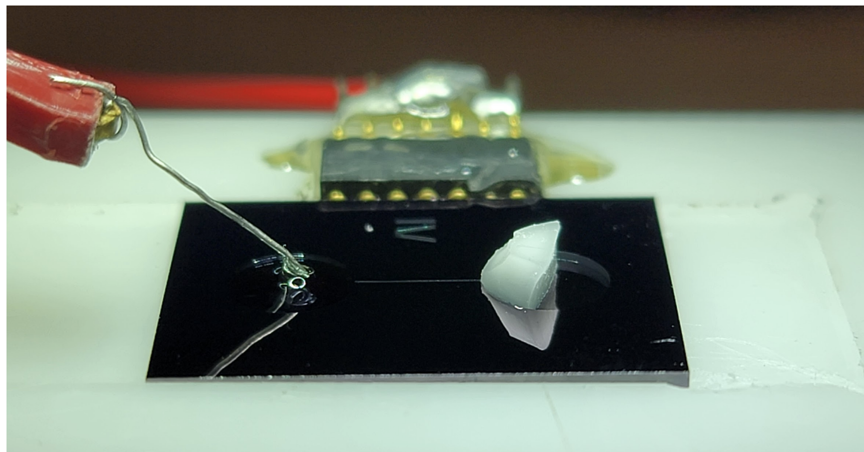

Figure 9-19: Two reservoir device with hydrophobic coating strip in middle and emitter material at end of channel.

sufficient rounding to avoid meniscus pinning.

The same device was then filmed at an angle to highlight the liquid filament diviting and segmentation. Once, voltage was removed, the central region of the liquid filament is clearly seen depleting and eventually causing the filament to segment and recede to the hydrophilic channel and reservoir regions. These angled images are shown in Figure 9-22.

Following ten test cycles with EMI-BF4 in the device, the device was cleaned of the

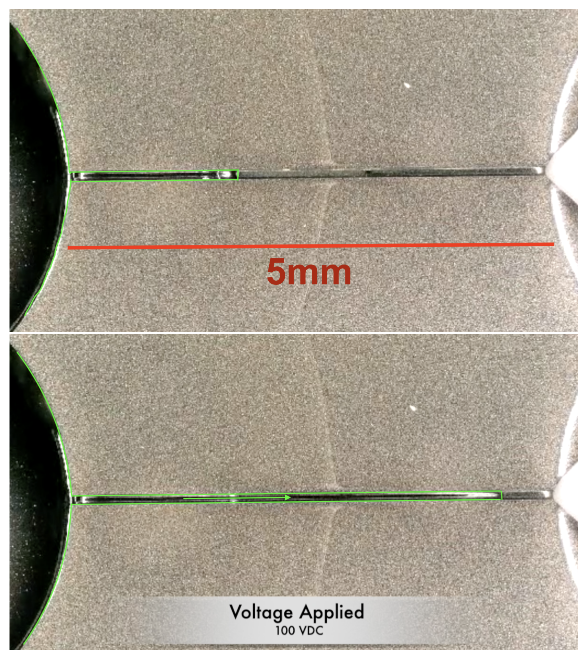

Figure 9-20: EMI-BF4 in a two reservoir device with hydrophobic coating strip in middle and emitter material at end of channel undergoing SCF via electrowetting.

ionic liquid and the reservoir was then filled with water. As with the EMI-BF4 tests, once voltage was applied, the channel wet almost instantly just as before given water has a higher surface tension and lower viscosity. Once the porous emitter material is fully saturated and the voltage to the device is removed, the hydrophobic contact angle is restored to the water filament in the central region of the channel, generating a divit in the filament that eventually depletes the center of the filament until it segments between the two reservoirs, just as with EMI-BF4, albeit much faster. This segmentation is shown in Figure 9-23.

With the segmentation of the liquid filament in the open microchannel strictly controlled by the wettability of the central region of the channel, an electrowetting on-off-on valve is demonstrated with dynamics quite similar to those predicted by earlier analysis. It is demonstrated that so long as the electrowetting region of the channel provides a contact angle above and below the 90 degree Cassie angle needed for wetting and de-wetting, the device enables and stops flow to the porous material at the end of the channel. The channel rounding was sufficient to prevent pinning and realize a change in pressure within the channel that allowed for sustained flow

Figure 9-21: Liquid filament depletion and segmentation without application of voltage to device.

and segmentation with only modification of the liquid-wall contact angle via electrowetting. The effects of this rounding are even more pronounced in the simplified cylindrical device set up.

Given the contact angle upper limit of wetting for the two cylinder configuration is 75 degrees, even the plasma-treated fluoropel did not provide a low enough contact angle for EMI-BF4 to wet the rods, however, DI water on this treated surface reliably provided a contact angle range between 73 and 108 degrees as mentioned earlier. The cylinders coated with parylene and a region of fluoropel, were slightly submerged into a large dish filled with DI water. The cylinders were then adjusted to a pitch of 2.06 cylinder radii, which is below the SCF wetting threshold. The water immediately wetted up the cylinder capillary rail up to the hydrophobic region in similar fashion

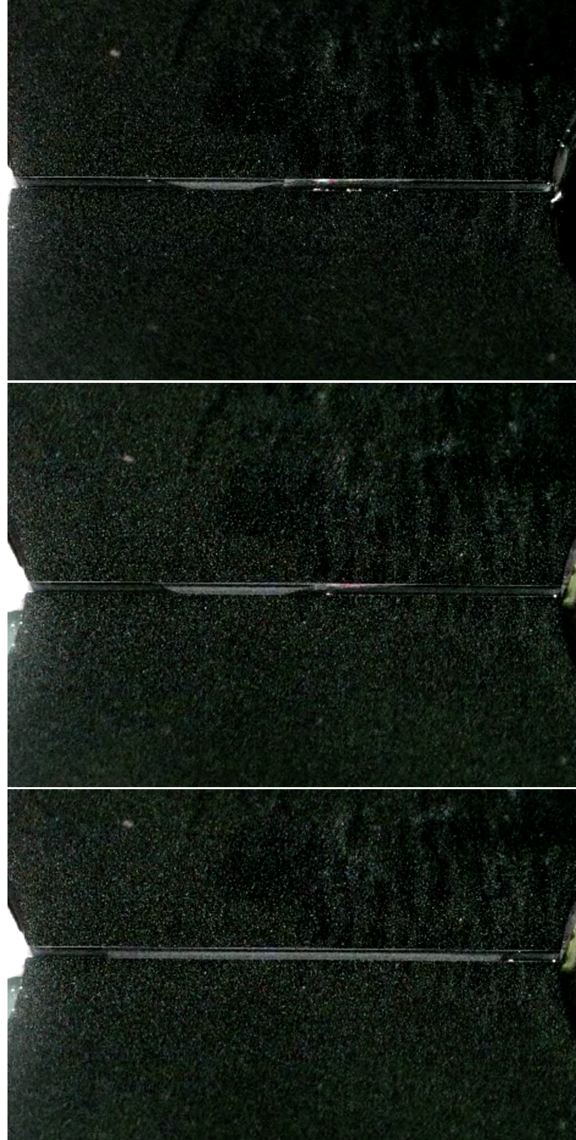

Figure 9-22: EMI-BF4 filament depletion and segmentation shown at an angle. The divit is the light gray region in the center of the channel where the hydrophobic coating is. The EMI-BF4 filled reservoir is at the right and saturated emitter material reservoir is at the left.

to the silicon devices. This is shown in Figure 9-24.

Once voltage is applied between the rails and the liquid reservoir, the electrowetting effect decreases the contact angle to below the SCF wetting threshold, allowing for liquid to then flow past the fluoropel region and into the filter paper.

Shown in Figure 9-25 is the liquid continuing to flow into the filter paper while the voltage is applied to the device.

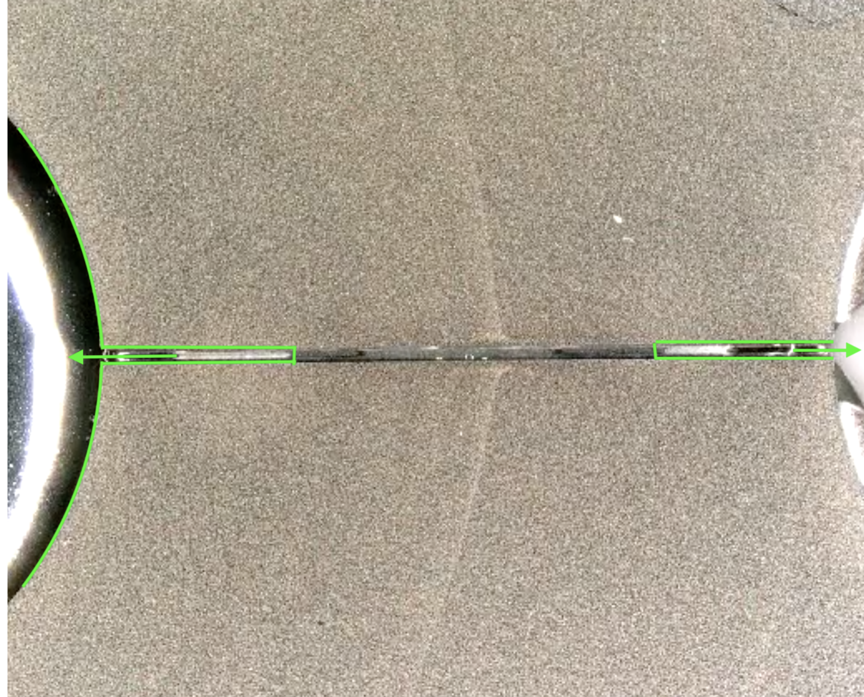

Figure 9-23: Water filament depletion and segmentation without application of voltage to device.

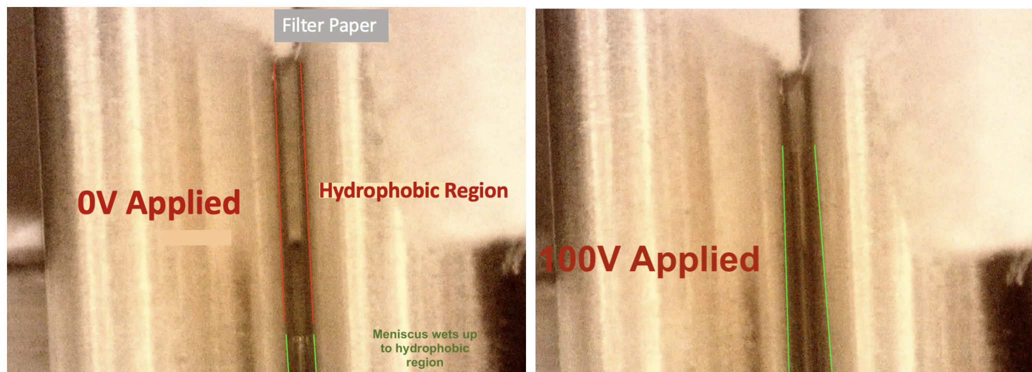

Figure 9-24: DI water wets up to the central hydrophobic strip on a cylindrical capillary electrowetting device. Once the 100VDC is applied between the two cylinders and the liquid reservoir, the contact angle drops below the wetting threshold for the hydrophobic region, due to electrowetting, and flow along the rail toward the filter paper.

The liquid will continue to flow into the filter paper so long as it is not fully saturated. Once the voltage is removed from the device, just like the silicon devices, the liquid contact angle restores to a non-wetting value that causes a capillary instability, segmenting the liquid between the two ends of the capillary rail. This is further

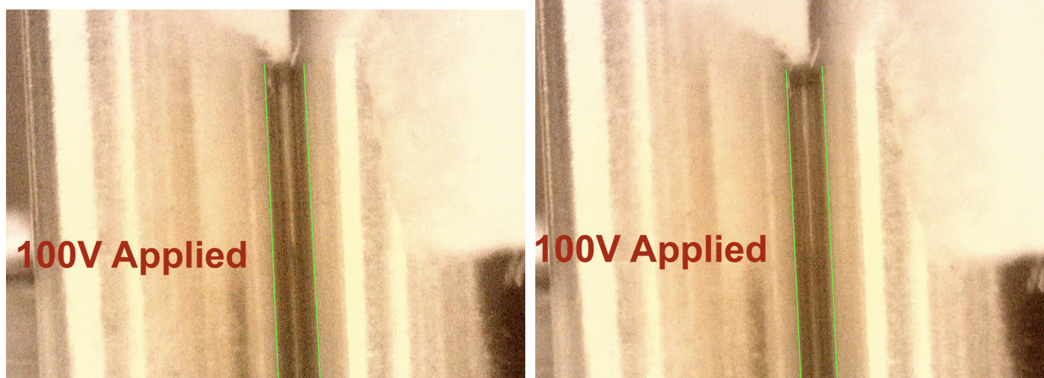

Figure 9-25: So long as voltage is applied between the cylinders and the liquid reservoir, liquid continues to flow into the filter paper until it is saturated.

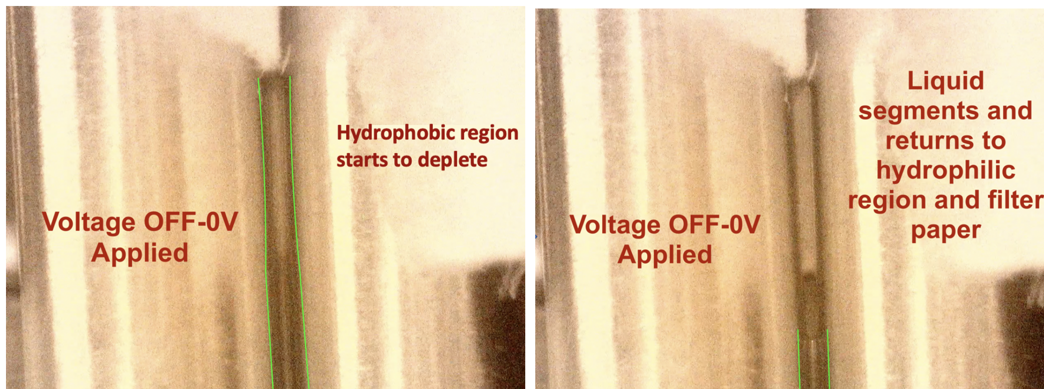

Figure 9-26: Once voltage is removed, the hydrophobic contact angle restores in the fluoropel region, causing the liquid to form a capillary instability and segment between the filter paper and reservoir ends of the rails.

proof that sufficiently rounded open capillary rails or microchannels, combined with an electrowetting region, can both initialize and stop flow to a porous material at the end of the channel or rail from an upstream neutral pressure liquid reservoir. This was the intended operational outcome of the hypothesized electrowetting flow controller. The following section will present the results of the monodisperse emitter material work.

9.2 Monodisperse Emitter Thrusters

Following many trials and iterations of silica resin batches, a suitable candidate solution was found using 1.5 micron silica nanospheres at a fractional mass loading of

approximately 75 percent with respect to the UV curable resin. A detailed solution preparation walk-through is available in [2].

9.2.1 Material Characteristics

Initial porosity estimates for batches sintered at peak temperatures between 1120°C and 1160°C were all 42 percent +/- 2 percent as determined by liquid volume displacement of the chips as well as weighing the chips and comparing with solid amorphous silica of similar volume. This is close to the theoretical limit of packing density in simple cubic arrangement of spheres at 47.7 percent porosity. Pore size ranges between 250 nm and 500 nm depending on spherical packing density in the region shown in figure 9-27. It should be noted that SEM imaging does not provide decisive measurements of pore size. Mercury intrusion porosimetry can provide a clearer picture of pore size and distribution. However, the material is in the range sought for use in ion electrospray thrusters.

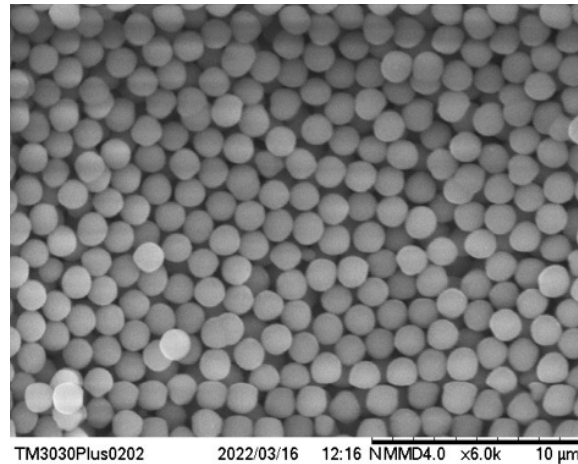

Figure 9-27: SEM image of 75 percent mass loading fraction after 1160°C sintering

Vickers Hardness testing was conducted on chips from each batch sintered between 1120°C and 1160°C and compared to previous emitter material hardness. This hardness data is shown in figure 9-29. Previous porous glass materials had hardness values of in the range of 35-45HV0.3. Some were harder than others and some had better uniformity than others, giving better repeatable tip geometries from laser ablation.

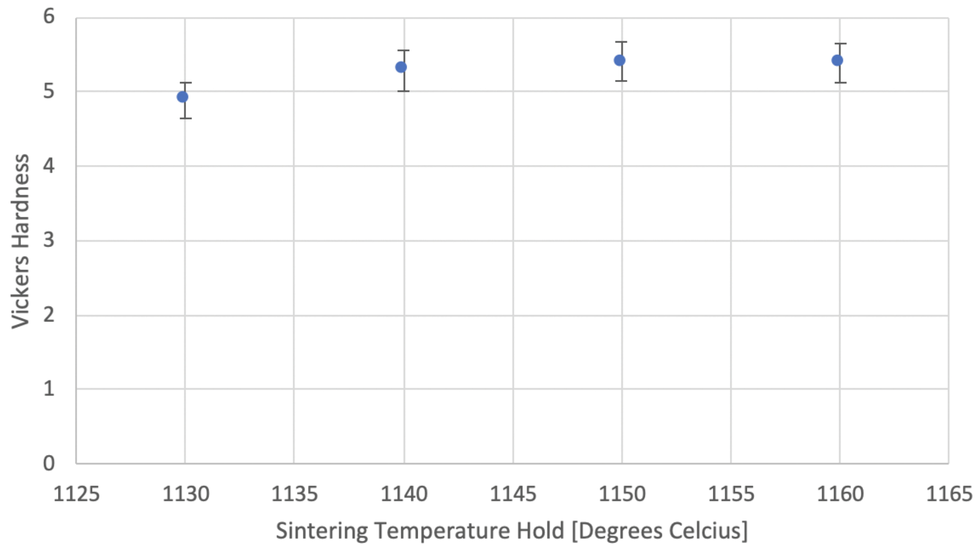

Figure 9-28: Vickers hardness test values under 300 gram force. Note no hardness value was determined for the 1120°C as it was just barely sintered and crumbled under any measurable load.

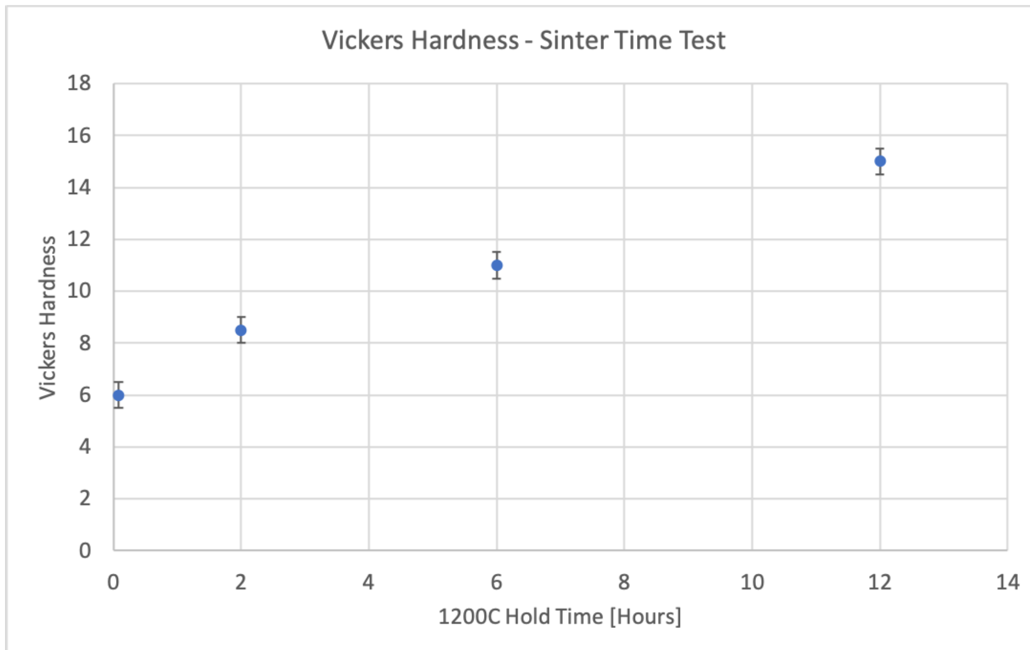

Figure 9-29: Vickers hardness test values under 300 gram force on samples held at peak 1200°C sintering temperatures for varying times. Note the clear increase in hardness as the hold time is increased.

The new sintered silica material is certainly less hard than previous materials by nearly an order of magnitude, but with increased sintering temperature hold times,

the hardness across the each emitter chip sample increases. After 12 hours of holding at 1200°C, the hardness value had more than doubled when compared to the 5 minute hold profile. The effects of these lower hardness values will be discussed along with the laser ablation results.

9.2.2 Laser Ablation of Emitters

Polished chips mounted on frames were laser ablated using a 0.25 Watt UV picosecond pulsed laser. Etch rates were determined to be on the order of 25 microns per pass, which is significantly higher than previous materials. This high etch rate is likely due to the relatively weak sintered bonds between the nanospheres in the bulk material as shown in the hardness testing. Various tip profiles were achieved by altering the number of laser passes and the diameter of gaps in the laser duty cycle during passes over the material.

Initial laser passes were done at a power of 0.5 Watts which created a noticeable amount of ablation debris during pass. Despite this, after 10 laser passes, conical tips were formed, albeit a bit more blunt than prior emitters with tip radii around 10-20 micron. The high ablation rate, although repeatable, is not ideal for smooth tip geometries as the layer "resolution" is much lower than if ablation is slower. Tip height uniformity was still excellent with variation across 10 measured tips of less than 10 microns. This emitter array (JG4-2) is shown in figures 9-30 and 9-31.

Subsequent laser ablation of the material was performed at a lower laser power of 0.25 Watts. This significantly reduced the amount of debris created by each laser pass, providing much smoother tips overall and allowing for tighter tip radii (17 micron) to be formed although with more of a flat plateau at the top of each tip. Tip height was approximately 300 micron and varied by a smaller 5 micron magnitude across 10 measured tips as compared to 10 micron with the higher power laser setting. This emitter array (JG4-3) is shown in figure 9-32.

During silica solution development a trial batch was created utilizing 750 nanometer diameter silica microspheres instead of the typical 1.5 micron nanospheres. This material had a slightly higher Vickers hardness of 8HV0.3 but would have smaller pore

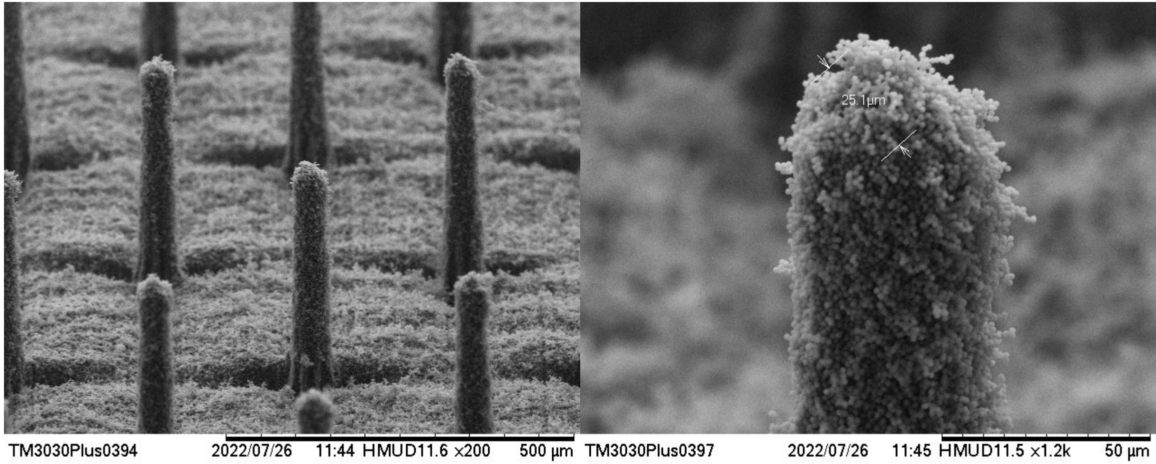

Figure 9-30: Laser ablated emitter tip array JG4-2.

Figure 9-31: Tip profile of JG4-2 emitter, note well-rounded tips, but rather blunt.

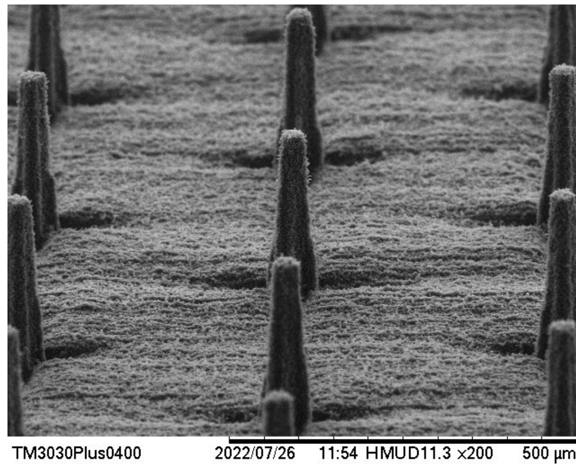

Figure 9-32: Laser ablated emitter tip array JG4-3.

sizes that were present in prior porous glass emitters. This may be a useful trait, but in order to compare with the older emitter material, emphasis is on the larger pore material. Nonetheless, it was also mounted on a thruster frame and ablated at 0.5 Watts and required 15 passes laser passes to achieve tip heights of approximately 300 micron +/- 8 micron across 10 measured tips. This emitter (JG6-2) is shown in figure 9-33.

Finally, with the lessons learned from prior ablation attempts, a 1.5 micron nanosphere emitter chips was ablated at 0.25 Watts with a 30 micron laser pass gap which resulted in very smooth, very sharp (approximately 4.6 micron radius) emitter

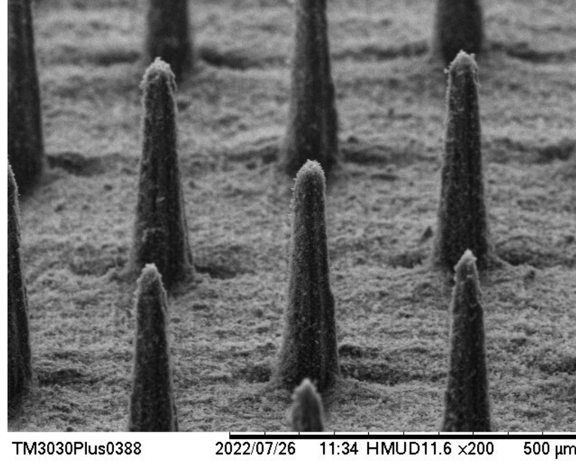

Figure 9-33: Laser ablated emitter tip array JG6-2, note smaller 750nm diameter nanoparticles are used here.

tips with minimal debris. This emitter array had tips approximately 300 micron tall all with less than 5 micron of height variation across 10 measured tips. This sintered silica emitter tip radius is markedly less than the measured radius of 20 micron seen in best case SPG emitter tips where tip height varies by around 15 microns. This emitter array (JG4-4) is shown in figures 9-34 and 9-35.

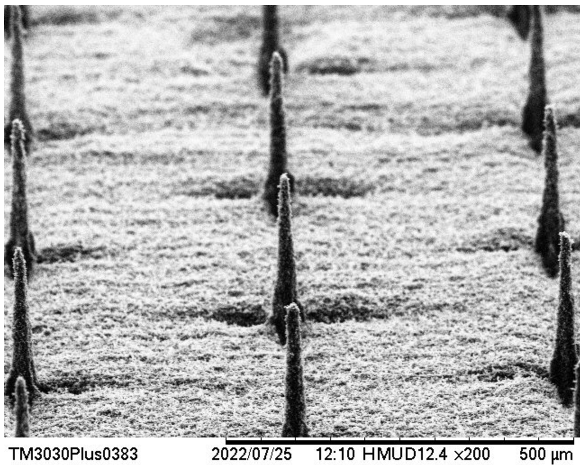

Figure 9-34: Laser ablated emitter array JG4-4.

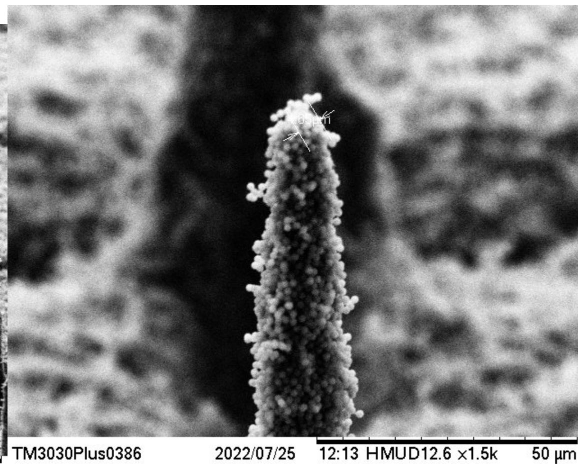

Figure 9-35: JG4-4 emitter tip, note very sharp profile with <5 micron radius of curvature.

The larger pore material thrusters were paired with extractors and fired to characterize thruster performance with the new emitter material.

9.2.3 Thruster Firing

The first emitter tested was JG4-3. This emitter was fired first given it had the least sharp tips (due to plateau features mentioned earlier.) The thruster was mounted in a temporary firing mount and loaded with 5 droplets of desiccated EMI-BF4 ionic liquid and allowed to fully saturate the porous tips. The thruster was placed in a vacuum chamber equipped with a time-of-flight (TOF) mass spectrometer and pumped down to 10^{-6} Torr prior to firing. Current emission occurred at 1200V and the current-voltage response is shown in figure 9-36. It is possible that the current spikes at 1800V are due to unstable emission behavior. Also noteworthy, asymmetric ion emission across positive and negative polarities, which has been seen in prior thruster firings with temporary mounts and only a few drops of ionic liquid [1]. Time-of-flight mass spectrometry was recorded at positive and negative 1800V during the initial firing of this thruster. 20, 50, and 100 microsecond time divisions on an oscilloscope captured the data that was subsequently plotted as normalized current vs. mass of the emitted ion species [46]. The TOF for JG4-3 is shown in figure 9-37 and the derived values of thrust, specific impulse, mass flow rate and efficiency are shown in figure 9-38. These values are attained from the output of the TOF post-processing matlab script written by Amelia Bruno of MIT. It is listed in the appendix. Even with the plateaued tip profiles of JG4-3, the TOF data suggests pure ionic mode operation consisting of largely of monomer and dimer ion species. The use of 1800V for TOF on this thruster is actually not ideal given the occasional emission spikes seen. For subsequent tests, a lower voltage is used that demonstrates stable emission over time without any spikes in current emitted.

Following the successful firing of the JG4-2, the sharper tipped JG4-4 emitter was set up on a temporary mount and loaded with 5 droplets of EMI-BF4 and allowed to fully saturate the tips prior to loading into the vacuum chamber. JG4-4 displayed predictably lower current emission start-up voltage around 700V and current-voltage data is shown in figure 9-39. TOF for JG4-4 is shown in figure 9-40 and the associated derived performance metrics are shown in figure 9-41. Again, this thruster appears

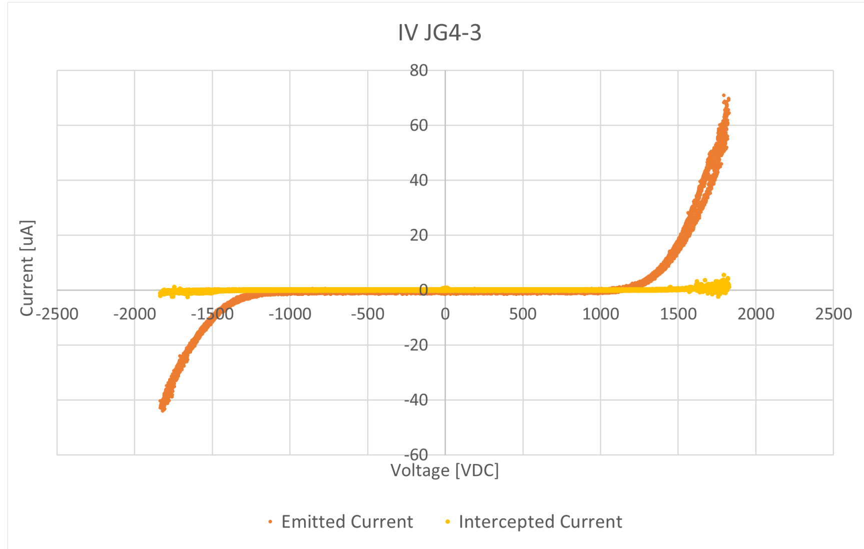

Figure 9-36: JG4-3 voltage-current relation.

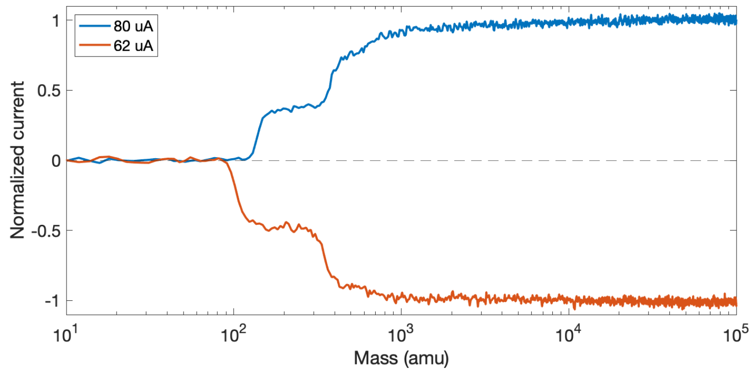

Figure 9-37: JG4-3 time-of-flight mass spectrometry.

Voltage (V)	Current (uA)	Thrust (uN)	Isp (sec)	m_dot (ug/s)	Efficiency
1800	80	9.6016	2296.4	0.42622	0.75104
-1800	62	5.7789	3163	0.18624	0.80338

Figure 9-38: JG4-3 time-of-flight derived performance metrics.

to be operating in the purely ionic emission regime. Given the very sharp tips of JG4-4, it is no surprise the intercepted current from the extractor is very small, on the order of single micro-amps for several hundred micro-amps of emitted current. This tip profile is very promising for future thruster use.

Lastly, JG4-2 was selected as the thruster to be used for long-duration lifetime firing tests. Instead of a temporary mount, JG4-2 was attached to a propellant tank

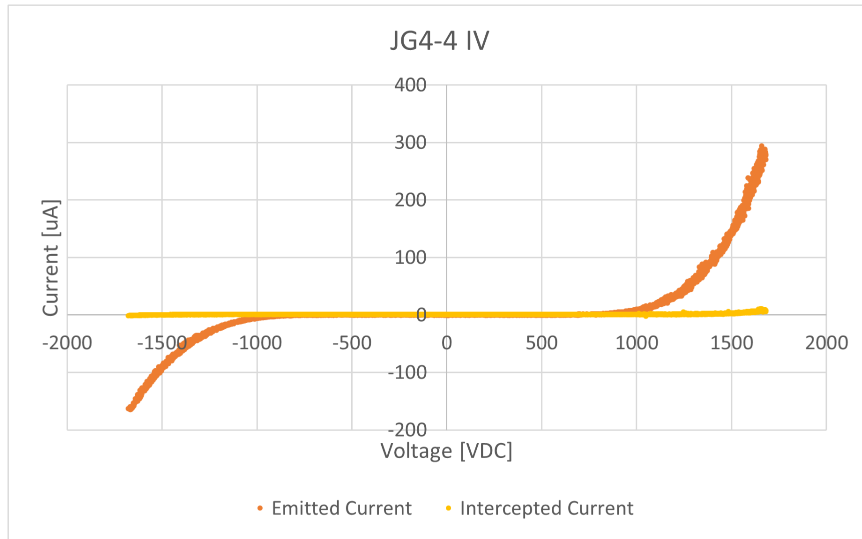

Figure 9-39: JG4-4 Voltage-Current relation. Note I1 corresponds to emitted current and I3 corresponds to current intercepted by the extractor grid.

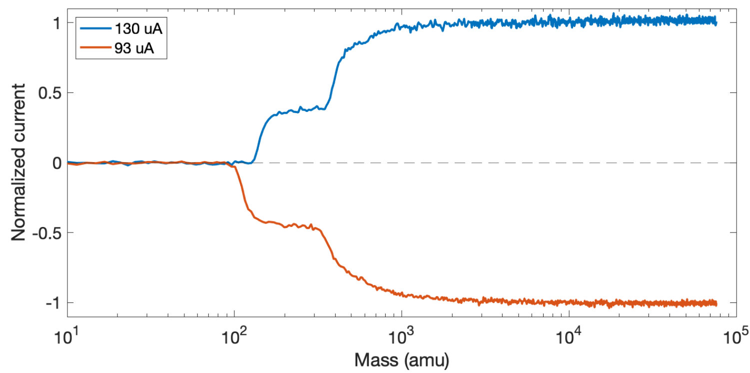

Figure 9-40: JG4-4 time-of-flight mass spectrometry.

Voltage (V)	Current (uA)	Thrust (uN)	Isp (sec)	m_dot (ug/s)	Efficiency
1450	130	13.552	2272.1	0.60802	0.80125
-1450	93	9.1053	2558.9	0.36272	0.84749

Figure 9-41: JG4-4 time-of-flight derived performance metrics.

holding about 8mL of desiccated EMI-BF4. Emission starts around 900V for JG4-2 and the current-voltage response is shown in figure 9-42. Once stable emission in both polarities was achieved, the thruster was fired on a square wave, changing polarities between +1100V and -1100V every 30 seconds. TOF data was collected when emission current was stable and symmetric at 150 micro-amps in both polarities and is shown in figure 9-43 along with the derived performance metrics in figure 9-44.

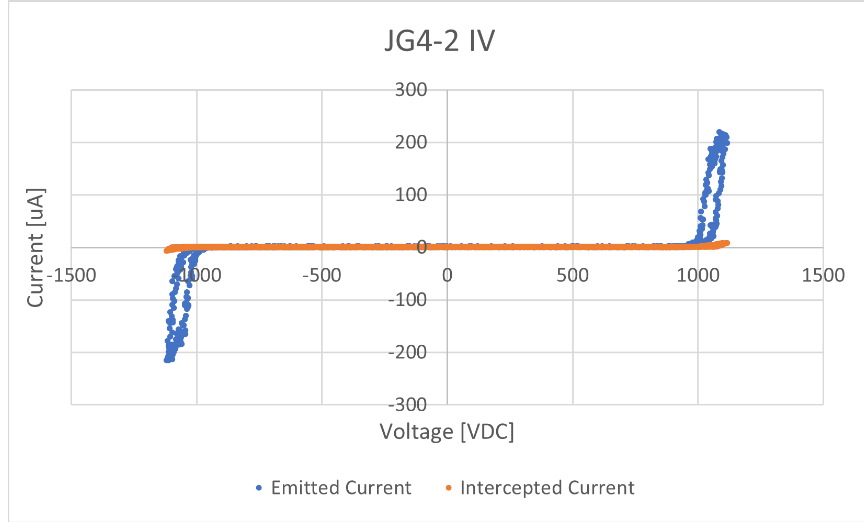

Figure 9-42: JG4-2 emission current-voltage data.

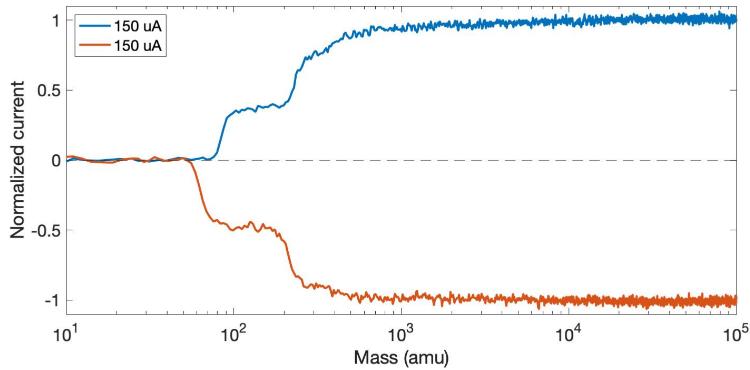

Figure 9-43: JG4-2 TOF data.

Voltage (V)	Current (uA)	Thrust (uN)	Isp (sec)	m_dot (ug/s)	Efficiency
1100	150	11.388	27122	0.042799	9.1816
-1100	150	7.4322	667.54	1.1349	0.14749

Figure 9-44: Derived performance metrics for JG4-2

A rotating stage that the thruster was attached to within the tank was used in combination with the TOF mass spectrometer to estimate ion beam shape half-angle for JG4-2 at approximately 40 degrees. Once data was collected, the JG4-2 thruster was left firing continuously on the square wave profile while logging current-voltage

data for 30 hours until the thruster developed a liquid short with the extractor shown in figure 9-45 and ceased firing. The lifetime current-voltage data is shown in figure 9-46.

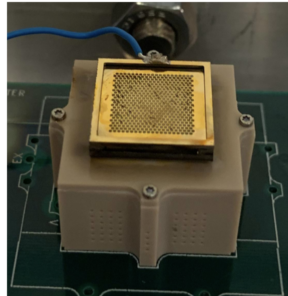

Figure 9-45: Liquid shorts (dark spots) in JG4-2 after firing for 30 hours.

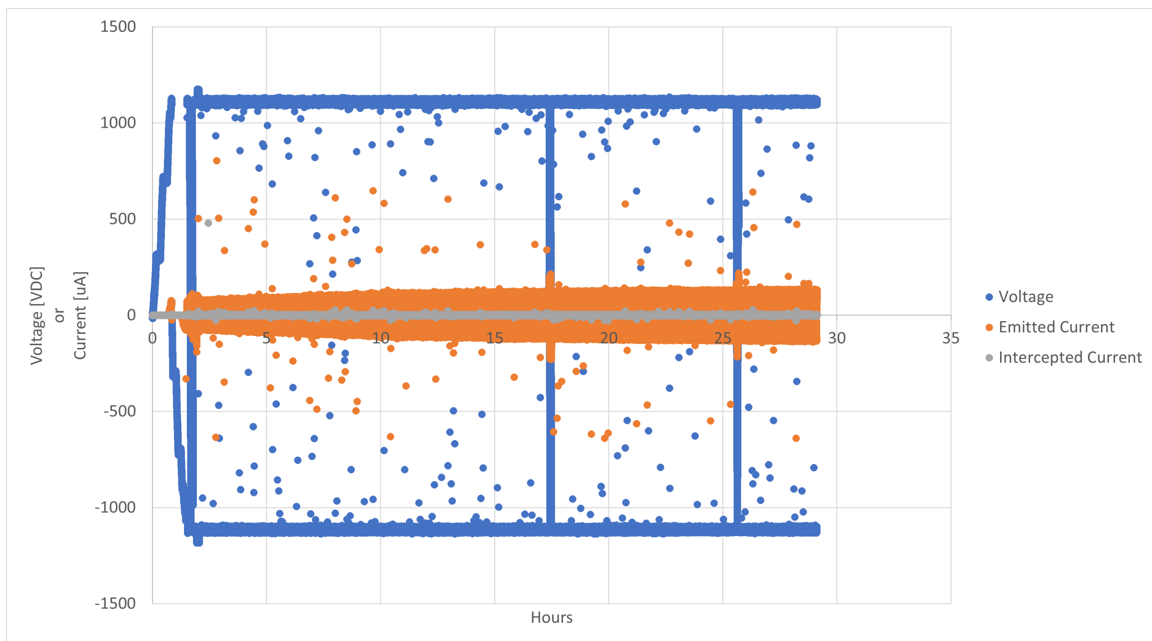

Figure 9-46: Lifetime current emission-voltage data for JG4-2. Note shorts developed just prior to 30 hours and are truncated to see hour marks.

Throughout the duration of firing, occasional current spikes were logged. It is possible these spikes were due to tiny droplet emissions being emitted or intercepted by the extractor and/or unstable emission behavior.

Chapter 10

Discussion

Following multiple rounds of testing electrowetting open microfluidic devices fabricated a variety of ways with a variety of liquids, it is clear that while operating an electrowetting open microchannel within a window of aspect ratio, contact angle, and voltage, on-off flow control can be achieved and repeated. A number of important lessons learned from these tests should be noted.

Firstly, in order to operate a device based on a repeated electrowetting effect, the repeatability of the liquid-hydrophobic-dielectric combination must first be thoroughly tested. In the case of several hydrophobic coatings that were tested, the coating provides an initial contact angle well above the wetting threshold of 90 degrees, but upon electrowetting activation, the contact angle of the liquid falls below the threshold and never returns to its unmodified state. It was found that only spin coated fluoropolymer (in this case Fluoropel) was effective in achieving a repeatable contact angle change from above the wetting threshold to below it and back above it again once voltage was removed. It remains to be seen if this degradation in attainable contact angle range has any atmospheric reliance, as the coatings were not tested cyclically under vacuum. This would be a logical next step. This proved difficult when dealing with the selective coating of an open capillary later on, but nonetheless, demonstrated excellent electrowetting contact angle curves for every liquid of interest (with the exception of EMI-IM which never demonstrated a hydrophobic contact angle on the hydrophobic coatings tested.) With the contact angle

data ranges measured for each liquid atop the fluoropel, the second component of determining operation windows was to test the aspect ratio limitations of spontaneous capillary flow in open microchannels.

$$\frac{p_f}{p_w} < cos(\theta) \tag{10.1}$$

Based on the free energy-derived SCF criteria, for a particular liquid with a known contact angle range via electrowetting, a minimum aspect ratio to enable wetting at the lower end of the contact angle range can be selected. For instance, with water having an electrowetting contact angle range of 81 degrees to 115 degrees on non-plasma treated fluoropel, this would suggest a rectangular channel depth-to-width aspect ratio of no less than 2.7 would enable the liquid to flow into the channel. This limit may prove difficult to demonstrate, so going a bit past the limit, say to an aspect ratio of 3, should enable the desired flow under electrowetting alone. To ensure segmentation, this aspect ratio should not be overly large either, as the positive pressure generated by the water once it is back to 115 degrees in the hydrophobic region of the channel asymptotes with increasing channel depth. Increasing channel depth past the SCF onset aspect ratio also lends to an increase in viscous drag due to more channel wall surface area in contact with the water, so flow rate to the second reservoir (or thruster emitter) would be decreased.

For a desired flow rate application, two options exist for sizing. Either multiple channels with very slow flow rates could be multiplexed to achieve a net flow rate much higher or a single large channel sized to match the viscous drag (longer channels of fixed aspect ratio experience more drag) to the desired flow rate. For the application of electrospray propulsion, the latter option is quite appealing due to the lack of a gravitation limitation on what constitutes a "microfluidic" device. This means that surface tension is always dominant in a zero-gravity environment, so a microchannel that would not be able to wick liquid in the presence of gravity should, in theory, be able to transport liquid unimpeded in space. Once the crucial parameters of liquid properties, electrowetting contact angle range, and desired flow rate are known, back-

solving for a device design is relatively straightforward. The difficulty then lies in the fabrication of a device based on whatever combination of viable parameters are found.

As discussed, the physical fabrication of the microchannel is relatively straightforward. Maintaining a sufficiently smooth and rounded channel wall surface is a bit tricky, but the most difficult aspect is the application of a robust electrowetting hydrophobic and dielectric layer to a portion of a microchannel that will want to distribute whatever liquid is placed inside of it. By utilizing the photolithographic masking techniques discussed in prior chapters, common spin-coated fluoropolymers used in electrowetting applications can be effectively utilized in selectively coating regions of open microchannels. As the channels become larger, this process becomes significantly easier, so for a channel with width greater than 1mm as an example, masking becomes much more user friendly.

For the case with metallic cylinder capillary rails, applying a selective hydrophobic coating is much more user-friendly and it is pretty clear that the rail is sufficiently rounded given its circular cross-section. The same on-off flow and segmentation behavior was seen in the preliminary tests of this device as well, although the range of contact angles is more limited in this case.

A primary goal of this work was to develop a solid-state flow controller that could be integrated into the fluid path of an electrospray thruster and offer repeatable on-off-on flow control to a thruster on command. **While there is much to be learned about such a device, the preliminary testing results suggest the combination of electrowetting with rounded open microchannels accomplishes the goal of repeatable solid-state flow control for electrospray thrusters**.

In addition to the depth of work on the electrowetting flow controller problem, the development of a new monodisperse sintered nanoparticle material for use in electrospray thrusters has shown promise in improving emitter tip profiles, material uniformity, and thruster performance. Pore size of the material can be tuned via the selection of different diameter nanoparticles or by choosing a distribution of varying size nanoparticles. Additional material tunability is gained from the sintering process.

Vickers hardness testing showed a trend in the increasing hardness of the porous material with increased sintering time. So long as the sintering is not carried out to a degree that melts all of the nanoparticles into a solid structure, porosity and pore distribution could also be tailorable, but further analyses of the pore distribution would be needed to confirm that. From the many ablation tests performed on the batches of emitter material it is clear that lower ablation energies give better shape control. This suggest that a "finer" tool, like a femto pulse laser at relatively low energies may give excellent tip profile results. It may even be possible, with such fine control of the laser ablation rate, to discretely remove single nanoparticles for outstanding shape control. This would have a definite impact on thruster lifetime via improvements in ion beam optics and reduction of ions impacting the extractor grid. Additional control over the individual tip taper angle would be an added benefit to controlling hydraulic impedance along the tip as well as aid in passive mitigation of emitter flooding.

From the tests run on the monodisperse sintered emitter material batches, a clear improvement in statistical tip uniformity, sharpness, and start-up voltage was measured as compared to prior porous glass emitter materials. Post-ablation treatments might further improve on these gains as well. Thorough cleaning of stray nanoparticles from the emitters, chemical etching of the emitter tips, and even depositing a thin layer of hydrophobic coating to the tips could work in tandem to further reduce the risk of premature thruster failure.

Chapter 11

Future Work

The goals of this work were to analyze and demonstrate the viability of an electrowetting open microchannel flow controller and achieve better emitter material uniformity and tip geometry control for electrospray propulsion. While electrospray propulsion was the target use-case, both the electrowetting flow controller architecture and the sintered monodisperse porous material have many interesting traits that may be discovered with further studies. As such, there is some future work that may be of interest to both the Space Propulsion Lab at MIT and the broader microfluidics and materials science communities.

11.1 Electrowetting Flow Controller

For the electrowetting flow controller, the lifetime capability of the selected fluoropolymer hydrophobic layers and their eventual degradation would be of great value to further understand. The possibility of alternate fluoropolymer, ceramics, or even nanotextures would be a worthwhile complementary study. If such degradation of the hydrophobic effect over multiple cycles could be mitigated, the flow controller may have many applications in microfluidics whereby a flow must be sustained or stopped actively to a porous media. Additional work looking into alternative geometries would also be of interest. For instance, there is no set need for a 3 walled channel for the intended physics to hold.

More conventional fabrication such as milling or stamping of the microchannel devices could also be of interest so long as the dielectric and hydrophobic coatings are paired well and the surface finish is sufficiently smooth. This would also lend to a much cheaper cost of production as compared to semiconductor fabrication methods in silicon.

The cylinder device was primarily tested as a way to macroscopically show the effects of the capillary ledge rounding, but it behaved so well, it would be worth continued research into similar configurations. The more limited contact angle range would not be an issue for the lower contact angle EMI-IM and with the use of optical stages, the separation of the cylinder can very accurately be controlled. Further characterization of a cylinder device to the extent of the silicon microchannel devices would be of interest.

One well-known shortcoming of all open microfluidic devices is their susceptibility to contamination. While the present work included extensive cleaning steps prior to testing the devices in a low particle clean room environment, contamination mitigation studies for such open microchannels could further improve the robustness and range of potential applications outside of spaceflight, where dust and debris is not present once in orbit.

As mentioned in previous chapters, EMI-IM is a particularly appealing propellant for electrospray due it not absorbing nearly as much ambient water as EMI-BF4 tends to. As such, determining a combination of device parameters to enable use of EMI-IM would complement this work well. Additionally, testing all hydrophobic coatings with ionic liquids under vacuum would require a unique contact angle measurement approach. This data would further help in understanding the operational ranges of the electrowetting flow controller.

11.2 Monodisperse Porous Materials

On the topic of the sintered monodisperse materials, there is a vast range of dials to be turned that have implications on the outcome of the final material. Namely,

the selection of nanoparticle size or sizes, sintering temperature and hold time, laser ablation power, ablation pulse frequency, and post-processing. The next logical step for use in electrospray applications would likely be to focus on the laser ablation and post-processing steps, given the repeatability of the current material formulation process being quite good. Microstructures that are not attainable with picosecond laser pulse frequency may be achieved with much faster femtosecond laser capabilities. However, the resulting tips are only as good the durability of their geometry once wetted, so stray nanoparticles of ablation debris that can move in the presence of liquid must be carefully removed. Current processes utilize low pressure nitrogen and ultrasonic bath cleaning steps, but further cleaning and even light chemical etching processes could pair nicely with improvements in the laser ablation resolution.

Lastly, given that the procedure developed to produce the monodisperse sintered porous emitter materials relies on a PDMS mold to cast the emitter chips, it would be interesting to see the limits in casting size of a sintered porous emitter. It may be possible to dramatically increase the size (or even decrease if desired) of each porous chip by simply creating larger molds to pour the resin solution into prior to UV curing.

THIS PAGE INTENTIONALLY LEFT BLANK

Chapter 12

Conclusion

This thesis work sought to add active flow control to electrospray propulsion systems and address the lifetime shortening phenomenon referred to as emitter flooding by developing a solid-state active flow control device and a monodisperse porous emitter material.

The combined implementation of the flow controller and monodisperse emitter material will not only offer improvements to thruster performance but also system robustness with the ability to actively control flow in a repeatable manner to the thruster as needed. With active flow control between the thruster and propellant reservoir, it may now be possible to achieve fine-control of thrust and Isp when regulating the flow rate actively, and compensate for other unavoidable system fluctuations, like temperature effects on liquid viscosity. While the application area that drove this research was primarily focused on electrospray thrusters, the resulting lessons learned about the flow controller and new porous material have broad applications in the areas of microfluidics and material science.

First, building on the analysis of [26], the Modified Lucas Washburn model was used to determine the effective channel sizing necessary to spur Spontaneous Capillary Flow (SCF) for a number of liquids. These liquids included EMI-BF4, EMI-IM, water, glycerol, and a water/IPA mixture. The analytical predictions for flow rate into the unwetted channel was used as a basis for determining the efficacy of the model in open microchannel flow dynamics. Additional analysis was done using a numerical

computational fluid dynamics platform to doubly confirm the analytical model and also predict more complex fluid dynamics. Namely, the simulation of expected liquid segmentation once the contact angle of the liquid with the open microchannel walls goes from a wetting (<90 degree) to non-wetting (>90 degree) angle. It was predicted that this change in surface wettability brought on via electrowetting should cause an instability that forces the liquid to deplete in the hydrophobic region in favor of the lower pressure channel ends. Re-application of voltage subsequently lowers the contact angle below the SCF limit again, spurring re-wetting of the channel. This repeatable process allows for cyclic on-off flow control between a liquid reservoir and porous thruster emitter, effectively mimicking the same level of active flow control seen in much larger pressure-driven valved propellant management systems.

Second, the lessons learned from the analytical and numerical modeling work were put to use on an experimental device. The first set of experiments focused on testing each liquid atop a variety of dielectric and hydrophobic coatings to see which combination produced the desired wetting and non-wetting contact angle ranges repeatably. Once a hydrophobic-dielectric combination was identified that worked with one propellant in particular, EMI-BF4, that combination was implemented into a fabrication process for experimental devices. These experimental devices were fabricated in silicon using semiconductor fabrication techniques to create open microchannels of fixed aspect ratios with rounded channel ledges to prevent liquid pinning during operation. The silicon devices were then given the same dielectric layers followed by a selective hydrophobic layer deposition treatment to mimic the channel geometry and boundary conditions used in the analysis. The devices were tested with a variety of liquids, and the wetting velocities of the liquids into the channels, under the effects of electrowetting and capillary forces, were compared to the predicted velocities from prior analyses. A second set of tests included a porous emitter substrate at the end of each microchannel and the use of EMI-BF4 as well as water. These tests demonstrated the desired flow to the emitter under the effects of electrowetting and capillary forces and then, once voltage was removed, the eventual liquid depletion and segmentation in the region of the channel with the hydrophobic coating applied. This effectively

demonstrated the physical effects predicted and desired from the earlier analysis work. These new devices, while not perfect, demonstrate the feasibility of solid-state flow control within the scope of electrospray thruster operating conditions.

Lastly, to further improve on the fluid management in electrospray propulsion systems, a new monodisperse porous emitter material was created. Using a silica nanoparticle solution with UV curable resins, chips were cast with a maximum mass loading fraction of nanoparticles the solution would support. The cast solution was cured via UV light and a sintering profile was developed to attain a hard and handleable, yet porous, monodisperse emitter material. This new material has much improved macroscopic uniformity which, once laser ablated, resulted in sharper emitter tips and more uniform wetting properties across the bulk material than prior porous glass materials used. The ability to ablate the material with just 0.25 watts of laser power resulted in finer control over tip geometry which, in turn, led to lower start-up voltages for the electrospray thruster as well as lower intercepted currents that some prior glass emitters.

Overall, the electrospray thruster offers excellent low-thrust and high-efficiency propulsion capabilities, but lacked simple active propellant management that is commonly seen in other electric and chemical propulsion systems used in spaceflight. Laboratory tests of electrowetting open microchannel flow controllers, designed based on simple analytical models and paired with a new monodisperse emitter material, improves the robustness of the electrospray propulsion system by adding a the capability of active fluid management and finer control over emitter geometry and pore distribution.

THIS PAGE INTENTIONALLY LEFT BLANK

Appendix A

Time of Flight Post Processing

In order to derive the thruster performance values based on the collected time-of-flight data for each thruster, an electrospray characterization program is utilized. This program was written by Amelia Bruno, a fellow graduate student in the Space Propulsion Lab at MIT. The following Matlab script is utilized for this post-processing:

```
function[TOF_results] = TOF_postprocess(input,varargin)

% Run this function in the same directory/path of all TOF scope files.
%
% INPUTS:
%   input_table:    nxm table of TOF data with the fields SCOPE, VOLTAGE,
%                   CURRENT, BCKGND.
%                      - scope = numbers of scope file (e.g. file format is
%                               scope_###.csv)
%                      - voltage = firing voltage in +/-V
%                      - current = emitted current in +/-uA,
%                      - bckgnd = number of scope file of backgnd scan
% (OPTIONAL NAME/VALUE PAIRS):
%   trunc:          scalar (double) of mass to truncate performance calc.
%   leg_str:        nx1 cell of strings, for legend entries.
%
% OUTPUTS:
%   TOF_results:    nx6 table of TOF results, summarizing voltage, current,
%                   thrust, Isp, m_dot, and polydispersive efficiency.


%% Initialize

% Input table or matrix

scopefiles = input.scope;
bckgndfiles = input.bckgnd;
Vtof = input.voltage;
Itot = input.current * 10^(-6);

% Constants
e = 1.6e-19; % C
mi = 1.66e-27; % kg/amu
L = 111.1/100;  % tof distance in turbovac, meters
g = 9.81;
pol = sign(Vtof); % firing polarities

% Handle varargins
p = inputParser;
addParameter(p,'trunc',0);
addParameter(p,'leg_str',append(string(table2array(input(:,3))),' uA'));
parse(p,varargin{:});

%% Pull and format data
for n=1:length(scopefiles)
    tof = readmatrix(['scope_' num2str(scopefiles(n)) '.csv']);
    bckgnd = readmatrix(['scope_' num2str(bckgndfiles(n)) '.csv']);
    tof(:,3) = tof(:,3)-bckgnd(:,3); %subtract background noise
    tof(any(isnan(tof), 2), :) = []; %remove NaNs from scope file
    dT = diff(tof(:,2));
    gate = find(abs(dT)==max(abs((dT))))+1; %locate gate signal
    tof = tof(gate:end,:); %pull tof data only after gate signal
    if p.Results.trunc > 0
        t_trunc = L./(sqrt(2.*e.*abs(Vtof)./(p.Results.trunc*mi)));
        [~,ind] = min(abs(tof(:,1)-t_trunc(n)));
        trunc_ind(n) = ind;
        tof = tof(1:ind,:);
    end
    if dT(gate-1) < 0 % triggered on gate open (rising slope)
        minI = mean(tof(end-20:end,3));
        maxI = mean(tof(20:30,3));
        rise(n) = true;
    elseif dT(gate-1) > 0 % triggered on gate close (falling slope)
        maxI = mean(tof(end-20:end,3));
        minI = mean(tof(1:20,3));
        rise(n) = false;
    else
        disp(['No difference in values automatically detected between '...
         'initial and final datapoints on TOF spectra. Check data.']);
        plot(tof(:,3))
    end
    % Truncate at gate, correct offset and normalize
    tof(:,3) = (tof(:,3) - minI)/(maxI - minI);
    % Convert t to amu
    mass = 2*e*abs(Vtof(n))./(L./tof(:,1)).^2;
    m_amu = mass/mi;
```

```
    % Save TOF
    TOF{n} = [m_amu pol(n)*(1-tof(:,3)) tof(:,1)]; %format: m_amu, TOF signal, time
end

%% Estimate performance
F=[];mdot=[];Isp=[];eta=[];
for i=1:length(scopefiles)
    t = TOF{i}(:,3); rtofL = TOF{i}(:,2);
    if rise(i)
        rtofL = 1+(-1)*pol(i)*rtofL;
    end
    F(i) = abs((2*Vtof(i)/L) * trapz(t,(Itot(i)*rtofL)));
    mdot(i) = abs((4*Vtof(i)/(L^2)) * trapz(t,t.*(Itot(i).*rtofL)));
    Isp(i) = F(i)/(mdot(i)*g);
    eta(i) = abs((F(i)^2)/(2*mdot(i)*Itot(i)*Vtof(i)));
end

% Sort data into table
table_labels = {'Voltage (V)','Current (uA)','Thrust (uN)', 'Isp (sec)', 'm_dot (ug/s)', 'Efficiency
TOF_results = table(Vtof,Itot*10^6,F'*10^6,Isp',mdot'*10^9,eta','VariableNames',table_labels);

%% Plot TOF signals
f=figure;
for q=1:length(scopefiles)
    semilogx((TOF{q}(:,1)),TOF{q}(:,2),'LineWidth',2); hold on;
end
xlim([10^1 10^5]);
ylim([-1.1 1.1]);
yline(0,'--'); %grid on
legend(p.Results.leg_str','Location','NorthWest')
xlabel('Mass (amu)'); ylabel('Normalized current')
set(gca,'fontsize',16)
f.Position = [180   426   820   371];


end
%% Subfunctions
function[small] = bin5(data)
l = length(data);
for i = 1:ceil(l/5)
    try
        small(i) = mean(data(5*i-4:5*i));
    catch err %if vector length not divisible by 5 at end
        if i == ceil(l/5)
            if contains(err.message,'exceeds array bounds')
                small(i) = mean(data(5*i-4:end));
            end
        end
    end
end

end
```

THIS PAGE INTENTIONALLY LEFT BLANK

Appendix B

Pressure Contours for Tested Liquids in Open Microchannels

The following plots of expected liquid filament pressure in open rectangular microchannels serve to establish performance envelopes for a known liquid-hydrophobic coating electrowetting curve. Once the contact angle range is known, the generalized Cassie angle can be calculated based on aspect ratio. So long as the generalized Cassie angle falls below the 90 degree threshold, the channel will wet, once above this 90 degree threshold, the pressure becomes positive with respect to the neutral reservoir and will recede or segment if the opposite channel end is also neutral or negative pressure. Plots for 50 micron wide, 100 micron wide, and 200 micron wide channels with varying depths are made for EMI-IM, water, and water/IPA mixtures to show the changing magnitude of pressure in open rectangular channels.

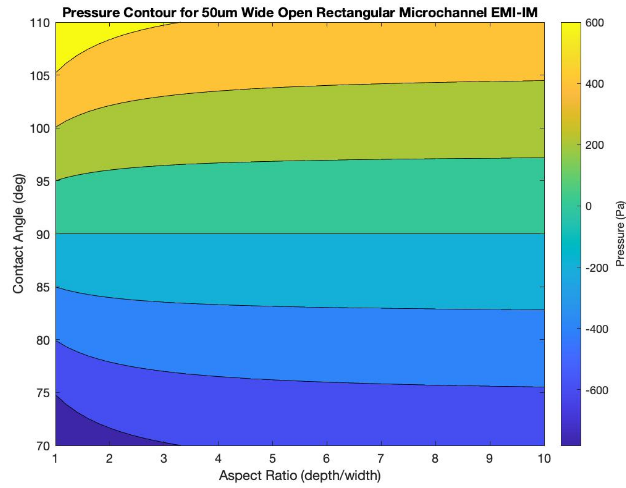

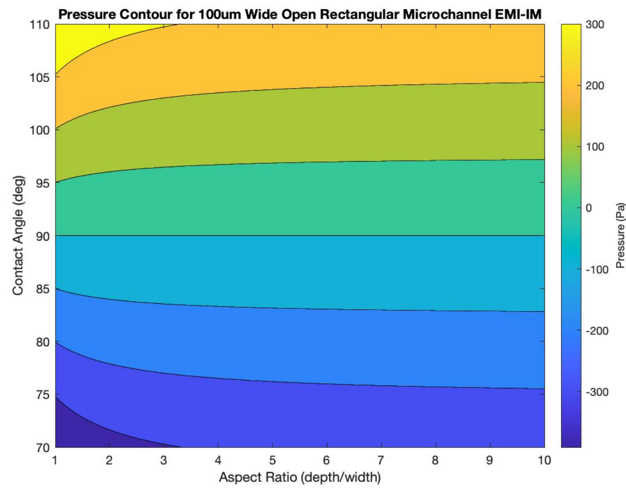

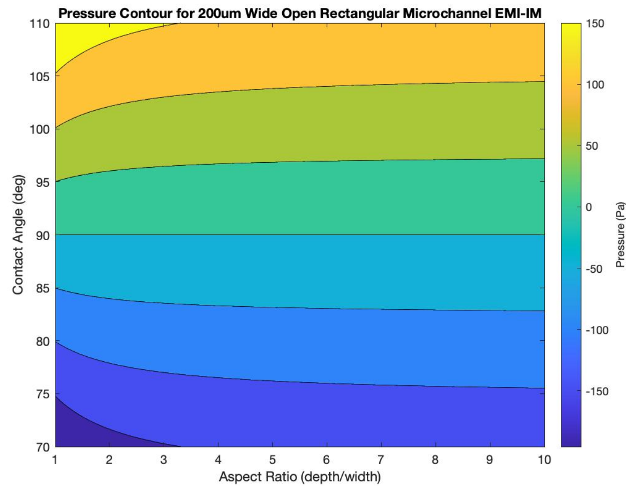

Figure B-1: EMI-IM pressure contours for varying depth microchannels based on a range of contact angles and channel depths. Note that not all contact angles are achievable, the range is physically set by the hydrophobic coating used for electrowetting.

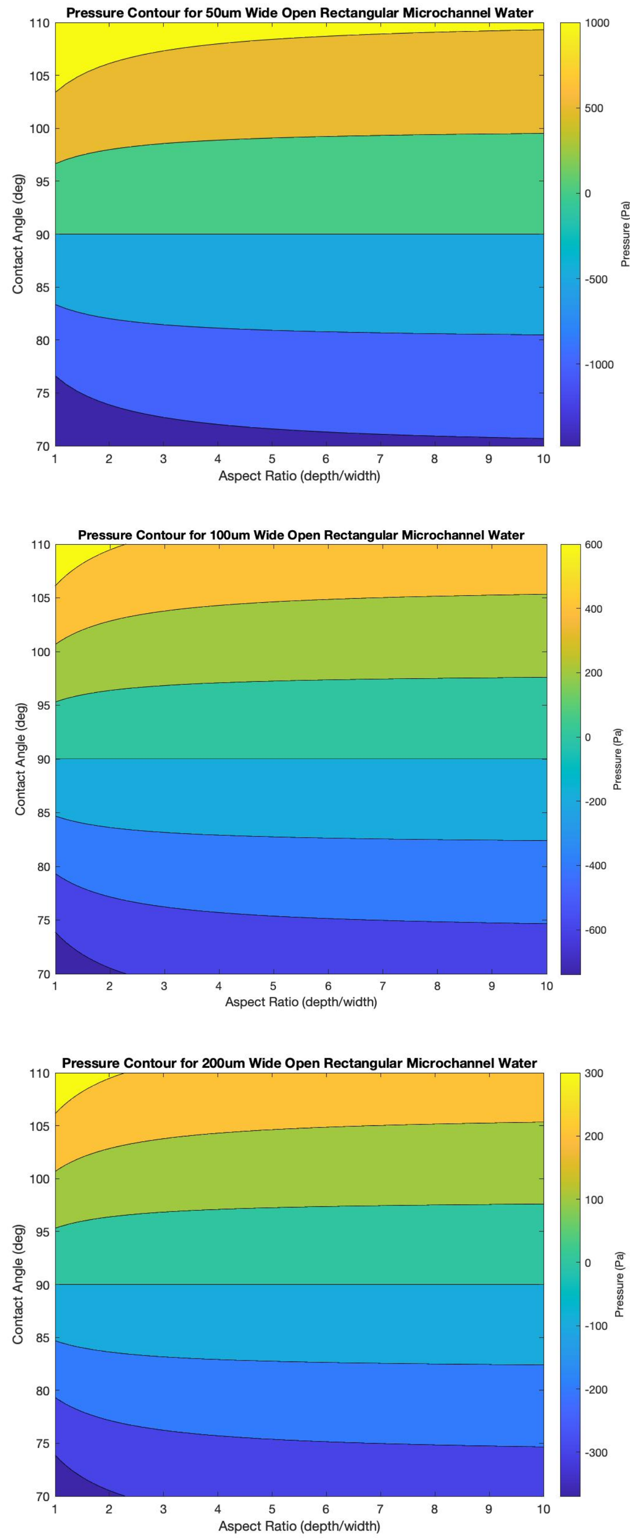

Figure B-2: Water pressure contours for varying depth microchannels based on a range of contact angles and channel depths. Note that not all contact angles are achievable, the range is physically set by the hydrophobic coating used for electrowetting.

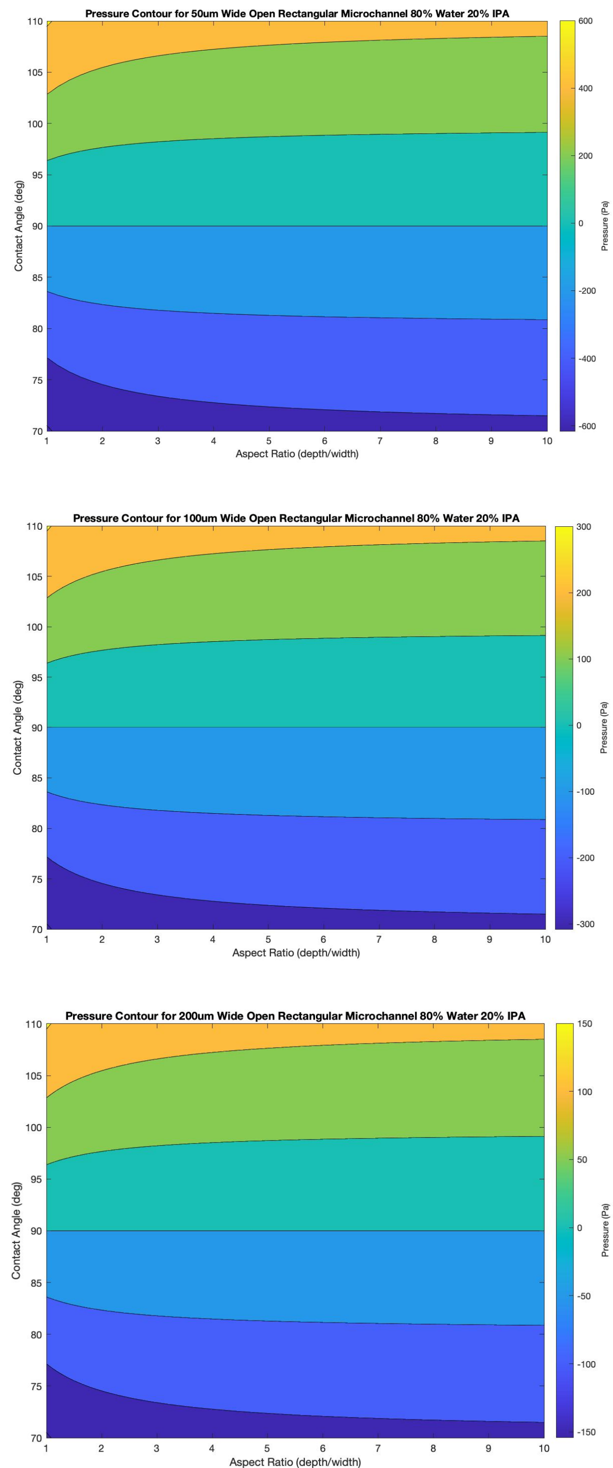

Figure B-3: 80% Water/ 20% IPA by volume pressure contours for varying depth microchannels based on a range of contact angles and channel depths. Note that not all contact angles are achievable, the range is physically set by the hydrophobic coating used for electrowetting.

References

[1] Dakota S. Freeman, "Design and Manufacture of the Next Generation of Ion Electrospray Thrusters", Master's thesis work, MIT Department of Aeronautics and Astronautics, 2019

[2] Jonathan MacArthur, "Material and Fabrication Developments in the Ion-Electrospray Propulsion System", Master's thesis, MIT Department of Aeronautics and Astronautics, 2020

[3] Daniel Courtney, "Ionic liquid ion source emitter arrays fabricated on bulk porous substrates for spacecraft propulsion", Ph.D thesis work, MIT Department of Aeronautics and Astronautics, 2011

[4] Louis Perna, "Design and manufacturing of an ion electrospray propulsion system package and passively-fed propellant supply", Master's thesis work, MIT Department of Aeronautics and Astronautics, 2014

[5] Natalya Brikner, Paulo C. Lozano, "The role of upstream distal electrodes in mitigating electrochemical degradation of ionic liquid ion sources", Appl. Phys. Lett. 101, 193504 (2012)

[6] Rebelo, L. P. N., Canongia Lopes, J. N., Esperanca, J. M. S. S., and Filipe, E., "On the Critical Temperature, Normal Boiling Point, and Vapor Pressure of Ionic Liquids," The Journal of Physical Chemistry B, Vol. 109, No. 13, 2005, pp. 6040–6043.

[7] Earle, M. J., Esperanca, J. M. S. S., Gilea, M. A., Canongia Lopes, J. N., Rebelo, L. P. N., Magee, J. W., Seddon, K. R., and Widegren, J. A., “The Distillation and Volatility of Ionic Liquids,” Nature, Vol. 439, No. 7078, 2006, pp. 831–834.

[8] Chang HC, Yeo L, "Electrokinetically Driven Microfluidics and Nanofluidics." Cambridge University Press, 2009

[9] Whitesides, George M., "The origins and future of microfluidics." Insight Overview, Nature Vol 442, 2006

[10] Klarman, Dan, et al. “A Model of Electrowetting, Reversed Electrowetting, and Contact Angle Saturation.” Langmuir, vol. 27, no. 10, 2011, pp. 6031–6041., doi:10.1021/la2004326.

[11] Schertzer, M. J., et al. “An Empirically Validated Analytical Model of Droplet Dynamics in Electrowetting on Dielectric Devices.” Langmuir, vol. 26, no. 24, 2010, pp. 19230–19238., doi:10.1021/la103702t.

[12] Kavousanakis, Michail E., et al. “How to Achieve Reversible Electrowetting on Superhydrophobic Surfaces.” Langmuir, vol. 34, no. 14, 2018, pp. 4173–4179., doi:10.1021/acs.langmuir.7b04371.

[13] Chamakos, Nikolaos T., et al. “Effect of Substrate Topography, Material Wettability and Dielectric Thickness on Reversible Electrowetting.” Colloids and Surfaces A: Physicochemical and Engineering Aspects, vol. 555, 2018, pp. 595–604., doi:10.1016/j.colsurfa.2018.07.043.

[14] Paneru, Mani, et al. “Static and Dynamic Electrowetting of an Ionic Liquid in a Solid/Liquid/Liquid System.” Journal of the American Chemical Society, vol. 132, no. 24, 2010, pp. 8301–8308., doi:10.1021/ja9106397.

[15] Verheijen and Prins, "Reversible Electrowetting and Trapping of Charge: Model and Experiments" Langmuir 15, 6616 (1999).

[16] Peykov, Quinn, and Ralston, "Electrowetting: a model for contact-angle saturation" Colloid Polym. Sci. 278, 789 (2000).

[17] Quinn, Sedev, and Ralston, "Contact Angle Saturation in Electrowetting" J. Phys. Chem. B 109, 6268 (2005).

[18] Vallet, Berge, and Vovelle, "Electrowetting of water and aqueous solutions on poly(ethylene terephthalate) insulating films" Polymer. 37, 2465 (1996).

[19] Jiang, Ma, Hasko, and Nathan, "Influence of polarization on contact angle saturation during electrowetting" Appl. Phys. Lett. 109, 211601 (2016)

[20] J. MacArthur, P. Lozano, et al., "Microfluidic and Extractor Electrode Update in the ion-Electrospray Propulsion System", IEPC-2019-909

[21] Berry, Shaun, and Jakub Kedzierski. “New Methods to Transport Fluids in Micro-Sized Devices.” LINCOLN LABORATORY JOURNAL, vol. 17, no. 2, 2008.

[22] Berthier J (2016). Open microfluidics. Brakke, Kenneth A., Berthier, Erwin. Hoboken, NJ: Wiley. ISBN 9781118720936. OCLC 953661963.

[23] Tao FF, Xiao X, Lei KF, Lee I, "Paper-based cell culture microfluidic system". BioChip Journal. 9 (2): 97–104, 2015

[24] Ballerini DR, Li X, Shen W, "Flow control concepts for thread-based microfluidic devices". Biomicrofluidics. 5 (1): 14105, 2011

[25] Swanson C, Lee S, Aranyosi A, Tien B, Chan C, Wong M, Lowe J, Jain S, Ghaffari R, "Rapid light transmittance measurements in paper-based microfluidic devices". Sensing and Bio-Sensing Research. 5: 55–61, 2015

[26] Yang D, Krasowska M, Priest C, Popescu MN, Ralston J., "Dynamics of Capillary-Driven Flow in Open Microchannels". The Journal of Physical Chemistry C. 115 (38): 18761–18769. Sep. 2011, doi:10.1021/jp2065826. ISSN 1932-7447.

[27] Casavant BP, Berthier E, Theberge AB, Berthier J, Montanez-Sauri SI, Bischel LL, et al. (June 2013). "Suspended microfluidics". Proceedings of the National Academy of Sciences of the United States of America. 110 (25): 10111–6.

[28] Ansari, Mehrad Gholizadeh. “Numerical Modeling of Capillary-Driven Flow in Open Microchannels: an Implication of Optimized Wicking Fabric Design.” SM Thesis, Missouri ST, 2018

[29] Kashaninejad, Navid. “Analytical Modeling of Fluid Flow in Hydrophobic, Rectangular Microchannels with General Navier-Slip Boundary Conditions.” 2019, doi:10.20944/preprints201909.0061.v1.

[30] Baret, Decre, Herminghaus, Seeman, "Transport Dynamics in Open Microfluidic Grooves" Langmuir, 23, 9, 5200–5204, 2007

[31] A. Ashish Saha and S. K. Mitra, “Effect of dynamic contact angle in a volume of fluid (VOF) model for a microfluidic capillary flow,” J. Colloid Interface Sci., vol. 339, no. 2, pp. 461–480, 2009.

[32] Khare, Herminghaus, Baret, Law, Brinkmann, Seeman, "Switching Liquid Morphologies on Linear Grooves" Langmuir, 23, 26, 12997–13006, 2007

[33] Barman, Swain, Law, Seeman, Herminghaus, Khare, "Electrowetting Actuated Microfluidic Transport in Surface Grooves with Triangular Cross Section" Langmuir, 31, 3, 1231–1236, 2015

[34] Jiang, Peng, et al. "Large-Scale Fabrication of Wafer-Size Colloidal Crystals, Macroporous Polymers and Nanocomposites by Spin-Coating." J. AM. CHEM. SOC. 2004, vol. 126, pp. 13778-13786, doi: 10.1021/ja0470923

[35] Jiang, P. et al. "Single-Crystal Colloidal Multilayers of Controlled Thickness." Chem. Mater. 1999, vol. 11, pp. 2132-2140, doi: 10.1021/cm990080

[36] Xing, Hongyu, et al. "Preparation and characterization of UV curable Al2O3 suspensions applying for stereolithography 3D printing ce-

ramic microcomponent." Powder Technology, vol. 338, 2018, pp. 153–161, doi:10.1016/j.powtec.2018.07.023

[37] Middleman, "An introduction to mass and heat transfer: principles of analysis and design." Wiley Online Library, 1997.

[38] E. Delamarche, A. Bernard, H. Schmid, A. Bietsch, B. Michel, H. Biebuyck, "Micro- fluidic networks for chemical patterning of substrate: design and application to bioas- says," JACS 120, 500-508, 1998.

[39] R. Safavieh, D. Juncker, "Autonomous microfluidic capillary system," Anal. Chem. 74, 6139-6144, 2002.

[40] R. Safavieh, A. Tamayol, D. Juncker, "Serpentine and leading-edge capillary pumps for microfluidic capillary systems," Microfluid Nanofluid 18, 357-366, 2015.

[41] Chang Kun Kang, Sang Min Lee, Im Deok Jung, Phill Gu Jung, Sung Jin Hwang and Jong Soo Ko, "The fabrication of patternable silicon nanotips using deep reactive ion etching", Journal of Micromechanics and Microengineering, 27 May 2008

[42] B. E. Deal and A. S. Grove, "General Relationship for the Thermal Oxidation of Silicon", J. Appl. Phys., vol. 36, no. 12, pp. 3770-3778, 1965.

[43] Brancato, L., Keulemans, G., Gijsenbergh, P., Puers, R. "Plasma enhanced hydrophobicity of parylene-C surfaces for a blood contacting pressure sensor". Procedia Eng. 2014, 87, 336–339.

[44] Trantidou T et al. "Oxygen plasma induced hydrophilicity of Parylene-C thin films" Applied Surface Sci. 2012, Vol.261 pgs. 43–51

[45] C. Guerra-Garcia, D. Krejci, P. Lozano, "Spatial uniformity of the current emitted by an array of passively fed electrospray porous emitters", J. Phys. D: Appl. Phys, 49, 2016

[46] Krejci, D., Mier-Hicks, F., Thomas, R., Haag, T., and Lozano, P., “Emission Characteristics of Passively Fed Electrospray Microthrusters with Propellant Reservoirs,” Journal of Spacecraft and Rockets, Vol. 54, No. 2, 2017, pp. 447–458.

[47] B. Koo, C. Kim, "Evaluation of repeated electrowetting on three different fluoropolymer top coatings", Journal of Micromechanics and Microengineering, 23(6), 2013

[48] Victor A. Lifton, Steve Simon, "Robust Si-Based Membranes for Fluid Control in Microbatteries Using Superlyopohobic Nanostructures", Journal of Microelectromechanical Systems, Vol. 20 No. 1, Feb 2011

[49] R. Manivannan, Anil Jumar, Ch. Subrahmanyam, "Aqueous Gelcasting of Fused Silica Using Colloidal Silica Binder", J. American Ceramic Society, 96(8) 2432-2436, 2013

[50] B. Jańczuk, E. Chibowski, W. Wójcik, "The Influence of n-Alcohols on the Wettability of Hydrophobic Solids", Powder Technology 45, 1-6, 1985

[51] c. Chia, J. Martis, "Grayscale LIthography and Resist Reflow for Parylene Patterning", White Paper, 8 June 2018

[52] Larry L. Hench, Jon K. West, "The sol-gel process", Chem. Rev. 1990, 90(1), pp 33-72

[53] Gisele Azimi, Rajeev Dhiman, Hyuk-Min Kwon, Adam T. Paxson, Kripa K. Varanasi, "Hydrophobicity of rare-earth oxide ceramics", Nature Materials, 12, 315-320, Jan. 20 2013

[54] Catherine E. Miller and Paulo C. Lozano, "The Effects of Metastable Solvated Ions on Electrospray Ion Thruster Efficiency", IEPC-2015-179

[55] Hongyu Xing, et al., "Preparation and characterization of UV curable Al2O3 suspensions applying for stereolithography 3D printing ceramic microcomponent", Powder Technology 338 (2018) 153–161

[56] Jan Deckers, et al., "Additive Manufacturing of Ceramics: A Review", 2014

[57] W. Martino, J. Fernandez de la Mora, Y. Yoshida, G. Saito, and J. Wilkes. Surface tension measurements of highly conducting ionic liquids. Green Chem.,8:390–397, 2006.

[58] Lifton, V.A. and Simon, S., Robust Si-based membranes for fluid control in microbatteries using superlyophobic nanostrcutures, Journal of Microelectromechanical Systems, V. 20, N.1, February 2011.

[59] Chevalliot, et al., "Experimental Validation of the Invariance of Electrowetting Contact Angle Saturation", Journal of Adhesion Science and Technology 26 (2012) 1909-19

[60] Leon, Philip J Ponce de, and Luis F Velásquez-García. “IOPscience.” Journal of Physics D: Applied Physics, IOP Publishing, 2016

[61] Berthier, et al., "Open Microfluidic Capillary Systems", Analytical Chemistry 2019 91 (14), 8739-8750

[62] Krupenkin, et al., "Reversible Wetting-Dewetting Transitions on Electrically Tunable Superhydrophobic Nanostructured Surfaces", Langmuir 2007, 23, 9128-9133

[63] Javadi, A., Habibi, M., Taheri, F. et al. "Effect of wetting on capillary pumping in microchannels". Sci Rep 3, 1412 (2013)

[64] Fu, Xiaotong, and Zachary Gagnon. "Contactless microfluidic pumping using microchannel-integrated carbon black composite membranes." Biomicrofluidics vol. 9,5 054122. 20 Oct. 2015

[65] Carrera, et al., "Interfacial Properties, Densities, and Contact Angles of Task Specific IonicLiquids", J. Chem. Eng. Data 2010,55,609–615

[66] Li, et al., "Dynamic Electrowetting and Dewetting of Ionic Liquids at a Hydrophobic Solid-Liquid Interface", Langmuir 2013, 29, 2631-2639

[67] Paneru, et al., "Electrowetting of Ionic Liquids on Teflon AF1600 in Ambient Hexadecane", Journal of Adhesion Science and Technology 26 (2012) 2047-20

[68] Nanayakkara, et al., "A Fundamental Study on Electrowetting by Traditional and Multifunctional Ionic Liquids:Possible Use in Electrowetting on Dielectric-Based Microfluidic Applications", Analytical Chemistry 2008, 80, 7690–7698

[69] Hatipogullari, Metin; Wylock, Christophe; Pradas, Marc; Kalliadasis, Serafim and Colinet, Pierre (2019). Contact angle hysteresis in a microchannel: Statics. Physical Review Fluids, 4(4), article no. 044008.

[70] Moon et al. "Low voltage electrowetting-on-dielectric." Journal of Applied Physics, 92, 7, 4080-4087, 2002

[71] Monnier, Jérôme, et al. “Numerical Modeling of Electrowetting by a Shape Inverse Approach.” SIAM Journal on Applied Mathematics, vol. 69, no. 5, 2009, pp. 1477–1500., doi:10.1137/050624340.

[72] Peykov, V., et al. “Electrowetting: a Model for Contact-Angle Saturation.” Colloid and Polymer Science, vol. 278, no. 8, 2000, pp. 789–793., doi:10.1007/s003960000333.

[73] Zhao, Rui, and Zhong-Cheng Liang. “Mechanism of Contact Angle Saturation and an Energy-Based Model for Electrowetting.” Chinese Physics B, vol. 25, no. 6, 2016, p. 066801., doi:10.1088/1674-1056/25/6/066801.

[74] Kedzierski, et al., "New Generation of Digital Microfluidic Devices", Journal of Microelectromechanical Systems, VOL. 18, NO. 4, AUGUST 2009

[75] Lam T, Devadhasan JP, Howse R, Kim J, "A Chemically Patterned Microfluidic Paper-based Analytical Device (C-µPAD) for Point-of-Care Diagnostics". Scientific Reports. 7 (1): 1188, 2017

[76] Berthier J, Brakke KA, Gosselin D, Navarro F, Belgacem N, Chaussy D., "Spontaneous capillary flow in curved, open microchannels". Microfluidics and

Nanofluidics. 20 (7): 100. Jul. 2016, doi:10.1007/s10404-016-1766-6. ISSN 1613-4982.

[77] Fouillet Y, Achard JL., "Microfluidique discrète et biotechnologie" Jun. 2004. Comptes Rendus Physique. 5 (5): 577–88. Bibcode:2004CRPhy...5..577F. doi:10.1016/j.crhy.2004.04.004.

[78] Lebedev NN, Skal'skaya IP, "Force acting on a conducting sphere in the field of a parallel plate condenser". Soviet Phys. Tech. Phys. 7: 268–270. 1962

[79] Velev OD, Prevo BG, Bhatt KH., "On-chip manipulation of free droplets". Nature. 426 (6966): 515–6. Dec. 2003, Bibcode:2003Natur.426..515V. doi:10.1038/426515a.

[80] Gascoyne PR, Vykoukal JV, Schwartz JA, Anderson TJ, Vykoukal DM, Current KW, McConaghy C, Becker FF, Andrews C (August 2004). "Dielectrophoresis-based programmable fluidic processors". Lab on a Chip. 4 (4): 299–309. doi:10.1039/b404130e.

[81] Kirby, B. J., "Micro and Nanoscale Fluid Mechanics: Transport in Microfluidic Devices." Cambridge University Press. 2010 ISBN 978-0-521-11903-0.

[82] Shi, Z.; et al. (2018). "Dynamic contact angle hysteresis in liquid bridges". Colloids and Surfaces A: Physicochemical and Engineering Aspects. 555: 365–371. arXiv:1712.04703. doi:10.1016/j.colsurfa.2018.07.004.

[83] Bartoli, C., Von Rohden, H., Thompson, S., and Blommers, J., "A Liquid Caesium Field Ion Source for Space Propulsion," Journal of Physics D: Applied Physics, Vol. 17, No. 12, 1984, pp. 2473.

[84] Krejci, D., Hugonnaud, V., Schonherr, T., Little, B., Reissner, A., Seifert, B., Koch, Q., Bosch Borras, E., and Gonzalez del Amo, J., "Full Performance Mapping of the IFM Nano Thruster, Including Direct Thrust Measurements," Journal of Small Satellites, Vol. 8, No. 2, 2019, pp. 881–893.

[85] Lozano, P. and Martinez-Sanchez, M., “Ionic Liquid Ion Sources: Characterization of Externally Wetted Emitters,” Journal of Colloid and Interface Science, Vol. 282, No. 2, 2004, pp. 415–421.

[86] Lozano, P. C., “Energy Properties of an EMI-Im Ionic Liquid Ion Source,” Journal of Physics D: Applied Physics, Vol. 39, No. 1, 2005.

[87] Legge Jr, R. S. and Lozano, P. C., “Electrospray Propulsion Based on Emitters Microfabricated in Porous Metals,” Journal of Propulsion and Power, Vol. 27, No. 2, 2011, pp. 485–495.

[88] Courtney, D. G., Li, H. Q., and Lozano, P., “Emission Measurements from Planar Arrays of Porous Ionic Liquid Ion Sources,” Journal of Physics D: Applied Physics, Vol. 45, No. 48, 2012.

[89] Mier-Hicks, F. and Lozano, P. C., “Electrospray Thrusters as Precise Attitude Control Actuators for Small Satellites,” Journal of Guidance, Control, and Dynamics, Vol. 40, No. 3, 2017, pp. 642–649.

[90] Hirt and Nichols, “Volume of fluid (VOF) method for the dynamics of free boundaries,” Journal of Computational Phys., vol. 39, no. 1, pp. 201–225, 1981.

[91] Brackbill, Kothe, Zemach, “A continuum method for modeling surface tension,” Journal of Computational Phys., vol. 100, no. 2, pp. 335–354, 1992.

[92] Barkhudarov, "Lagrangian VOF advection Method for FLOW-3D", FLOW-3D publication, 2004

[93] Lozano, P.C., Wardle, B.L., Moloney, P. et al. Nanoengineered thrusters for the next giant leap in space exploration. MRS Bulletin 40, 842–849 (2015).